INFORMATION TO USERS

This manuscript has been reproduced from the microfilm master. UMI films the text directly from the original or copy submitted. Thus, some thesis and dissertation copies are in typewriter face, while others may be from any type of computer printer.

The quality of this reproduction is dependent upon the quality of the copy submitted. Broken or indistinct print, colored or poor quality illustrations and photographs, print bleedthrough, substandard margins, and improper alignment can adversely affect reproduction.

In the unlikely event that the author did not send UMI a complete manuscript and there are missing pages, these will be noted. Also, if unauthorized copyright material had to be removed, a note will indicate the deletion.

Oversize materials (e.g., maps, drawings, charts) are reproduced by sectioning the original, beginning at the upper left-hand corner and continuing from left to right in equal sections with small overlaps.

Photographs included in the original manuscript have been reproduced xerographically in this copy. Higher quality 6" x 9" black and white photographic prints are available for any photographs or illustrations appearing in this copy for an additional charge. Contact UMI directly to order.

Bell & Howell Information and Learning
300 North Zeeb Road, Ann Arbor, MI 48106-1346 USA
800-521-0600

Small Angle Scattering Studies of Phospholipids in Excess Water

by

PETER C. MASON

B.Sc., M.Sc.

A Thesis
Submitted to the School of Graduate Studies
in Partial Fulfilment of the Requirements
for the Degree
Doctor of Philosophy

McMaster University
©Copyright by Peter C. Mason, 1998.

Small Angle Scattering Studies of Phospholipids in Excess Water

DOCTOR OF PHILOSOPHY (1998)
(Physics)

McMaster University
Hamilton, Ontario

TITLE: Small Angle Scattering Studies of Phospholipids in Excess Water

AUTHOR: Peter C. Mason

SUPERVISOR: Dr. B. D. Gaulin

NUMBER OF PAGES: xi, 116

Abstract

Model membrane systems composed of homogeneous suspensions of phospholipids in an aqueous environment have been of great interest for their biological relevance and for their intriguing physical properties. When placed in excess water, phospholipids will spontaneously self-assembly into multilamellar vesicles consisting of repeating bilayer-water layer units which are ideally suited for examination via scattering techniques.

Small angle scattering techniques have played an integral role in the study of the morphology and phase behaviour of model membrane systems. This thesis focuses on small angle neutron scattering (SANS) work on two different model membrane systems, dipalmitoylphosphatidylcholine (DPPC) and 1-palmitoyl-2-oleoylphosphatidylethanolomine (POPE). Three main results, which contribute new information or ideas, are presented.

SANS and X-ray diffraction studies of DPPC and DPPC in which the quaternary ammonium hydrogens have been replaced with deuterium (DPPC-d_9) have been performed as a function of temperature in a range from 20 °C to 50 °C . DPPC will display three distinct phases in this range: a low temperature gel ($L_{\beta'}$) phase, an intermediate ripple ($P_{\beta'}$) phase, and a high temperature liquid crystalline (L_α) phase. The $P_{\beta'}$ phase, which spans an eight degree range from 35 °C to 42 °C , is known to exhibit non-equilibrium behaviour. On cooling from the L_α phase, the $P_{\beta'}$ phase formed is metastable but long lived. We present complementary SANS and X-ray diffraction work which shows a complex multipeak pattern for the metastable $P_{\beta'}$ phase. A simple, single wavelength model is proposed that explains our data and also previously published synchrotron X-ray data which was interpreted in terms of a more complex model of competing rippled domains. We also show that the metastability persists into the $L_{\beta'}$ phase.

High resolution SANS work on large unilamellar vesicles (LUVs) of DPPC shows that we are able to extract such parameters as vesicle radius and bilayer thickness from the small angle scattering profile. We present, for the first time, diffraction evidence for the development of a ripple modulation of the bilayer surface in LUVs. Calorimetric work done in conjunction with the SANS offers supporting evidence for this claim.

An examination of the high resolution SANS profiles of multilamellar samples of POPE, DPPC, and DPPC-d_9 is presented which shows that the interfacial properties of model membrane systems can be inferred from scattering techniques. Results show that POPE, which has a relatively small headgroup, displays a smooth water-lipid interface, which can be described using Porod's law of surface scattering, in both its gel and liquid crystalline phases. DPPC and DPPC-d_9, on the other hand, are consistent in showing that the interface between the phosphatidylcholine (PC) headgroups and the water in the $L_{\beta'}$ and $P_{\beta'}$ phases is rough and disordered. On raising the temperature into the L_α phase of DPPC, this interface becomes smooth.

Acknowledgements

I have had the great fortune of working with and sharing my graduate school experience with a great many people who have enriched my life during my Ph.D.

Bruce Gaulin, my embattled supervisor and friend, deservedly tops the list. Perhaps the most definitive thing I can say about Bruce is that I am convinced that there is no other person at McMaster who could have supervised me to completion over these five years. My respect for Bruce and his scientific prowess has always been inversely related to his insight into sports and his organizational skills.

I owe a great deal of gratitude to Richard Epand for his remarkable patience in (repeatedly) explaining simple biochemistry to me, his keen input into this work, his miraculous speed in proof-reading, his companionship on the tennis courts, and his fine example of what a dedicated scientist and person should be.

Mark Lumsden deserves special mention for his daily friendship and assistance.

Thanks go to my companions in the lab for their friendship, patience and input: Marcy Lumsden, Chris Wiebe, Jason Gardner, and Marek Kiela.

Thanks for the support and aid of those people who truly define the face of the department: Wendy Malarek, Jackie Collin, Cheryl Johnston, and Rosemary McNeice.

I would like to specifically thank my friends who organized and/or participated in the many sporting distractions during my time here, particularly Andy Duncan, Frank Hayes, Rob Hughes, and David Jones.

Builders category: Andy Duft, Mary and Ian Lumsden, Karen Cameron, Sarah, Emily, Jessica, Rebecca, and Colin Ellard, Jim and Tatiana Startseva, Merle Robertson, Ian and Brandy Cameron, Dennis Tokaryk, Gypsy and Scratchy Andriani.

Finally, my endless thanks to Anita Andriani Mason for all that has past and all there is to come.

Preface

The bulk of the original work in this thesis is presented in Chapters 3, 4, and 5 which are included as a series of three papers, two of which have been peer-reviewed and accepted for publication in Physical Review E, and one that has been submitted to this same journal and is currently under review. The papers are authored by myself, B.D. Gaulin, R.M. Epand, G.D. Wignall, and J.S. Lin.

The neutron scattering experiments were performed by myself with advice on the spectrometer configuration provided by G.D. Wignall and J.S. Lin. The X-ray experiments were performed by myself under the ever-watchful eye of B.D. Gaulin. The calorimetry experiments were conducted by R.M. Epand who bore my input stoically.

All samples used in these experiments were prepared by myself under the tutelage of R.M Epand and R.F. Epand. I performed all scattering analysis with guidance from B.D. Gaulin. R.F. Epand provided useful advice on the analysis of calorimetric data. I wrote all three manuscripts with proofreading and editing assistance provided by B.D. Gaulin and R.M. Epand.

Note that there are inconsistencies in spelling style between these papers and the rest of the thesis as the American Physical Society does not allow standard Canadian spelling to appear in their journals where it conflicts with the common American form.

Contents

List of Figures

List of Tables

Chapter 1

Introduction

The study of model systems has been a common investigative motif in the pursuit of a more complete scientific understanding of nature. Physics in particular has enjoyed great success in mapping complex problems on to well known, simple, solvable models. In this thesis we present structural studies of model membrane systems which mimic their more complex cousins in nature, biological membranes. A more complete understanding of such systems should help to advance the science of naturally occurring membranes and reveal some of the mechanisms behind membrane modulated biological function.

In addition to their biological relevance, model membrane systems attract the attention of physicists for their remarkable array of properties. Membranes represent quasi two-dimensional systems which exhibit a rich phase behaviour as a function of a variety of extensive parameters. Their material characteristics, including unrivaled flexibility and strength, have made them a popular object of study for materials research scientists. Model membranes are also excellent systems for use in medical and food preservation techniques as they can be introduced without fear of toxicity. For example, using model membranes as vehicle for drug delivery is an idea which is growing in its application.

1.1 Phospholipids

Model membrane systems are composed of mixtures of phospholipid molecules in an aqueous environment. The systems studied in this thesis are homogeneous, consisting of membranes made of a single lipid component. Phospholipids are the most common lipid form in biological membranes. They are characterized by two non-polar acyl chains which are esterified to a glycerol backbone which in turn is esterified to a phosphate to which is bonded an alcohol. A wide range of phospholipids with varying properties can be constructed by substituting different alcohols in the headgroup region or by attaching different acyl chains to the glycerol backbone. The nomenclature for identifying the phospholipids depends both on the type of alcohol attached to the phosphate group, the number of carbons in the acyl chains, and the degree of saturation in the chains. For example, phospholipids with a choline alcohol are generally described as phosphatidylcholines (PCs) while those with an ethanolamine in the headgroup are denoted phosphatidylethanolamines (PEs). Table 1.1 lists some common alcohol headgroups along with their structures, systematic, and generic names. At physiological pH, the phosphate group will carry a full net negative charge, making both PCs and PEs zwitterionic as they carry a net positive charge on their amine groups. Phosphatidylserines and phosphatidylglycerols will carry a net negative charge. The polar nature of the headgroups is responsible for their high degree of solvation in an aqueous solvent.

Table 1.2 lists a number of the possible fatty acids which may appear as acyl chains in phospholipids. A typical chain is between 14 and 20 carbon atoms long and ends with a terminal methyl (CH_3) group. The chains may be saturated, meaning that there are no carbon double bonds, or unsaturated, implying the presence of at least one carbon-carbon double bond. Palmitic acid, for example, is sixteen carbons long with no double bonds and is denoted 16:0 using a classification system where the first

Alcohol	**Structure**	**Systematic Name**	**Generic Name**
Glycerol	$HO\text{-}CH_2\text{-}\underset{\displaystyle OH}{\underset{\vert}{CH}}\text{-}CH_2\text{-}OH$	1,2-Diacyl-*sn*- glycero-3-phospho-1-*sn*- glycerol	Phosphatidylglycerol
Choline	$\overset{+}{HO\text{-}CH_2\text{-}CH_2\text{-}N(CH_3)_3}$	1,2-Diacyl-*sn*- glycero-3-phosphocholine	Phosphatidylcholine
Serine	$\overset{+}{HO\text{-}CH_2\text{-}\underset{\displaystyle COO^-}{\underset{\vert}{CH}}\text{-}NH_3}$	1,2-Diacyl-*sn* -glycero-3-phosphoserine	Phosphatidylserine
Ethanolamine	$\overset{+}{HO\text{-}CH_2\text{-}CH_2\text{-}NH_3}$	1,2-Diacyl-*sn*-glycero-3-phosphoethanolamine	Phosphatidylethanolamine

Table 1.1: Some common alcohols found in phospholipids along with both the systematic and generic names that correspond to the respective headgroup (from Cevc & Marsh (1987))

Symbol	Common Name	Structure
14:0	Myristic	$CH_3(CH_2)_{12}COOH$
16:0	Palmitic	$CH_3(CH_2)_{14}COOH$
18:0	Stearic	$CH_3(CH_2)_{16}COOH$
16:1, Δ_9	Palmitoleic	$CH_3(CH_2)_5CH{=}CH(CH_2)_7COOH$
18:1, Δ_9	Oleic	$CH_3(CH_2)_7CH{=}CH(CH_2)_7COOH$
18:2, $\Delta_{2,9}$	Linoleic	$CH_3(CH_2)_4CH{=}CHCH_2CH{=}CH(CH_2)_7COOH$
20:0	Arachidic	$CH_3(CH_2)_{18}COOH$

Table 1.2: Common fatty acid chains which occur in phospholipids (from Harrison & Lunt (1975))

number reflects the number of carbons in the chain, and the second number counts the number of double bonds. Consequently, the 18 carbon long oleic acid with its single double bond between carbons 9 and 10 and is denoted 18:1, Δ_9, where the Δ_9 indicates the position of the double bond. An unsaturated chain has fewer conformational degrees of freedom than a saturated chain, a difference which will affect the bilayer properties. Regardless of saturation level, most acyl chains are insoluble in water. The insolubility of the oily acyl chains is a result of the *hydrophobic effect* which is driven by entropic effects arising from the connected hydrogen bonding structure of water (Tanford 1980). In order to maintain their strong hydrogen bonded network, water molecules sacrifice conformational entropy and form an ordered framework encapsulating the hydrophobic chain.

1.1.1 Bilayers and Self-Assembly

The amphipathic nature of phospholipids leads to rather remarkable properties when they are introduced to water or some other polar solvent. In order to expose the hydrophilic headgroup regions to the solvent while simultaneously shielding the hydrophobic acyl chains, the phospholipids will, in most cases, spontaneously arrange themselves into a bilayer construct. These bilayers will close in on themselves to form

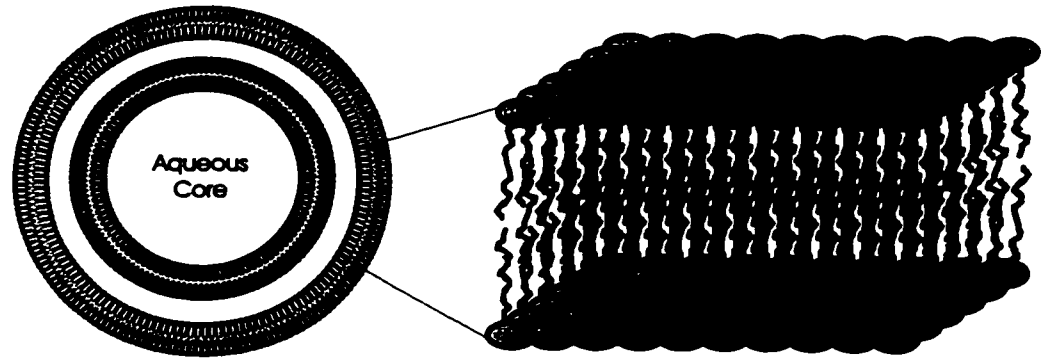

Figure 1.1: A multilamellar vesicle composed of two concentric bilayers.

bilayer vesicles, completely sequestering the acyl chains from the aqueous environment. Unless special steps are taken, the vesicles will not be composed of a single lipid bilayer, but anywhere from 10-50 concentric bilayers with a layer of water separating neighouring bilayers (Yeagle 1987). Figure 1.1 shows a multilamellar vesicle with two concentric bilayers along with a magnification of the bilayer structure.

The interplay of forces in determining the properties of MLVs is quite complex. Van der Waals forces and conformational entropic effects dominate the interchain interactions. For interlamellar interactions, it is commonly stated that attractive van der Waals forces between the bilayers are countered by repulsive steric and undulation forces. However the steric forces can be further dissected into a subset of forces of varying strengths and ranges which depend on headgroup size, intrinsic membrane curvature, and interbilayer separation to name a few. An excellent review is given by Israelachvili & Wennerström (1992).

Bilayers in Scattering Experiments

Multilamellar vesicles (MLVs) are ideally suited to scattering experiments as the bilayer-water layer building blocks form a repeating structural unit in the MLV construct. Multilamellar vesicles in solution are analogous to powder samples for

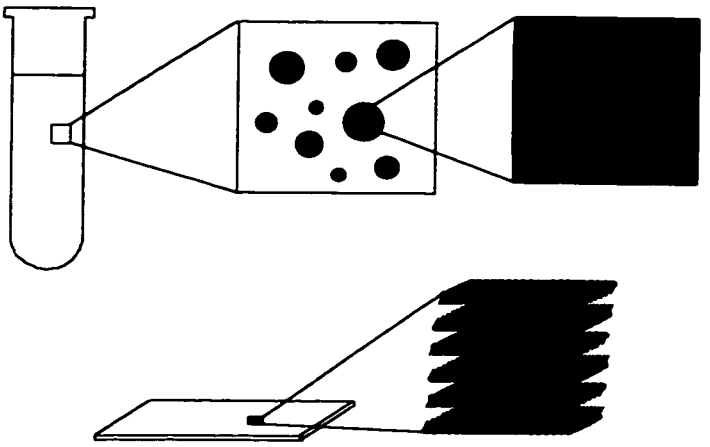

Figure 1.2: Two different bilayer sample preparations used in scattering experiments. The top picture shows multilamellar vesicles in an aqueous buffer while the bottom shows aligned stacks of bilayer on a substrate (from Lumsden (1998)).

typical crystallographic studies. An advantage of using MLVs is that all scattering geometries are seen simultaneously in a diffraction experiment. This is also a disadvantage in that it can be difficult to distinguish between in-plane and out-of-plane spatial correlations. Aligned samples on a substrate can be used in many cases to clarify exactly which reflections are being observed. Figure 1.2 shows an artists rendition of the two different sample preparations.

A problem with aligned samples, which may soon be remedied (Katsaras 1997, Lumsden 1998), is that they have heretofore relied on exposure to a 100% relative humidity environment, instead of direct contact with water, to achieve full hydration. The difference in sample environment leads to inadequate water uptake in aligned samples. Experiments have shown that some properties of aligned samples are systematically altered compared to the more biologically relevant MLVs. In particular, the formation of the ripple phase of DPPC, discussed in section 1.2.2 and in more detail in chapter 3, appears to be inhibited in aligned samples.

Real biological membranes are, of course, not multilamellar in nature. As cellular membranes consist of a single bilayer vesicle, there is considerable interest in extracting as much information as possible about model membrane systems consisting of a single, vesicular bilayer. Unilammellar vesicles can be made from a variety of techniques but the most practical and reproducible method is by extruding MLVs through an appropriately sized filter (Hope, Bally, Webb & Cullis 1985). Large unilamellar vesicles (LUVs) produced in this manner are useful for studying vesicular systems without having to consider bilayer-bilayer interactions. An examination of such a system is presented in chapter 4.

1.1.2 DPPC and POPE

This thesis presents work on two specific phospholipids in excess water, DPPC and POPE. Using the systematic nomenclature, the names are written as 1,2-dipalmitoyl-*sn*-glycero-3-phosphocholine (DPPC) and 1-palmitoyl-2-oleoyl-*sn*-glycero-3-phosphoethanolamine (POPE). The rational behind these epithets is demonstrated in Fig. 1.3 which shows the chemical structures of DPPC and POPE. DPPC consists of two palmitic acid chains which are esterified to carbons 1 and 2 of the glycerol. A choline headgroup is attached through a phosphate group to the 3^{rd} carbon of the glycerol. POPE has a palmitic acid esterified to carbon 1, oleic acid esterified to carbon 2, and an ethanolamine alcohol attached through the phosphate group to carbon 3 of the glycerol.

Both DPPC and POPE are naturally occurring lipids in biological systems. POPE is typical of the type of PE found in biological membranes while DPPC makes up approximately 80% of mammalian lung surfactant. Referring again to Fig. 1.3, we see that the two phospholipids share common features but have some important differences. The headgroups are very similar in nature with the only difference being

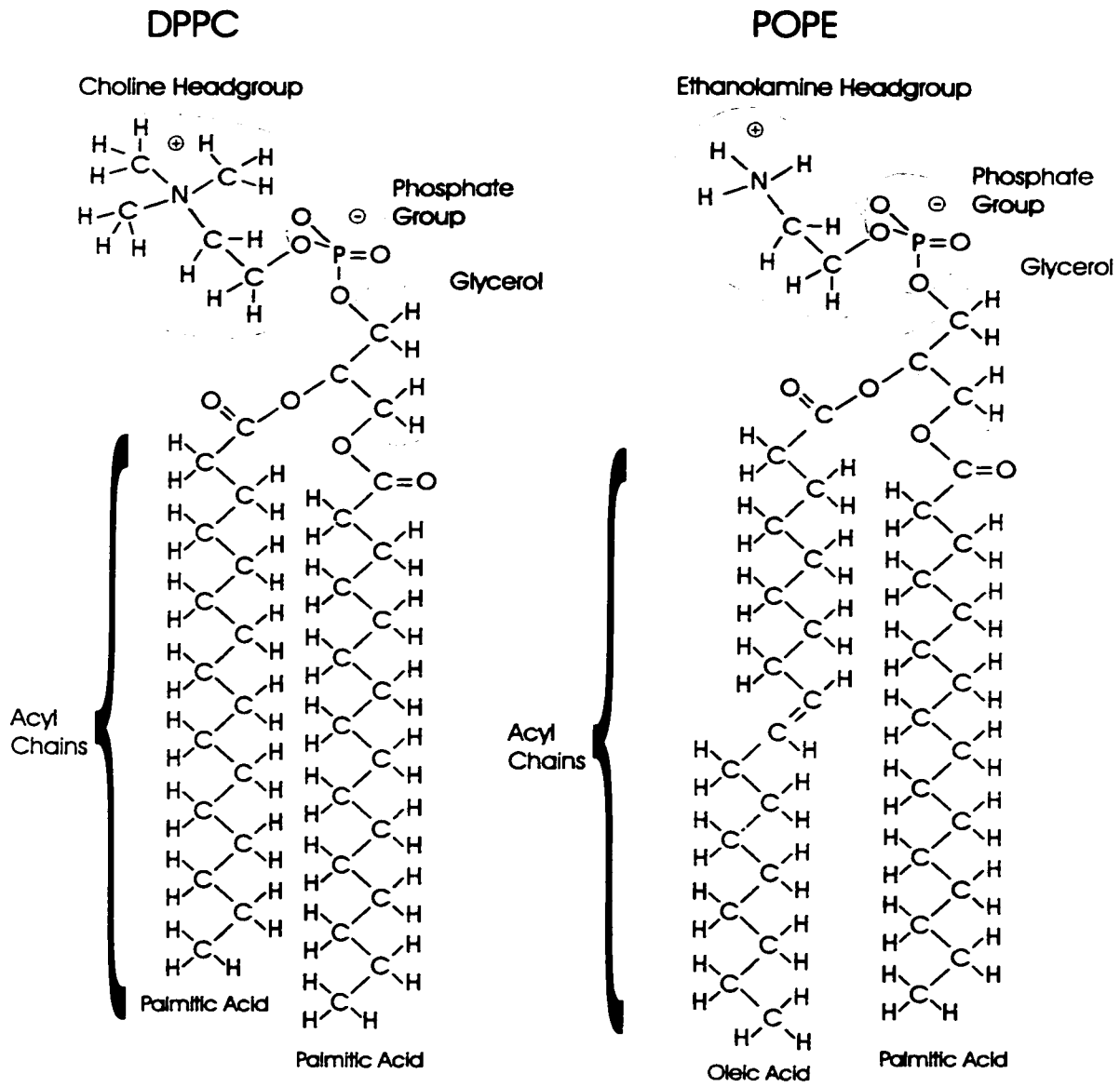

Figure 1.3: The chemical structures of DPPC on the left and POPE on the right.

that the quaternary methyl groups of the choline headgroup are replaced with hydrogens in the ethanolamine headgroups giving the phosphatidylethanolamines a much smaller headgroup than the phosphatidylcholines. Both headgroups are electrically neutral but zwitterionic with the approximate location of the charges indicated in the figure. The other difference of note is the substitution of oleic acid in POPE for palmitic acid of DPPC on the second carbon of the glycerol backbone. The presence of the cis double bond between carbons 9 and 10 inhibits the conformational freedom of the acyl chain as it precludes the trans-gauche isomerizations that are characteristic of the carbon-carbon single bonds. In addition the cis double bond serves to separate the acyl chains which affects the phase behaviour of the membrane as discussed in section 1.2.

The larger headgroup of DPPC inhibits its ability to pack within the plane of the bilayer. Evidence for this is seen in the characteristics of the acyl chain conformations in the gel phases to be discussed in sections 1.2.1 and 1.2.2. Crystals of DPPC compensate for the headgroup size by inducing neighbouring rows of DPPC molecules to be displaced from one another in the direction of the bilayer normal (Cevc & Marsh 1987). Such displacements may serve to roughen the interface between the headgroups and the solvent as evidenced by the work presented in chapter 5. In contrast, the relatively small PE headgroup in POPE is able to recede into the plane of the bilayer without distorting the acyl chain packing. The interfacial consequences of this will be discussed in chapter 5.

1.2 Lipid Polymorphism

Lipid samples in an aqueous environment are polymorphic in nature. Structural changes can be seen as a function of a variety conditions such as pH, ionic

strength, lipid concentration, pressure, and temperature. The studies presented in this thesis are all performed in excess water conditions with all other environmental factors held constant except for temperature. Even with these severe limitations in parameter variability, the phospholipids studied exhibit a wide range of structures. Hydrated multilamellar vesicles undergo a series of phase transitions as a function of temperature, typically in the sequence of subgel $L_{c'}$, gel $L_{\beta'}$, ripple $P_{\beta'}$, and liquid crystalline L_{α} phases. DPPC displays this type of phase behaviour while POPE is missing the $L_{c'}$ and $P_{\beta'}$ phases, replaces the $L_{\beta'}$ phase with a L_{β}, and forms an inverted hexagonal H_{II} at high temperatures. Under certain conditions, other lipid systems form a bicontinuous cubic Q phase. Both the H_{II} and Q phases are non-lamellar phases and are not studied in this work, but it is interesting to note that such phases have been the focus of a great deal of attention for their possible role in biological function (Epand 1996). The H_{II} phase in particular seems to hold clues to mechanisms leading to membrane fusion.

The phase behaviour of phospholipid systems involves a complex interplay among a number of factors. While a complete understanding of phospholipid polymorphism requires a microscopic description of various interactions, a qualitative understanding of the bulk properties can, in many cases, be understood by reducing the problem to consider only simplified geometric arguments. For example, Israelachvili, Marčelja & Horn (1980) consider the self-organization of lipids in water and present ideas which allow a rough understanding of the role of headgroup size and chain length in the formation of either lamellar or hexagonal phases in lipids. They assume an interfacial free energy per molecule given by

$$G = \gamma a + \frac{C}{a} \tag{1.1}$$

where γ is the interfacial hydrophobic energy per unit area, a is the area per molecule, and C is a constant representing the repulsion of adjacent lipids. Minimizing the free

energy with respect to the interfacial area yields an equilibrium value $a_0 = (\frac{C}{\gamma})^{\frac{1}{2}}$. Assume that the volume, V, occupied by a lipid molecule does not change much with the motional behaviour of the acyl chains at any given temperature. Now if a lamellar structure is formed, the phospholipid will occupy a cylindrical volume, V_c, which is defined from the product of the preferred area, a_0 and the length of the acyl chains, l_c, which we call the critical length. If

$$\frac{V}{V_c} = \frac{V}{a_0 l_c} \sim 1 \tag{1.2}$$

then the planar bilayer structure is stable. If the ratio given in Eq. 1.2 grows, i.e. if

$$\frac{V}{a_0 l_c} > 1 \tag{1.3}$$

this is an indication that the bilayer structure is not stable and a larger area for the acyl chains is favoured. This implies that the hexagonal H_{II} phase would be formed. Comparing DPPC and POPE, the larger headgroup of PC implies a larger value for a_0, while the chain length l_c is approximately equivalent for both. Consequently the ratio in Eq. 1.2 will be larger for POPE implying that formation of the H_{II} phase will be more favourable in POPE than in DPPC. This is indeed the case as the hexagonal phase will form in POPE but is not seen for DPPC in excess water conditions. Further, it can be deduced that the H_{II} phase will be a high temperature phase for POPE with l_c being reduced by the motional disorder at temperatures in the fluid phase. This is also reflected in the phase behaviour of POPE which forms the H_{II} phase at temperatures beyond the L_α phase.

For the lipids DPPC and POPE in excess water in the temperature regime spanned by the experiments in this thesis, only the gel ($L_{\beta'}$ or L_β), ripple, and liquid crystalline phases will occur. We will henceforth restrict our discussion of the structure to these phases. Figure 1.4 shows a schematic of the $L_{\beta'}$, $P_{\beta'}$, and L_α phases of DPPC. We discuss the structural properties of these phases below.

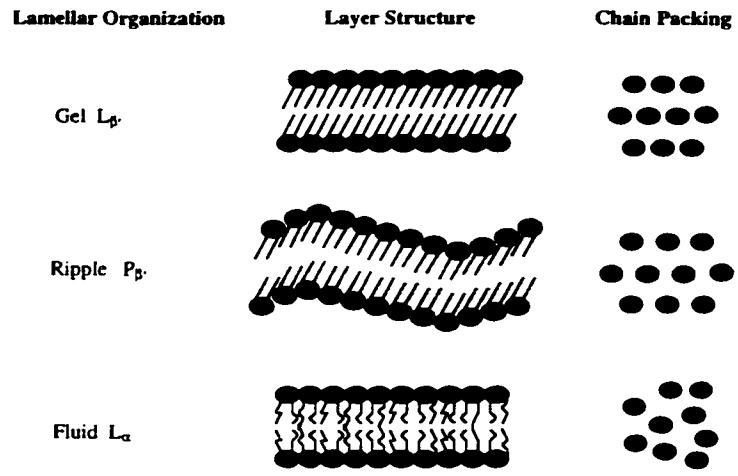

Figure 1.4: Cartoon of the bilayer structure and corresponding acyl chain packing lattice of DPPC in three phases (from Lumsden (1998)).

1.2.1 Gel Phase

The gel phase for DPPC is expressed at temperatures between 18 °C and 33 °C. It is characterized by an all-trans conformation of the acyl chains which pack on a distorted hexagonal lattice. The distortion is a result of competition between the headgroup steric repulsion, which favours a large interlipid distance, and the acyl chain van der Waals attraction which favour a hexagonal close packing arrangement. To find a balance between these competing factors while forming a lamellar arrangement, the chains develop a tilt with respect to the bilayer normal (Tardieu, Luzzati & Reman 1973). Figure 1.4 shows this tilt along with the chain packing lattice. X-ray diffraction studies (Mitsui 1978, Franks & Lieb 1981) show a sharp peak corresponding to an interchain separation of 4.2 Å. Despite the "frozen" nature of the chains in the gel phase, the acyl chains are have some rotational freedom about the molecular long axis (see Fig. 1.3) (Cameron & Mantsch 1982, Trahms, Klabe & Boroske 1983).

This degree of freedom is eliminated in the subgel (L_c) phase.

The gel phase for POPE occurs for temperatures below 23 °C . It is essentially the same as the DPPC gel phase except that the smaller PE headgroup allows the acyl chains to pack without the development of a tilt angle (Suwalsky & Tapia 1981). This distinction is denoted by dropping the prime in the phase label, meaning that the POPE gel phase is denoted the L_β phase. Of course the lack of trans-gauche isomerization in the L_β phase of POPE does not eliminate the cis double bond on the oleic acid acyl chain.

1.2.2 Ripple Phase

The ripple $P_{\beta'}$ phase of DPPC, first discovered by Tardieu et al. (1973), is the least understood of the DPPC mesophases. Many attempts have been made to develop a theoretical description of the mechanisms behind the formation of this phase but none have yet proved fully satisfactory. Nevertheless, there are a number of pieces to the puzzle that are known.

The ripple phase, in terms of symmetry, is a gel phase much like the $L_{\beta'}$ phase. Its defining characteristic is the development of a long wavelength periodic modulation of the bilayer surface. To within experimental error, the bilayer enthalpy and entropy of the $L_{\beta'} \rightarrow P_{\beta'}$ transition (known as the pretransition) is independent of chain length, suggesting that the driving mechanisms behind the transition are related to changes in the headgroup and interfacial regions (Cevc & Marsh 1987). This is supported by X-ray diffraction work which suggests that, apart from a relaxation of the lattice distortion, the acyl chains remain packed on an hexagonal lattice as in the $L_{\beta'}$ phase. Figure 1.4 demonstrates these points more clearly. It is believed that the mismatch between the occupied areas of the headgroup and the acyl chains play a key role in the formation of the ripple phase (Hatta, Kato & Takahashi 1993)

The formation of the ripple phase is accompanied by a transverse shift of the bilayer lipid molecules (Pearson & Pascher 1979) , which allows the headgroups to occupy a larger volume, and a change in the chain tilt angle to approximately 30°. Nuclear magnetic resonance (NMR) experiments have shown that the headgroup has a great deal more rotational freedom about the P-O bond in the $P_{\beta'}$ phase (Shepherd & Büldt 1978, Shepherd & Büldt 1979).

Many ideas have been proposed to help explain the ripple phase. Detailed treatment of near-neighbour interactions (Pearce & Scott 1982), spontaneous curvature effects (Doniach 1979), strain relaxations (Larsson 1977), domain fluidization (Falkovitz, Seul, Frisch & McConnell 1982) models have all proved inadequate in predicting $P_{\beta'}$ features. Some models have invoked bilayer-bilayer coupling in MLVs as a possible mechanism (Cevc, Zeks & Podgornik 1981), but evidence for rippling in unilamellar vesicles presented in chapter 4 seems to discount this idea.

The solution to the ripple phase problem may depend on the achievement of a more complete experimental picture of this phase. Experiments have suggested that a wide range of ripple wavelengths are obtainable depending on such parameters as lipid type (Wack & Webb 1989), lipid asymmetry (Czajkowsky, Huang & Shao 1995), hydration level (Wack & Webb 1989), solvent composition (Mou, Yang & Shao 1994), and sample history (Yao, Matuoka, Tenchov & Hatta 1991). Regarding this last point, a proposed new model of ripple phase metastability will be given in chapter 3.

1.2.3 Liquid Crystalline Phase

The liquid crystalline L_α phase is considered to be the biologically relevant phase for phospholipid systems as membrane systems at physiological temperatures are found to be in this phase. In the L_α phase the acyl chains are free to undergo trans-gauche isomerizations which results in an increase in the separation distance

between headgroups and a thinning of the the bilayer. The orientational order of the chains remains intact but the periodicity is lost as the lipids are free to migrate throughout the plane of the bilayer. This is evidenced by the disappearance of the sharp 4.2 Å $L_{\beta'}$ peak in the x-ray spectrum which is replaced by a diffuse band of scattering, characteristic of a liquid system, in the range 4.5 Å to 4.7 Å. Again, Fig. 1.4 shows a depiction of this phase. The biological significance of the L_α phase was placed on a strong foundation with the advent of the *fluid mosaic model* (Singer & Nicolson 1972) which proffers three main points: 1. Membrane proteins are free to diffuse in the two-dimensional plane of the membrane. 2. The lipid bilayer serves a dual role as a permeability barrier and as a solvent for the integral membrane proteins. 3. Lipid molecules are able to move laterally in the plane of the bilayer and to "flip-flop" across the bilayer mid-line.

The transitions $P_{\beta'} \rightarrow L_\alpha$ in DPPC and $L_\beta \rightarrow L_\alpha$ in POPE are referred to as the main transition. This transition occurs at $T_m = 42$ °C in DPPC and $T_m = 23$ °C in POPE. The difference in T_m for the two lipids reflects the importance of interchain interactions in driving the transition. The main transition is often referred to as a chain-melting transition and is well characterized both experimentally and theoretically. NMR studies (Gamble & Schimmel 1978, Grünewald, Frisch & Holzwarth 1981) of the main transition have shown that fluid domains nucleate about acyl chains that "melt", creating density fluctuations within the bilayer. These domains grow to encompass the entire bilayer leading to more rapid rotations of the headgroup (Shepherd & Büldt 1978). The increased headgroup separation exposes more of the headgroup to the aqueous environment allowing water molecules to reach polar residues such as the carbonyl oxygens of the chains (Casal & Mantsch 1984) and increasing the hydration of the lipid.

The significance of the acyl chains in the main transition is easily seen in

practice. Experiments have shown that T_m is strongly correlated to the length and saturation level of the chains with relatively weak dependence on the headgroup and interfacial regions (Cevc & Marsh 1987). The value of T_m monotonically increases with chain length as longer chains have stronger van der Waals interactions which inhibit the chain-melting transition. The 37 °C difference in the main transition temperatures of POPE and DPPE (T_m=60 °C), lipids with similar chain lengths and identical headgroups, is due almost entirely to the presence of the cis double bond of the oleic acid acyl chain in POPE. The "kink" in the chain introduced by this bond inhibits acyl chain close packing in POPE thereby reducing the interchain binding energy and depressing the absolute value of T_m.

The theory of the main transition is well-developed. An excellent review is given by Nagle (1980) who has been one of the pioneers of a statistical mechanical description of this transition. Recent experimental (Zhang, Tristram-Nagle, Headrick, Suter & Nagle 1995, Lemmich, Mortensen, Ipsen, Honger, Bauer & Mouritsen 1996) and theoretical work (Nagle, Petrache, Gouliaev, Tristram-Nagle, Liu, Suter & Gawrisch 1998) on the L_α phase as it approaches T_m showing the development of critical behaviour, characteristic of systems approaching the critical point of a second order phase transition, despite the fact that the transition is clearly first order. For this reason, the main transition is often called a pseudo-first order transition (Mouritsen 1991). Such studies have advanced the understanding of the L_α phase and the main transition, but a full explanation of the bilayer behaviour has yet to be achieved.

Chapter 2

Scattering

Neutron and X-ray small angle scattering are among the principle techniques for the microscopic characterization of biological materials. Compared to interatomic length scales which are commonly of interest in condensed matter physics, the length scales for biological systems are large. Small angle neutron scattering, which is typically concerned with the measurement of structures from about 10 Å up to 1000 Å, is an ideal probe with which to examine the model membrane systems described in this thesis as they fall well within this range.

2.1 Basic Ideas

In diffraction, an incident beam of radiation scatters off the sample and, in doing so, probes the scattering object with a sinusoidal signal (Windsor 1988). This is illustrated in Fig. 2.1 in which an incident beam of wavelength λ_0 strikes a sample at an angle θ to the sample normal. The diffracted beam scatters at the same angle θ. The intersection of the incident and scattered beams defines a probe wavelength λ_Q which depends on both the wavelength of the incident radiation and the scattering angle, 2θ. This dependence is illustrated in Fig. 2.2 which shows how interference of

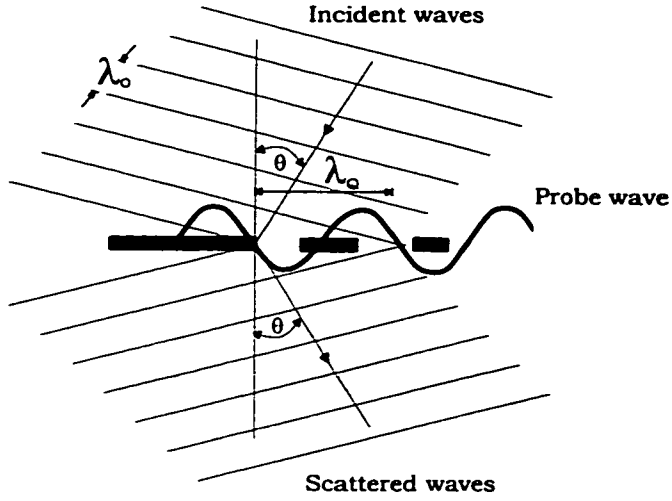

Figure 2.1: Diffraction of incident waves from a scattering object. The intersection of the incident and scattered waves define a probe signal which scans the sample.

incident and scattered waves forms a sinusoidal probe wave along the horizontal of the page for three different scenarios. In (a) the incident radiation has wavelength λ_0 and half scattering angle θ. Panel (b) shows how the probe wavelength increases when the wavelength of the incident radiation is doubled, while panel (c) illustrates the inverse relationship between the scattering angle and the probe wavelength.

Figure 2.2 shows explicitly why small angle scattering is used to study large scale structures. This reciprocal relationship can be seen more clearly by writing the probe wave in terms of a *scattering vector*, **Q**. It is straightforward to show that the distance between intersection points in Fig. 2.2, and therefore λ_Q, is given by $\lambda_Q = \frac{1}{2}\lambda_0 \; sin \; \theta$. The magnitude of the scattering vector is then simply

$$Q = \frac{2\pi}{\lambda_Q} = \frac{4\pi}{\lambda_0} \; sin \; \theta. \tag{2.1}$$

The scattering is greatly enhanced if there is some periodicity, d, to the sample such that $d = \lambda_Q$ in which case we can rewrite Eq. 2.1 as

$$\lambda_0 = 2d \; sin \; \theta \tag{2.2}$$

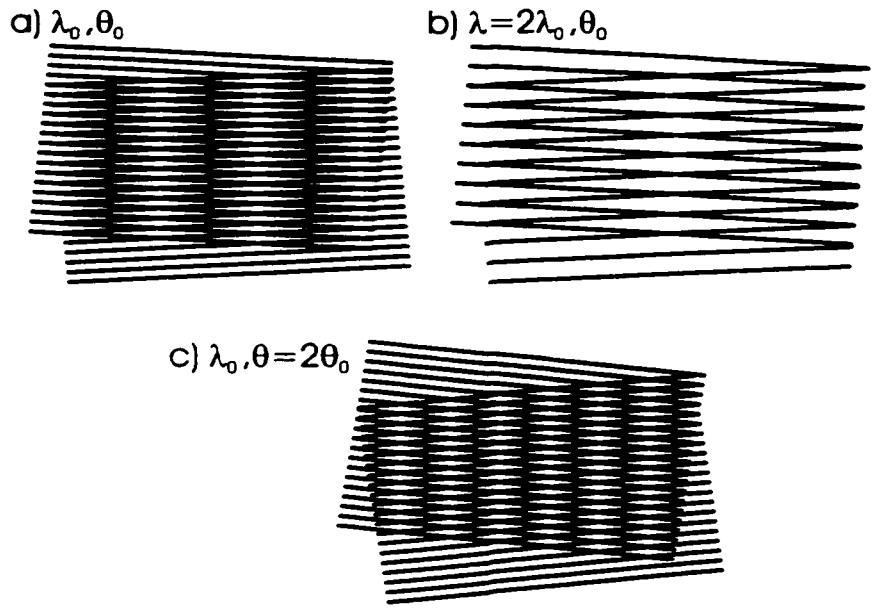

Figure 2.2: Illustration of the interference of incident and scattered waves. The probe wavelength in (a) is doubled in (b) when the wavelength of the radiation is doubled, and halved in (c) where the scattering angle is doubled.

which is the well known Bragg law of diffraction. The more general diffraction pattern from non-periodic microstructure can be thought of as a superposition of the reflections of all possible periodicities with relative intensities that depend on the amount of each present in the scattering sample (Windsor 1988).

2.2 Neutron Scattering

The technique of neutron scattering is ubiquitous in the study of condensed matter systems. Recognition of the contribution of this method came in 1994 with the awarding of the Nobel Prize in Physics to Bertram Brockhouse and Clifford Schull for their pioneering work in the development of the field. A fortuitous combination of properties have contributed to the success of the neutron as a probe. The wavelength of thermal neutrons is on the order of atomic separations, the energy is in the range

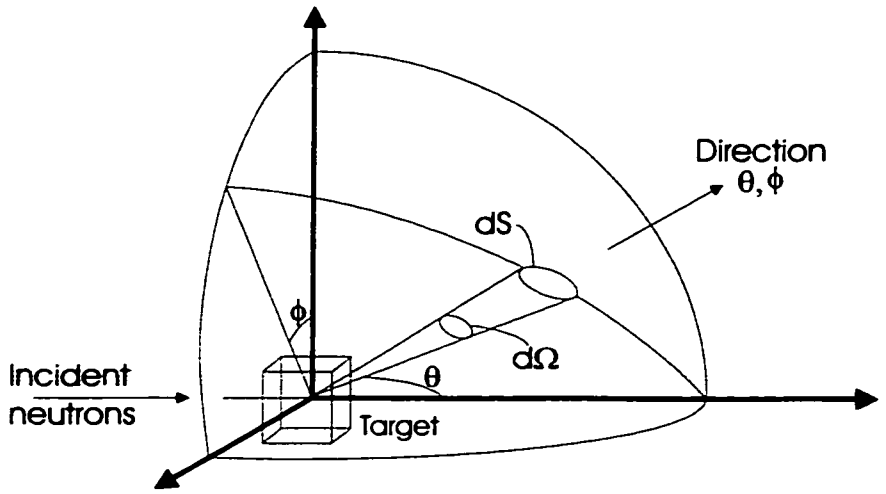

Figure 2.3: Geometry for a scattering experiment.

of many common crystal excitations, the penetration depth allows neutrons to probe bulk properties, and the inherent spin makes it sensitive to magnetic structure as well.

2.2.1 Scattering Cross Section

Most descriptions of neutron scattering are constructed around the idea of the scattering cross section (Squires 1978). Figure 2.3 shows the geometry of a typical experiment with a beam of monochromatic neutrons of energy E incident on a target sample which defines the scattering origin. Imagine there is a detector of area dS in the direction given by θ and ϕ which can measure the scattered neutrons as a function of their energy, E'. If the distance to the detector is large compared to the its dimensions then the solid angle dΩ subtended by the detector will be well defined. The number of neutrons detected per second divided by the incident flux, Φ, then defines the *partial differential cross-section*:

$$\frac{d^2\sigma}{d\Omega dE'} = \frac{\textit{neutrons/sec into } d\Omega \textit{ with energy between } E' \textit{ and } E'+dE'}{\Phi\ d\Omega\ dE'} \tag{2.3}$$

where the measurement of the energy, E', is assumed to measure neutrons with energy in the range E' to $E' + dE'$. In a SANS experiment we do not analyze the energy of the scattered neutrons, which is equivalent to integrating over dE', so it is the *differential cross-section* that is measured:

$$\frac{d\sigma}{d\Omega} = \frac{neutrons/sec\ scattered\ into\ d\Omega}{\Phi\ d\Omega} \tag{2.4}$$

The differential cross section is proportional to the normalized intensity, $I(Q)$, which will be used in further derivations.

If it were possible to measure the scattering in all directions by integrating over $d\Omega$, the result would be the *total scattering cross-section* defined by the equation

$$\sigma_{tot} = \frac{neutrons/sec\ scattered\ in\ all\ directions\ with\ all\ energies}{\Phi} \tag{2.5}$$

Since the flux,Φ, is measured in neutrons per unit area per second, the cross section, σ, will be in units of area as desired.

2.2.2 Scattering From a Single Atom

For non-magnetic systems, neutron scattering will be due to the strong nuclear force acting between the nucleus and the incident neutrons. The range of this force is on the order of 10^{-15} m which is about five orders of magnitude smaller than the wavelength of the neutrons in typical scattering experiments. As a result, the neutron will not be able to resolve any internal structure of the nucleus and the scattering will be isotropic. Imagine a beam of neutrons of velocity v incident on a single, fixed atom. The wavefunction of the incident neutrons can be written as a plane wave:

$$\psi_0 = e^{ikz} \tag{2.6}$$

and the scattered wavefunction, at a point **r** from the origin as

$$\psi_{sc} = -\frac{b}{r}e^{ikr} \tag{2.7}$$

where we have introduced the quantity b, the *scattering length*, of the atom. The minus sign in Eq. 2.7 is arbitrary and implies a value of b greater than zero for a repulsive potential (Squires 1978).

Using Eqs. 2.6 and 2.7 and assuming that the velocity of the neutrons before and after the scattering event is v, we can calculate the differential cross section. $\frac{d\sigma}{d\Omega}$ for elastic scattering. Referring to Fig. 2.3, the number of neutrons passing through an area dS per second will be

$$v\ dS|\psi_{sc}|^2 = v\ dS\frac{b^2}{r^2} = vb^2 d\Omega \tag{2.8}$$

and the flux of incident neutrons is simply

$$\Phi = v|\psi_0|^2 = v \tag{2.9}$$

so from the definition of the differential cross-section (Eq. 2.4) we have

$$\frac{d\sigma}{d\Omega} = \frac{vb^2 d\Omega}{\Phi d\Omega} = b^2 \tag{2.10}$$

and the total cross-section is derived from integrating over all solid angles:

$$\sigma_{tot} = 4\pi b^2 \tag{2.11}$$

From Eq. 2.11 we see that the relationship between the scattering cross-section, σ, and the scattering length, b, is dimensionally intuitive. The scattering length can, in some cases, be a complex number that varies strongly with the neutron incident energy. In such cases the imaginary part of b is associated with absorption which will occur for nuclei which have a resonant compound nucleus within an energy ΔE of the order of the incident neutron energy. The number of nuclei for which this

occurs is quite limited and none are naturally occurring in the samples studied in this thesis, so henceforth we shall assume that b is strictly a real quantity.

The value of the scattering length depends not only on the type of nucleus, but also on its spin state. A detailed discussion of this is given in Squires (1978) and will not be presented here. If the value of b varies in a system of a single element due to the presence of isotopes and/or varying nuclear spin states and the value b_i occurs with relative frequency f_i, we can define an average value for b and b^2 as follows:

$$\bar{b} = \sum_i f_i b_i, \qquad \overline{b^2} = \sum_i f_i b_i^2 \tag{2.12}$$

The result is that the scattering cross section can broken into two terms, a coherent part and an incoherent part

$$\sigma_{tot} = \sigma_{coh} + \sigma_{inc} \tag{2.13}$$

where

$$\sigma_{coh} = 4\pi\bar{b}^2, \qquad \sigma_{inc} = 4\pi(\overline{b^2} - \bar{b}^2) \tag{2.14}$$

Only the coherent part of the scattering cross-section contributes to the diffraction pattern of a system, while the incoherent part contributes a Q-independent background to the scattering. In the following section on neutron diffraction, only the coherent contribution to the scattering will be considered.

Table 2.1 shows the scattering length, coherent, and incoherent scattering cross-sections for a number of common elements. Values for b vary essentially at random throughout the periodic table but the magnitude is limited in range. For biological systems, the most important entries in Table 2.1 are the first two which compare the cross-sections of hydrogen and deuterium. The scattering lengths differ in sign and magnitude, with the deuterium coherent cross-section being enhanced by more than a factor of three. The biggest difference, however, is the huge incoherent

Table 2.1: Scattering lengths and cross sections of some common elements

Element	$\bar{b}$ $(10^{-12}cm)$	σ_{coh} (barns)	σ_{inc} (barns)
Hydrogen	-0.3742	1.760	79.90
Deuterium	0.6674	5.597	2.04
Carbon	0.6648	5.554	0.001
Nitrogen	0.936	11.0	0.49
Oxygen	0.5805	4.23	0.0009
Sodium	0.363	1.66	1.62
Magnesium	0.5375	3.631	0.077
Phosphorus	0.513	3.31	0.006
Sulphur	0.2847	1.019	0.007
Chlorine	0.9579	11.53	5.2
Calcium	0.490	3.02	0.03

cross-section of hydrogen, nearly forty times greater than that of deuterium. These differences have played a key role in the study of biological (and polymer) samples for two reasons. Firstly, the coherent scattering length density of the solvent can be varied continuously by simply altering the ratio of D_2O to H_2O. Secondly, it is possible to selectively deuterate particular functional groups in a molecule. These methods can be used to emphasize/deemphasize the scattering from targeted parts of the sample.

2.2.3 Neutron Diffraction

Diffraction is the result of interference of waves scattered by an object made up of a number of scattering centres. For coherent scattering, the amplitudes of the scattered waves add and the scattering intensity will be the square of the resulting amplitude. We start by considering the scattering of two point centres separated by a distance $\mathbf{r}$, as shown in Fig. 2.4. An incoming wave front with wavenumber $\mathbf{k_0}$ scatters

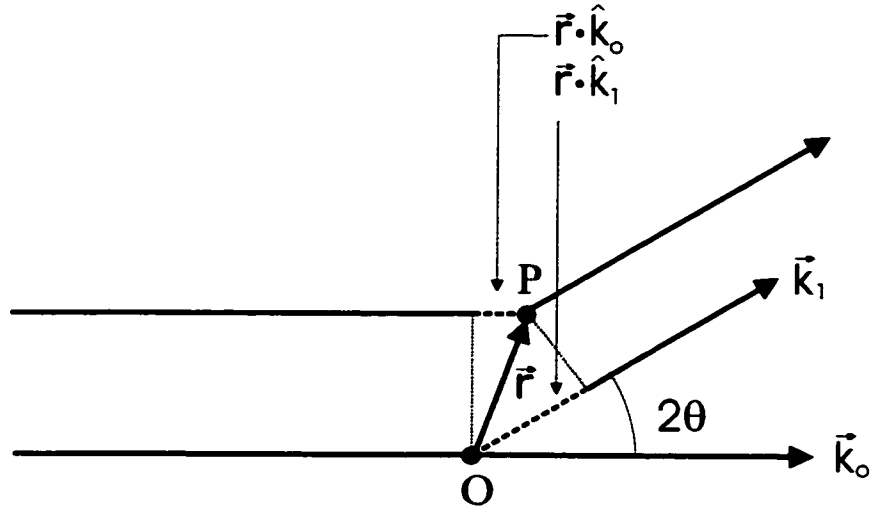

Figure 2.4: Scattering of a wavefront by two point centres.

off the centres at points O and P such that the scattered beam is in the direction given by $\mathbf{k_1}$. A normalized scattered wave can be represented by the complex form $e^{i\phi}$ where the phase, ϕ, is $\frac{2\pi}{\lambda}$ times the distance traveled from some arbitrary reference point. In Fig. 2.4, the path difference of the two scattered waves is indicated by the dashed lines. The upper ray travels an added distance $\mathbf{r} \cdot \hat{\mathbf{k}}_\mathbf{0}$ to reach its scattering centre, P, compared to the lower ray which scatters off centre O. After scattering, the lower ray must then cover the extra distance $\mathbf{r} \cdot \hat{\mathbf{k}}_\mathbf{1}$ before both rays strike a distant detector in the direction of $\mathbf{k_1}$. The phase difference between the scattered waves is then $\frac{2\pi}{\lambda}\ \mathbf{r} \cdot (\hat{\mathbf{k}}_\mathbf{1} - \hat{\mathbf{k}}_\mathbf{0})$. The scattering amplitude in a direction $\mathbf{k}_1$ from the two points scatterers in Fig. 2.4 is then simply

$$F(\mathbf{Q}) = \sum_{(\mathbf{r_o},\mathbf{r_p})} b(\mathbf{r}) e^{-i\mathbf{Q}\mathbf{r}} \tag{2.15}$$

where $\mathbf{Q} = (\mathbf{k_1} - \mathbf{k_0})$ and $b(\mathbf{r})$ is the bound scattering length of the object at $\mathbf{r}$. By using the bound scattering length we are invoking the *static approximation* which assumes that the target molecule is fixed and there is negligible energy transfer to it from the neutron. Correction terms to the static approximation (Placzek 1952)

show that deviations from this assumption are less than 1% for molecules the size of typical phospholipids. For a macroscopic object the number of scatterers is large and the sum can be replaced by an integral:

$$F(\mathbf{Q}) = \int d^3\mathbf{r}\rho(\mathbf{r})e^{-i\mathbf{Q}\mathbf{r}} \tag{2.16}$$

where $\rho(\mathbf{r})$ is the scattering length density and the integral is over the volume of the object. Equation 2.16 shows explicitly that the scattering amplitude in a direction specified by $\mathbf{Q}$ is just the Fourier transform of the scattering density within the object. The scattering intensity is the absolute square of the scattering amplitude:

$$I(\mathbf{Q}) = F^*F = \int\int d^3\mathbf{r_1}d^3\mathbf{r_2}\ \rho(\mathbf{r_1})\rho(\mathbf{r_2})e^{-i\mathbf{Q}(\mathbf{r_1}-\mathbf{r_2})} \tag{2.17}$$

Since this double integral involves only the relative distance $|\mathbf{r_1} - \mathbf{r_2}|$ between every pair of points in the object, it is convenient to perform the integration in two steps: 1) integrate over all points with equal relative distances, and 2) integrate over all possible relative distances. The first step can be written

$$\tilde{p}^2(\mathbf{r}) = \int d^3\mathbf{r}\ \rho(\mathbf{r_1})\rho(\mathbf{r_2})$$
$$with\ r = (|\mathbf{r_1} - \mathbf{r_2}|) = constant \tag{2.18}$$

Evidently, $\tilde{p}^2(\mathbf{r})$ is a measure of the correlation between the scattering length densities at all points in the the sample separated by a distance r, and is known mathematically as an autocorrelation function. The second step is an integral over all separation distances:

$$I(\mathbf{Q}) = \int d^3\mathbf{r}\ \tilde{p}^2(\mathbf{r})e^{-i\mathbf{Q}\mathbf{r}} \tag{2.19}$$

2.2.4 Small Angle Scattering from Surfaces

The scattering of X-rays and neutrons by a surface can provide useful information about its geometrical properties and morphology. Scattering experiments

can be performed on randomly oriented surfaces or single, aligned surfaces. As the systems studied in this thesis are vesicular suspensions, only the theory for the former will be presented here.

Scattering from Smooth Surfaces: Porod's Law

To simplify our derivation, we make two assumptions which are generally met in small angle scattering (Porod 1982) and certainly apply to the systems studied in this thesis:

(1) The system is statistically isotropic.

(2) There exists no long range order. That is, there is no correlation between points separated widely enough.

Assumption (1) implies that $\tilde{\rho}^2(\mathbf{r})$ will depend only on the magnitude of $\mathbf{r}$. In addition, the phase factor $e^{-i\mathbf{Q}\mathbf{r}}$ can be replaced by its average taken over all directions of $\mathbf{r}$ (Debye 1915):

$$\langle e^{-i\mathbf{Q}\mathbf{r}} \rangle = \frac{sin\ Qr}{Qr} \tag{2.20}$$

so we can write 2.19 in the form

$$I(Q) = \int 4\pi r^2 dr\ \tilde{\rho}^2(r) \frac{sin\ Qr}{Qr} \tag{2.21}$$

According to assumption (2), the scattering length densities should become independent (i.e. uncorrelated) at large r and can be replaced by a mean value $\bar{\rho}$. The auto-correlation function defined by 2.18 will then approach an asymptotic value, $V\bar{\rho}^2$. An object with constant scattering density throughout cannot contribute to the diffraction pattern so the scattering from our object must be due to the finite region where $\tilde{\rho}^2$ varies from its asymptotic value. Therefore we can eliminate the "background" and use, equivalently, the scattering density fluctuation $\eta = \rho - \bar{\rho}$ in

place of ρ, substituting

$$\tilde{\eta}^2(r) = \widetilde{(\rho - \bar{\rho})}^2 = \tilde{\rho}^2 - V\bar{\rho}^2 = V \cdot \gamma(r) \tag{2.22}$$

for Eq. 2.18 as necessary. Here we have introduced the correlation function (Debye, Anderson & Brumberger 1957) which can be interpreted as the average of the product of two fluctuations separated by a distance r:

$$\gamma(r) = \langle \eta(r_1) - \eta(r_2) \rangle \quad with\ r = |r_1 - r_2| = constant \tag{2.23}$$

We can now write Eq. 2.21 as

$$I(Q) = \int_0^\infty 4\pi r^2 dr\ \gamma(r) \frac{sin\ Qr}{Qr} \tag{2.24}$$

Our vesicular samples constitute a dilute solution of particles embedded in a solvent of constant scattering length density ρ_0. The headgroups forming the surface of our particles (vesicles) will be considered to have constant scattering length density ρ. We will ignore the acyl chains as they will not contribute to the surface scattering. As argued above, only differences in scattering length density, $\Delta\rho = (\rho - \rho_0)$, are relevant for diffraction so we will rewrite $\gamma(r)$ as the product of this constant density difference and a function $\gamma_0(r)$ that depends only on the geometry of the particle:

$$\gamma(r) = (\Delta\rho)^2 \cdot \gamma_0(r) \tag{2.25}$$

Guinier & Fournet (1955) identify $\gamma_0(r)$ as the probability that a given point at a distance r from an arbitrary reference point within the particle will itself be contained within the particle. It immediately follows that $\gamma_0(0) = 1$ and $\gamma_0(r \geq D) = 0$ where D is the maximum particle dimension. This interpretation leads to a convenient geometric definition of $\gamma_0(r)$ (Porod 1982, Singh & Barberato 1997). Imagine that the particle is duplicated and shifted by a vector $\mathbf{r}$ as shown in Fig. 2.5. The volume in common between the particle and its twin is denoted $\hat{V}(\mathbf{r})$. Averaging over all

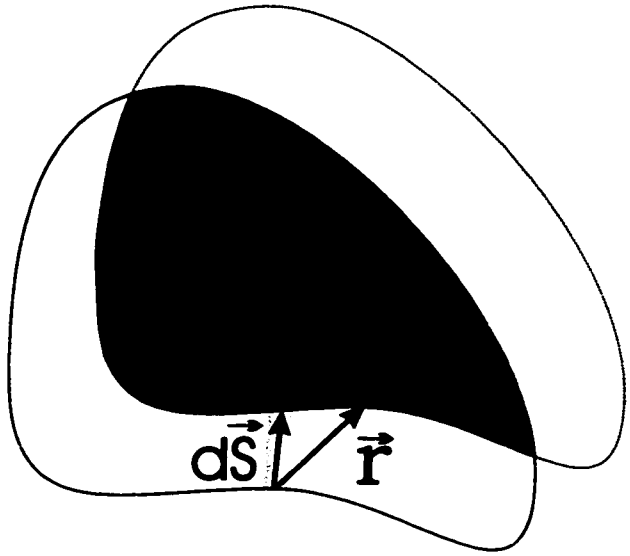

Figure 2.5: Geometric definition of the common volume, $\hat{V}(\mathbf{r})$, denoted by the dark shaded region defined by the intersection of the particle and itself after being displaced by $\mathbf{r}$. The lightly shaded region is meant to represent the differential change in volume of the surface element $\mathbf{dS}$ when displaced by $\mathbf{r}$.

directions of $\mathbf{r}$ measures the average common volume which can then be related to the characteristic function as

$$\gamma_0(r) = \frac{\langle \hat{V}(\mathbf{r}) \rangle}{V} \tag{2.26}$$

With reference to Fig. 2.5, we see that for small displacements of r, the common volume $\hat{V}$ differs from V only by a shift of the surface. Denoting a surface element by its inward normal, $\mathbf{dS}$, the reduction in volume resulting from a shift $\mathbf{r}$ of this surface element is just $\mathbf{r} \cdot \mathbf{dS} = r\mathrm{d}S\cos\phi$. To calculate $\langle \hat{V}(\mathbf{r}) \rangle$ we must average over all directions of $\mathbf{r}$ which is equivalent to averaging over $\cos\phi$ for positive values of ϕ. The common volume is restricted to points where $\mathbf{r}$ is directed inward, so we will average only over these values, reducing the average by a factor of $\frac{1}{2}$. For small r, we

can expand the characteristic function as

$$\begin{aligned}\gamma_0(r) &= \frac{\langle \hat{V}(\mathbf{r}) \rangle}{V} \approx \frac{\langle V - rdScos\ \phi \rangle}{V} \\ &= 1 - \frac{\overline{|cos\ \phi|}}{2}\ \frac{S}{V} r = 1 - \frac{S}{4V} r \end{aligned} \tag{2.27}$$

We can now write Eq. 2.24 as

$$\begin{aligned} I(Q) &= (\Delta\rho)^2 \int_0^D 4\pi r^2 dr\ \frac{\langle \hat{V}(\mathbf{r}) \rangle}{V}\ \frac{sin\ Qr}{Qr} \\ &\approx \frac{(\Delta\rho)^2}{V} \int_0^D 4\pi r^2 dr\ \left(1 - \frac{S}{4V} r\right)\ \frac{sin\ Qr}{Qr} \\ &= \frac{4\pi(\Delta\rho)^2}{VQ^3} \int_0^{QD} dy\ (y - \frac{S}{4VQ}\ y^2)\ sin\ y \qquad (with\ y = Qr) \\ &= \frac{2\pi(\Delta\rho)^2 S}{V^2}\ \frac{1}{Q^4} + O(Q^{-6}) \end{aligned} \tag{2.28}$$

Equation 2.28 shows explicitly that the leading term of the scattering intensity goes as Q^{-4}. This is the well known Porod law derived independently by Porod (1951) and Debye et al. (1957). Despite the restrictions used in the derivation, the applicability of Porod's law has proven to be more universal than might be expected (Porod 1982). The fourth power law behaviour is valid for single particles, densely packed systems, and systems where the particle size varies (as is the case with our MLVs). Extensions of the Porod law has been have been used in some systems to take into account higher order terms (Sobry, Ledent & Fontaine 1991) or to account for the continuous nature of the scattering length density transition at real interfaces (Schmidt 1991, Ruland 1971), but these refinements will not be considered here.

Scattering from Rough Surfaces

Nature, of course, is not all smooth surfaces and discrete boundaries. Real surfaces or interfaces are often rough, disordered, or poorly defined. Although disorder can often complicate the analysis of scattering data, there are cases where a high

degree of disorder can facilitate the application of concepts and techniques which simplify the analysis (Schmidt 1991). Disordered systems with a fractal nature fit this description. The ideas of fractal geometry (Mandelbrot 1983) have proved useful in many areas of the physical sciences (Avnir, Farin & Pfeifer 1984) including the analysis and interpretation of small angle scattering data.

One class of fractals which has been studied using small angle scattering techniques is the surface fractal (Martin & Hurd 1987). A surface fractal is an object embedded in space of Euclidean dimension d bounded by a fractal surface with dimension $d_s < d$ (Schmidt 1991). The lower limit on d_s occurs for smooth surfaces for which $d_s = d - 1$. Derivations of the expected behaviour of the small Q scattering from such objects show that the intensity follows a surprisingly simple form (Bale & Schmidt 1984, Kjems & Freltoft 1985):

$$I(Q) = I_{0s}\ \Gamma(5-2d)\ sin[\frac{\pi}{2}(2d-1)]\ Q^{-(2d-d_s)} \tag{2.29}$$

where I_{0s} is a constant and $\Gamma(5-2d)$ is the gamma function. This form of the scattering will apply when $Q\xi \gg 1$ where ξ is a measure of the particle size. As was the case for smooth surfaces, power law behaviour for small Q is seen. In fact, for a smooth surface, $d_s = d - 1$, in three dimensions, the Porod law is recovered and can thus be considered a special case of the more general form given by Eq. 2.29. From the bounds on d_s, it is apparent that any amount of interfacial roughness will serve to decrease the power law exponent and slow the fall off of the intensity with Q.

Strictly speaking, a true fractal is a geometrical structure which is scale invariant and therefore often referred to as *self similar*. No naturally occurring system will satisfy this definition, but fractal power law behaviour will nevertheless be seen as long as the system displays fractal-like characteristics in the range of length scales probed by the scattering experiment. In fact, the power law form is quite robust, being preserved for systems exhibiting power law roughness, and for rough interfaces

averaged over all orientations (Wong & Bray 1988). This latter case probably best describes the situation with our vesicular systems.

2.2.5 The SANS Spectrometer

All of the neutron scattering work reported in this thesis was conducted in a series of three experiments at the W.C. Koehler 30 metre SANS spectrometer at the National Center for Small-Angle Scattering at Oak Ridge National Laboratory (Koehler 1986). Figure 2.6 shows a schematic of the apparatus. The neutron source is the High Flux Isotope Reactor (HFIR) which normally operates at 100 MW. Thermal neutrons from the reactor core emerge from a beam port and pass through a beryllium filter which effectively eliminates neutrons with wavelengths less than four Angstroms. The beam is monochromatized to 4.75 Å, with $\frac{\Delta\lambda}{\lambda} = 5\%$, by Bragg reflection from two graphite crystals. The incident beam flux is monitored by a low-efficiency neutron proportional counter before entering the double-slit 7.6 metre long evacuated flight path. Waveguides can be used in the flight path to increase the flux at the sample, but none were used in our setup. The slits at either end of the flight path define the size of the transmitted beam which is blocked from hitting the detector by a 4 cm beam stop. The multidetector covers an area of 64 x 64 cm^2 and consists of 4096 detector elements. With the detector a distance L from the sample, scattered neutrons striking the detector a distance D from its centre define the scattering angle 2θ. Since L is large compared to D, the scattering wavevector can be written

$$Q = \frac{4\pi}{\lambda} \, Sin \, \theta \approx \frac{4\pi}{\lambda} \, tan \, \theta = \frac{2\pi}{\lambda} \frac{D}{L} \tag{2.30}$$

and with the range of detector distances available, Q can be made to span approximately two decades, from 0.003 to 0.3 $Å^{-1}$.

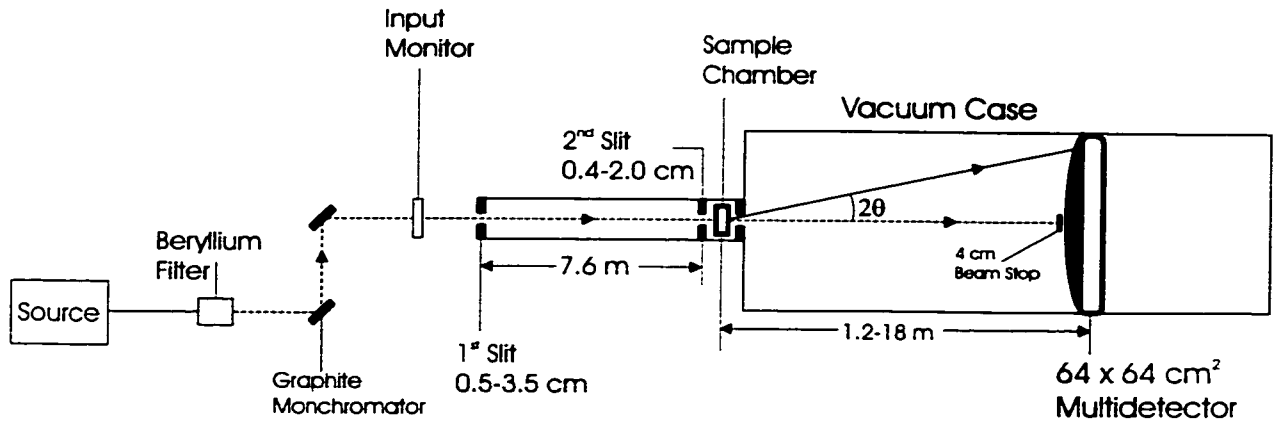

Figure 2.6: Schematic of the 30 metre SANS at the National Center for Small-Angle Scattering at Oak Ridge National Laboratory.

2.3 X-ray Diffraction

The scattering and diffraction concepts presented in the previous sections apply equally well to X-ray diffraction with some modifications that will be noted here. X-ray diffraction is an older field than its neutron counterpart with the first observation of X-ray diffraction from a crystalline material occurring in 1912 (Friedrich, Knipping & Laue 1912), a full twenty years before Chadwick's discovery of the neutron.

As X-rays are a form of electromagnetic radiation, they will interact strongly with the electronic cloud of an atom. Strictly speaking, this interaction should be treated quantum mechanically, but it turns out that a purely classical calculation is sufficient to derive most of the results of import. A particularly lucid treatise on X-ray scattering is given by Warren (1990). The Bragg law (Eq. 2.2) will apply equally well for X-rays and the results in section 2.2.4 remain valid by replacing the neutron scattering length density with the electron density function and with a change of the constants.

There are a number of notable differences between the two scattering tech-

niques. Since X-rays scatter from the electron cloud, the scattering power of an atom will scale with Z, the atomic number. For this reason light atoms such as hydrogen, a principle component of any biological material, are very weak scatterers. Unlike neutron diffraction then, it is difficult to vary the contrast of a sample since to do so means substitution of a different element which can drastically affect the relevant chemistry. Another difference is the contrast in the apparent size of the scattering centres. For neutrons the nuclei act as point scatterers, but for X-rays the scattering centres have the dimensions of the atom. As a result the atomic form factor, which is analogous to the scattering length, will have an angular dependence although for the small angles probed in the studies reported here this will not be significant. Because X-rays scatter from electrons through an electromagnetic interaction, there is no incoherent scattering associated with different probe-target spin states as there is in neutron scattering. There is an incoherent contribution due to Compton scattering, but as this varies directly with scattering angle it will also be of no issue in this study. Finally, ionization effects from intense X-ray irradiation can damage biological samples but no such effects were seen in any of our work.

X-ray diffraction was used to advantage (see chapter 3) in our studies. The improved resolution that can be achieved with X-rays is an effective way of resolving closely spaced scattering features that are indistinguishable with neutrons. In addition, because X-rays and neutrons scatter from different components of the sample, the intensity of scattering peaks can be quite different for each case. For this reason, a barely discernible peak using one technique may appear clearly using the other.

X-ray diffraction experiments were performed using an 18 KW rotating anode and triple axis diffractometer. Figure 2.7 shows a schematic of the X-ray diffractometer used in the experiments reported in this thesis. X-rays are produced when electrons boiled from a filament strike a rotating copper anode. In our experiments,

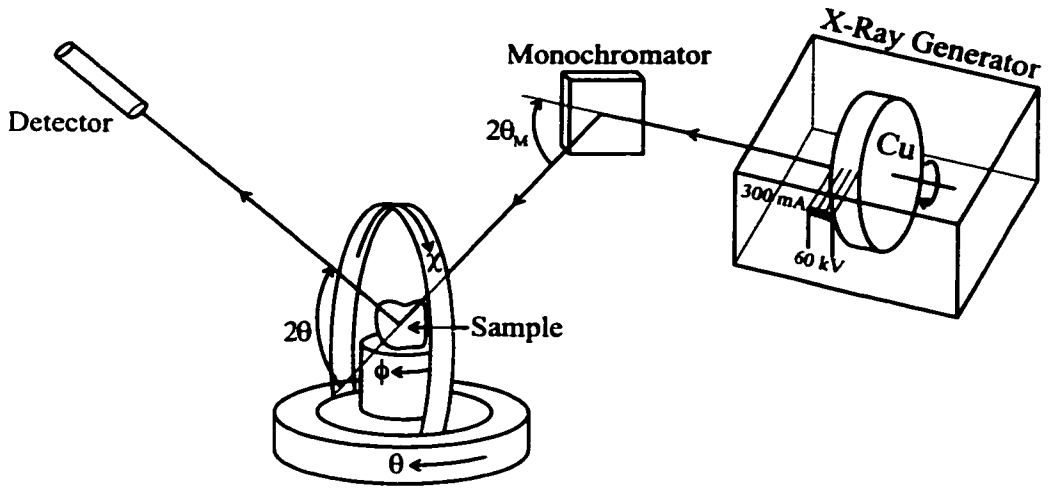

Figure 2.7: Schematic of the X-ray diffractometer (from Lumsden (1998)).

the radiation was monochromated by a pyrolytic graphite monochromator using the (002) reflection which allows passage of both the Kα and Kβ radiation. The Kβ is eliminated by judicious manipulation of the scattering slit geometries. The sample sits in an Eulerian cradle which allows a wide range of orientations, defined by the angles θ, ϕ, and χ, to be accessed without remounting the sample. In our experiments, on what are essentially powder samples, none of the Euler angles were altered once they were optimized to produce maximal scattering from the sample. The scattered X-rays are detected by a NaI scintillation counter at the scattering angle 2θ. It should be noted that the position of the detector, 2θ, is not correlated to the Euler angle θ.

Chapter 3

Metastability in DPPC MLVs

This chapter incorporates the article "Small-angle scattering studies of the fully hydrated phospholipid DPPC" which, at the time of printing, has been peer-reviewed and accepted for publication in Physical Review E.

Small-angle scattering studies of the fully hydrated phospholipid DPPC

P.C. Mason and B.D. Gaulin

Department of Physics and Astronomy, McMaster University,

Hamilton, Ontario, L8S 4M1, Canada

R.M. Epand

Department of Biochemistry, McMaster University,

Hamilton, Ontario, L8N 3Z5, Canada

G.D. Wignall and J.S. Lin

Center for Small-Angle Scattering Research, Oak Ridge National Laboratory,

Oak Ridge, Tennessee 37831, USA

Abstract

Small angle neutron and x-ray scattering studies have been carried out on fully hydrated dipalmitoylphosphatidylcholine (DPPC) multilamellar vesicles. This system is known to exhibit two distinct ripple ($P_{\beta'}$) phases, which depend on sample history, at temperatures intermediate to its high temperature liquid crystalline (L_α) phase, and its low temperature gel ($L_{\beta'}$) phase. On cooling from the L_α phase, the $P_{\beta'}$ phase displays a complex multipeak diffraction pattern that differs significantly from the diffraction pattern seen in the $P_{\beta'}$ phase obtained on warming from the $L_{\beta'}$ phase. Examining the $P_{\beta'}$ phase on cooling using small angle neutron scattering and x-ray diffraction techniques leads to the conclusion that this phase is characterized by a

long wavelength ripple ($\lambda_r \sim 330$Å) and a highly monoclinic unit cell ($\gamma \sim 125°$). As the $P_{\beta'}$ phase is traversed in temperature, the ripple wavelength changes significantly while the monoclinicity remains unchanged. Ripples from the $P_{\beta'}$ phase are seen to persist into the $L_{\beta'}$ phase on cooling, leading to increased small angle scattering characteristic of a disordered stacking of the lamellae.

©1998 The American Phyical Society

I. INTRODUCTION

The rich phase behaviour of phospholipid bilayers and their structural relationship to biological membranes have motivated scientists from many disciplines to examine their unique properties. In excess water, phospholipids self-assemble into multilamellar vesicles (MLVs) consisting of concentric, stacked bilayers each separated by a layer of water. The repetition of structure lends itself well to diffraction studies. Perhaps the most scrutinized of all model membranes, dipalmitoylphosphatidylcholine (DPPC) continues to be a source of intrigue. In particular the novel ripple $P_{\beta'}$ phase of DPPC (and other PCs) has been the source of much recent study and debate [1–4]. The $P_{\beta'}$ phase, characterized by the development of a long periodicity corrugation of the bilayer lamellae, is an intermediate phase spanning a relatively narrow ($\sim$ 8 °C) temperature range between the low temperature gel ($L_{\beta'}$) and high temperature liquid crystalline (L_{α}) phases. Among the fascinating properties of this phase is its non-equilibrium behaviour first reported by Tenchov *et al.* [5] in which the diffraction pattern obtained after slowly cooling the sample from the L_{α} phase is markedly different than that seen after warming the sample into the $P_{\beta'}$ phase from the $L_{\beta'}$ phase.

Yao *et al.* [6] concluded that the $P_{\beta'}$ phase on cooling in DPPC consists of two coexisting ripple structures. Their model proposes that there is phase coexistence between regions of the ripple phase identical with that obtained on warming, and regions for which the ripple wavelength is approximately two times greater. The diffraction pattern would then be a superposition of the patterns obtained from each of these regions. In this paper, we discuss small angle neutron and x-ray scattering studies of fully hydrated DPPC in the temperature regime ($\sim$ 20 °C to 50 °C) wherein

it displays all three of the $L_{\beta'}$, $P_{\beta'}$, and L_{α} phases, paying particular attention to the $P_{\beta'}$ ripple phase and the history dependence of the structure within this phase. While our diffraction data is similar to that obtained by Yao *et al.* [6], we show that both our data and that obtained by Yao *et al.* [6] can be understood in terms of a well ordered, highly monoclinic, single wavelength structure occurring on cooling, and a less-well-ordered single wavelength structure occurring on warming. In addition, we show that a related history dependence exists for the $L_{\beta'}$ phase, with disordered ripples persisting into the $L_{\beta'}$ phase when it is entered from above in temperature.

II. MATERIALS AND EXPERIMENTAL METHODS

1,2-dipalmitoyl-sn-glycero-3-phosphocholine (DPPC) and DPPC in which the hydrogens in the quaternary ammonium methyl groups have been replaced with deuterium (DPPC-d_9) were purchased from Avanti Polar Lipids, Inc. (Birmingham, AL) and used without any further purification.

For the small angle neutron scattering (SANS) experiments, 50 mg of DPPC-d_9 was suspended in 0.5 mL D_2O/PIPES buffer (20 mM PIPES, 1mM EDTA, 150 mM NaCl in D_2O adjusted to a pH meter reading of 7.4). This buffer simulates physiological conditions. The solution was centrifuged and transfered to a 1 mm pathlength Helma quartz cell and incubated at 45 °C for at least 24 hours. Excess water was drawn off and more suspension was transfered into the cell. After incubating a second time, a small amount of water was visibly separated from the remainder of the solution, confirming that the sample was in a state of excess water. An undeuterated DPPC sample was prepared in the D_2O buffer following the same procedure. The DPPC sample used in the x-ray samples were prepared in a similar manner except

with H_2O substituted for the D_2O. The x-ray samples were placed in 1.5 mm diameter $\oslash$ glass capillaries and visually inspected before use to ensure that they satisfied the excess water condition.

The SANS experiments were conducted at the W.C. Koehler 30 m SANS facility at the Oak Ridge National Laboratory [7] using neutrons of wavelength 4.75 $\AA$ ($\delta\lambda/\lambda \sim 5\%$). Two configurations of the instrument were employed with sample to detector distances of 3.5 m ($Q \in [0.019, 0.17\ \AA^{-1}]$) and 8.0 m ($Q \in [0.008, 0.075\ \AA^{-1}]$), for relatively low and high resolution measurements, respectively. The SANS data were corrected for instrumental backgrounds and detector efficiency and converted into absolute differential cross sections per unit sample volume using established protocols [8,9].

As a complement to the neutron work, x-ray diffraction experiments were conducted using Cu Kα radiation from an 18 kW rotating anode generator which was further monochromated using a pyrolytic graphite monochromator. The resolution of the x-ray measurements was roughly a factor of two better than that of the neutron measurements at a sample-to-detector distance of 3.5 m, which allowed fine structure within the diffraction pattern to be resolved. While neutrons and x-rays are similar diffraction probes, neutrons scatter from the nuclei in atoms while x-rays scatter off the electronic charge distribution, and consequently the use of the two techniques in tandem is expected to yield complementary information regarding the same structure.

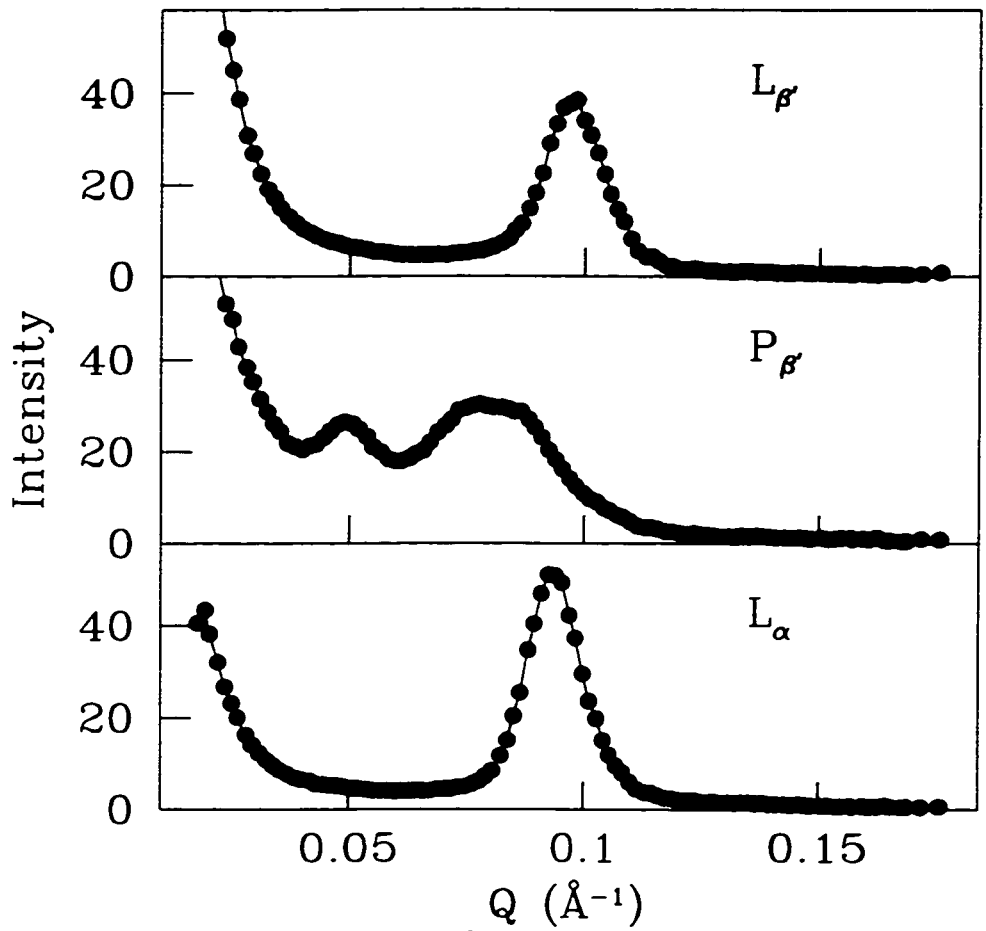

FIG. 1. Typical SANS profiles of DPPC in its three phases obtained on cooling. From top to bottom, data within the $L_{\beta'}$ (gel) at T=20°C, $P_{\beta'}$ (ripple) at T=39°C, and L_{α} (liquid crystal) phase at T=45°C.

III. RESULTS AND DISCUSSION

A. Experimental Results

Figure 1 shows the low resolution (3.5 m) SANS diffraction pattern for DPPC-d_9 in three different phases obtained on cooling. The phases are clearly distinguished by the shift in the lamellar repeat peak and the changes in the scattering intensity below $Q = 0.05$ Å^{-1} . The evolution of the diffraction pattern as a function of temperature can be better appreciated when presented as a contour plot, as shown in Figs. 2 and 3 for the warming and cooling runs, respectively.

Figure 2 shows a color contour plot of low resolution neutron data taken while slowly warming the DPPC-d_9 from 20 °C to 55 °C. Data collection began five minutes after the temperature had stabilized to within ±0.1 °C of the target temperature, following a change in temperature. Each measurement set was taken over a period of 30 minutes. Temperature steps of 0.5 °C were taken in the range from $T = 31$ °C to $T = 43$ °C. Additional measurements were also performed before and after the main measurement at one temperature in each phase for comparative purposes in order to ensure that relaxation kinetics were not affecting the results. No such effect was observed at any temperature.

The three phases of DPPC in the temperature range shown in Fig. 2 are easily identified by the rather abrupt changes in the overall pattern, including a shift in position of the lamellar repeat peak and dramatic changes in the the very low angle scattering ($Q = \frac{4\pi}{\lambda} sin\,\theta < 0.03$ Å^{-1}). This latter scattering increases strongly upon entering the $P_{\beta'}$ phase from the $L_{\beta'}$ phase and subsequently falls in the L_α phase. The inset shows data from a separate, higher resolution (8.0 m) experiment conducted to examine the region enclosed by the white box in Fig. 2.

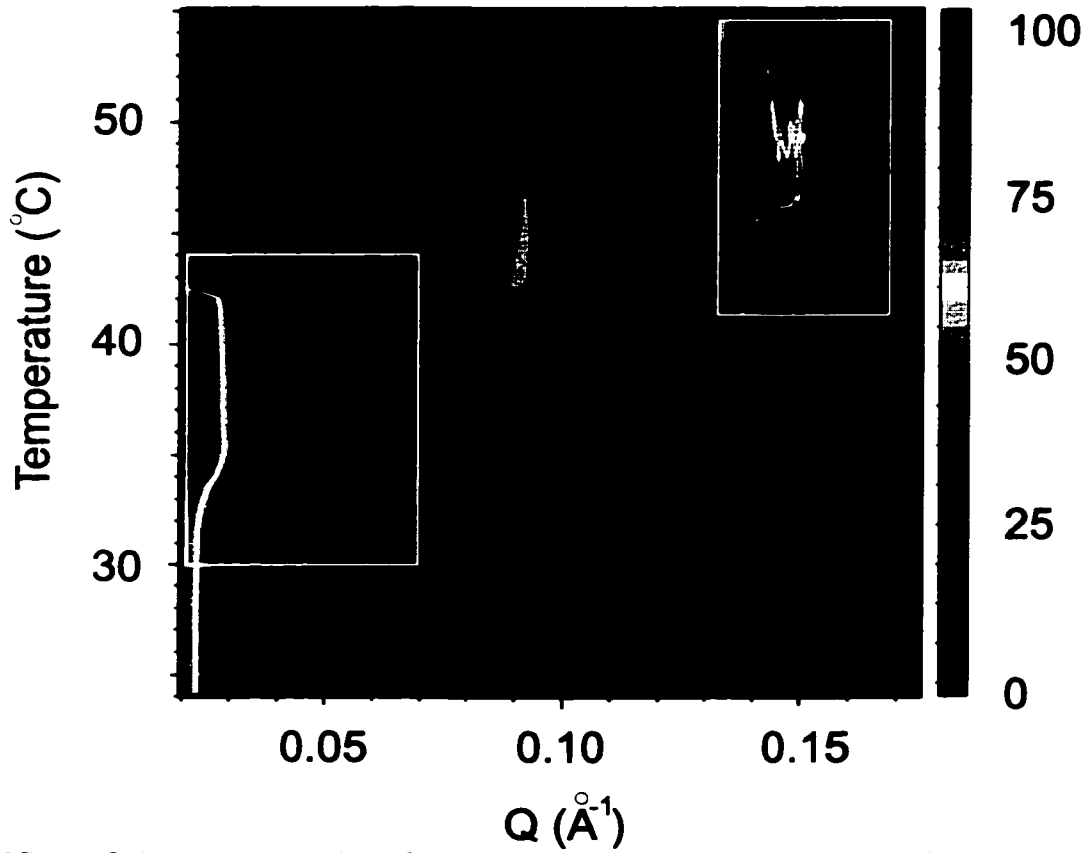

FIG. 2. Colour contour plot of DPPC-d_9 in excess water warming through its three phases ($L_{\beta'}$,$P_{\beta'}$,L_α) in this temperature range. The main plot shows neutron data taken with a sample to detector distance of 3.5 m ($Q \in [0.019, 0.17\ \text{Å}^{-1}]$). The inset shows data from a separate, 8.0 m experiment corresponding to the region enclosed by the white box ($Q \in [0.02, 0.075\ \text{Å}^{-1}]$).

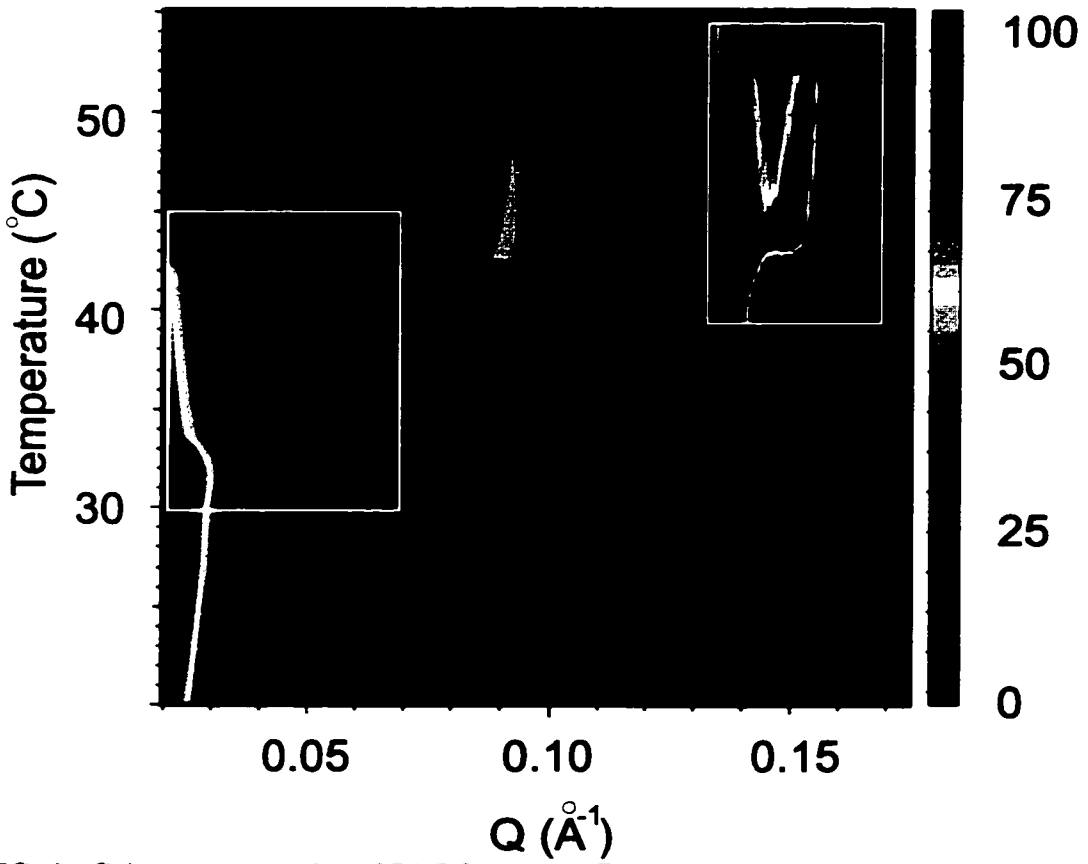

FIG. 3. Colour contour plot of DPPC-d_9 as in Fig. 2. but with the sample slowly cooled through this temperature range.

Neutron scattering profiles of DPPC-d_9 as the same sample was slowly *cooled* are shown in Fig. 3. Similar thermal protocol as described above was employed. The scattering due to the ripple periodicity in the $P_{\beta'}$ phase ($Q \sim 0.05$ Å^{-1}) is much more prominent on cooling and the low angle scattering is markedly different. In the cooling scans, the very low Q scattering in the $P_{\beta'}$ phase, while more intense than that of the L_α phase, does not approach the levels attained in the warming scans and reaches its highest intensity in the $L_{\beta'}$ phase. The undeuterated DPPC sample displayed similar scattering profiles which are not shown in this paper.

Figure 4 shows the complementary x-ray and neutron diffraction patterns obtained by these two techniques for DPPC warmed into the $P_{\beta'}$ phase. Both data sets were taken at T=39 °C and the x-ray data has been scaled arbitrarily so that the data sets overlap. The lamellar repeat peak at Q=0.086 Å^{-1} exhibits roughly the same width in both data sets, indicating that this is a single Bragg-like feature whose intrinsic width implies the presence of disorder. The neutron data also show a shoulder related to the ripple periodicity near Q=0.05 Å^{-1} which does not appear in the x-ray profile corresponding to a ripple wavelength of $\lambda_r \sim 125\AA$ in the ripple phase on warming, in agreement with previous freeze-fracture measurements [10] but slightly less than previous x-ray diffraction results [6,11]. In contrast, the data shown in Fig. 5, collected after cooling slowly into the $P_{\beta'}$ phase from the L_α phase, show an enhanced neutron peak from the ripple periodicity near Q=0.05 Å^{-1} and the peak attributed to the lamellar repeat appears much broader. The higher-resolution x-ray cooling data show that this broad peak is, in fact, made up of two closely spaced peaks at Q=0.072 Å^{-1} and Q=0.087 Å^{-1} that are not fully resolved by the neutrons. In addition, the x-rays reveal a peak at Q=0.10 Å^{-1} which does not appear in the neutron profile.

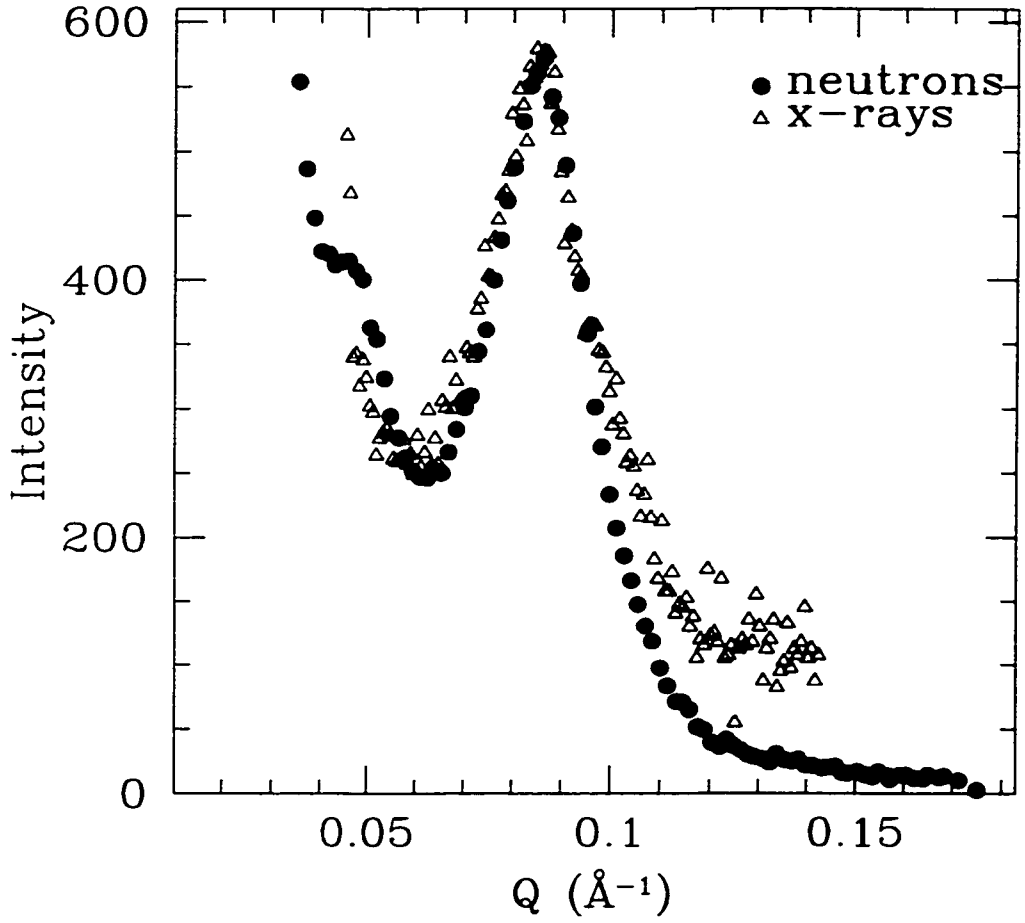

FIG. 4. A comparison of neutron and x-ray scattering profiles of DPPC-d_9 in the $P_{\beta'}$ phase (both at T=39°C) after warming from the $L_{\beta'}$ phase.

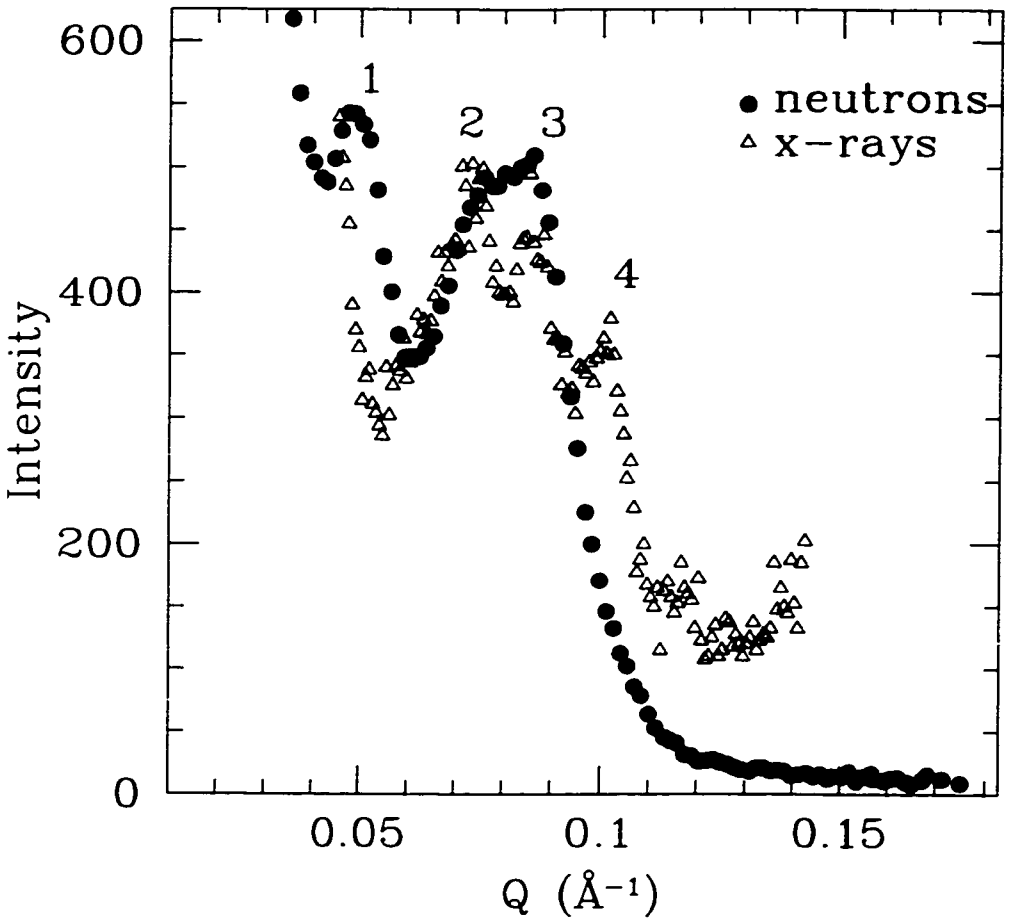

FIG. 5. A comparison of neutron and x-ray scattering profiles of DPPC-d_9 in the $P_{\beta'}$ phase (both at T=39°C) after slow cooling from the L_α phase.

B. Modelling the Ripple Phase

It is well known [1,12] that the ripple phase can be described by a two-dimensional monoclinic lattice, shown schematically in Fig. 6, where the unit vectors are given by:

$$\vec{a} = d\,cot\,\gamma\,\hat{x} + d\,\hat{z} \;\; and \;\; \vec{b} = \lambda_r\,\hat{x} \tag{1}$$

where d is the lamellar repeat distance, λ_r is the ripple wavelength, and the difference between γ and 90° is a measure of the monoclinicity. The reciprocal lattice vectors are then:

$$\vec{A} = \frac{2\pi}{d}\,\hat{z} \;\; and \;\; \vec{B} = \frac{2\pi}{\lambda_r}\,\hat{x} - \frac{2\pi}{\lambda_r tan\,\gamma}\,\hat{z} \tag{2}$$

The absolute form factors reported by Wack and Webb [12] for the $P_{\beta'}$ phase of the related phospholipid DMPC suggest that the strongest peaks for the low Q range should correspond to the $(1\bar{1})$, (10), and (11) reflections. If we assume that these reflections are peaks 2,3, and 4 respectively in Fig. 5, we must conclude that peak 1 is the (02) reflection in order to obtain reasonable values for our unit cell. These assignments give d = 73 Å, in agreement with the value obtained on warming and with other measurements, [12] λ_r = 330 Å, and γ = 126°. Long wavelength ripples of this order have been reported previously but not with an accompanying large monoclinicity [6,13].

A consequence of our assignment of peak 1 in Fig. 5 as the (02) reflection is that we should expect to see the (01) reflection at a Q value half that of (02). Figure 7 shows the high resolution (8 m) neutron profile of DPPC-d_9 at 39 °C within the $P_{\beta'}$ phase on cooling, along with a non-linear least square fit to the data. The pattern could not be adequately fit with a power law background and a single Lorentzian

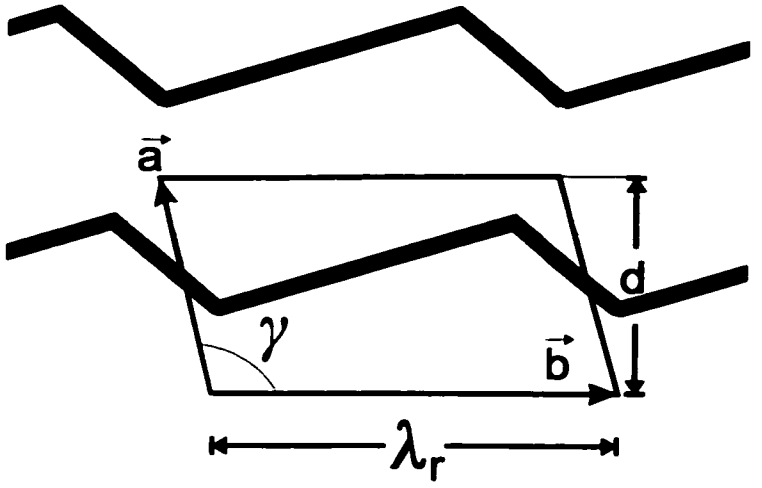

FIG. 6. A schematic drawing of the monoclinic unit cell of DPPC in the $P_{\beta'}$ phase. The cell is uniquely defined by the bilayer periodicity, d, ripple wavelength, λ_r, and monoclinic angle, γ.

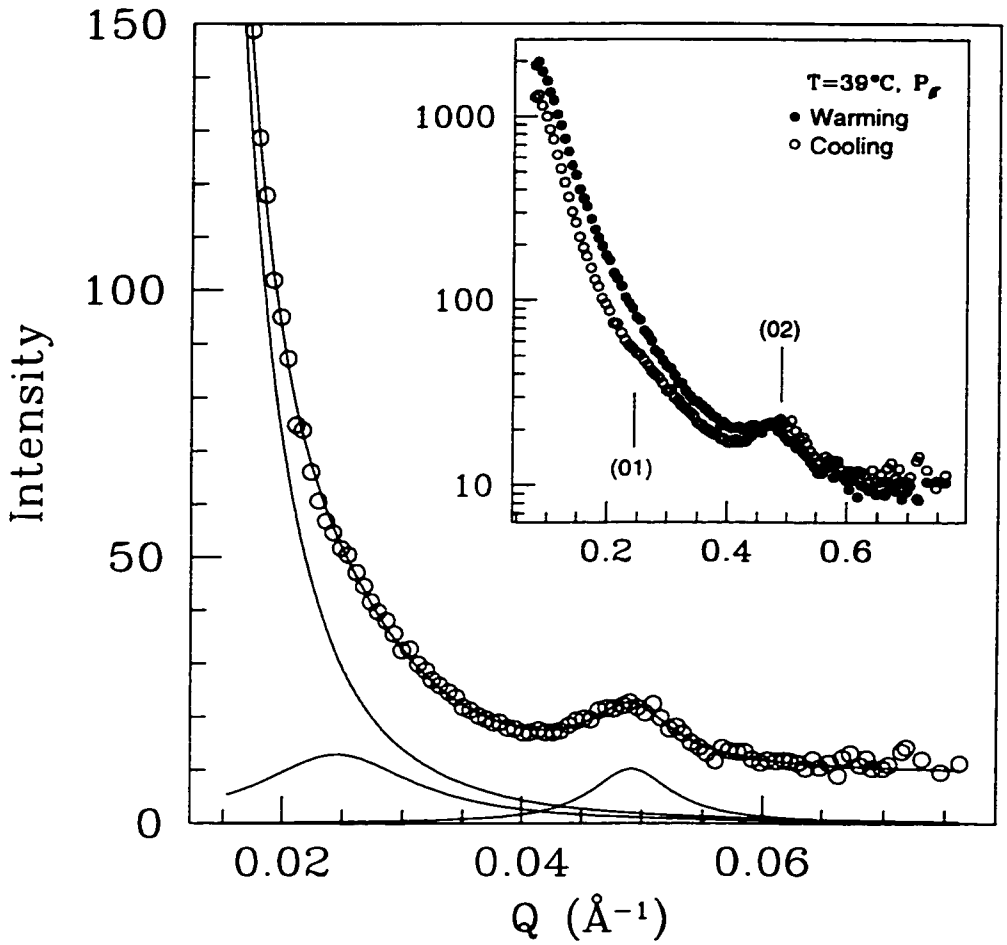

FIG. 7. A fit to the high resolution (8.0 m) neutron data of DPPC-d_9 in the $P_{\beta'}$ phase is shown. The main plot shows the data on a linear scale along with the fit. The three components of the fit: the power law background and two Lorentzians, are also included. The inset compares the profiles of the $P_{\beta'}$ phase obtained on warming and cooling on a semi-log scale.

centered at $Q \sim 0.05$ Å^{-1}, but the addition of a second Lorentzian at half this Q value describes the data well. The inset shows the same cooling data on a semi-log scale, along with the corresponding profile obtained on warming. In this plot the (01) peak is clearly discernible in the raw data of the cooling scan and is absent in the warming data.

Figure 8 shows the x-ray diffraction profile of DPPC in the $P_{\beta'}$ phase on cooling taken from Yao *et al.* [6] As already discussed, these authors interpreted this profile as the superposition of two different rippled regions, each with it's own ripple wavelength, bilayer periodicity, and monoclinicity. However, the single, long wavelength ripple phase model which we constructed to describe our diffraction data, *also describes their diffraction data.* This can be seen in Fig. 8 and Table 1, where we directly compare the measured and calculated peak positions using a model structure for which $\lambda_r = 350$ Å, $d = 71$ Å, and $\gamma = 129°$. These results agree well with the results from our experiments, with the greatest discrepency being a 6% difference in the ripple wavelength. The vertical lines in Fig. 8 indicate the calculated peak positions of the Bragg reflections in the given range. Only reflections up to third order are shown. The measured and calculated peak positions are summarized in Table 1. This yields an excellent description of the Yao *el al.* [6] data. The single phase structure we suggest is also consistent with the decrease in diffuse scattering observed at small Q compared with the ripple phase obtained on warming. A superposition of two rippled structures would be expected to give rise to increased diffuse scattering due to disorder, which is not observed.

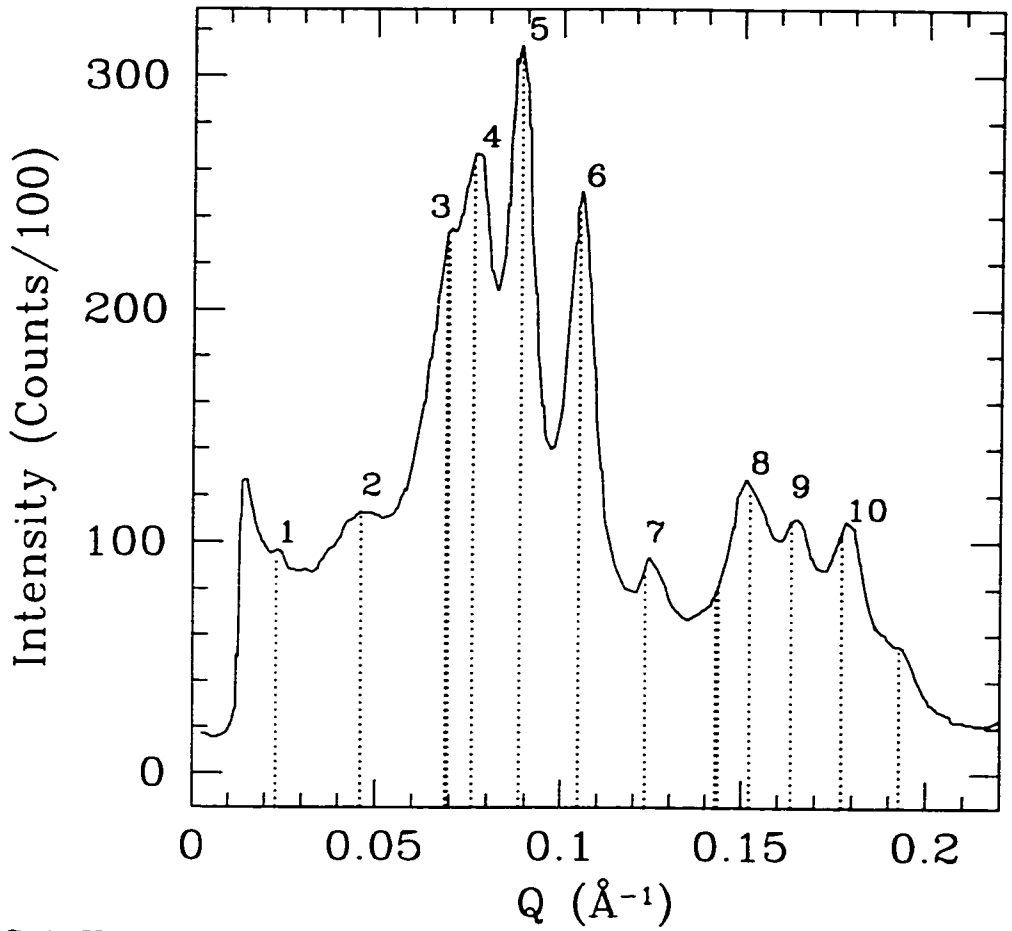

FIG. 8. X-ray diffraction profile of DPPC in the $P_{\beta'}$ phase on cooling (taken from Yao *et al.* (1991)). The vertical lines indicate expected peak positions calculated using our model and detailed in Table 1.

TABLE I. Calculated and measured peak positions of DPPC in the $P_{\beta'}$ phase on cooling. Peak number correspond to the labels shown in Fig. 8. Only reflections up to third order are shown. The question marks (?) in the Peak Number column correspond to calculated reflections which were not labeled in the Yao *et al.* (Ref. 6) work.

Peak Number	Peak label (hk)	Calculated ($Å^{-1}$)	Measured ($Å^{-1}$)
1	(01)	0.023	0.023
2	(02)	0.046	0.046
3	(03)	0.069	0.070
	$(1\bar{2})$	0.069	
	$(1\bar{3})$	0.070	
4	$(1\bar{1})$	0.076	0.077
5	(10)	0.089	0.089
6	(11)	0.118	0.119
7	(12)	0.123	0.124
?	(13)	0.143	
	$(2\bar{3})$	0.144	
8	$(2\bar{2})$	0.152	0.152
9	$(2\bar{1})$	0.164	0.164
10	(20)	0.177	0.178
?	(21)	0.193	

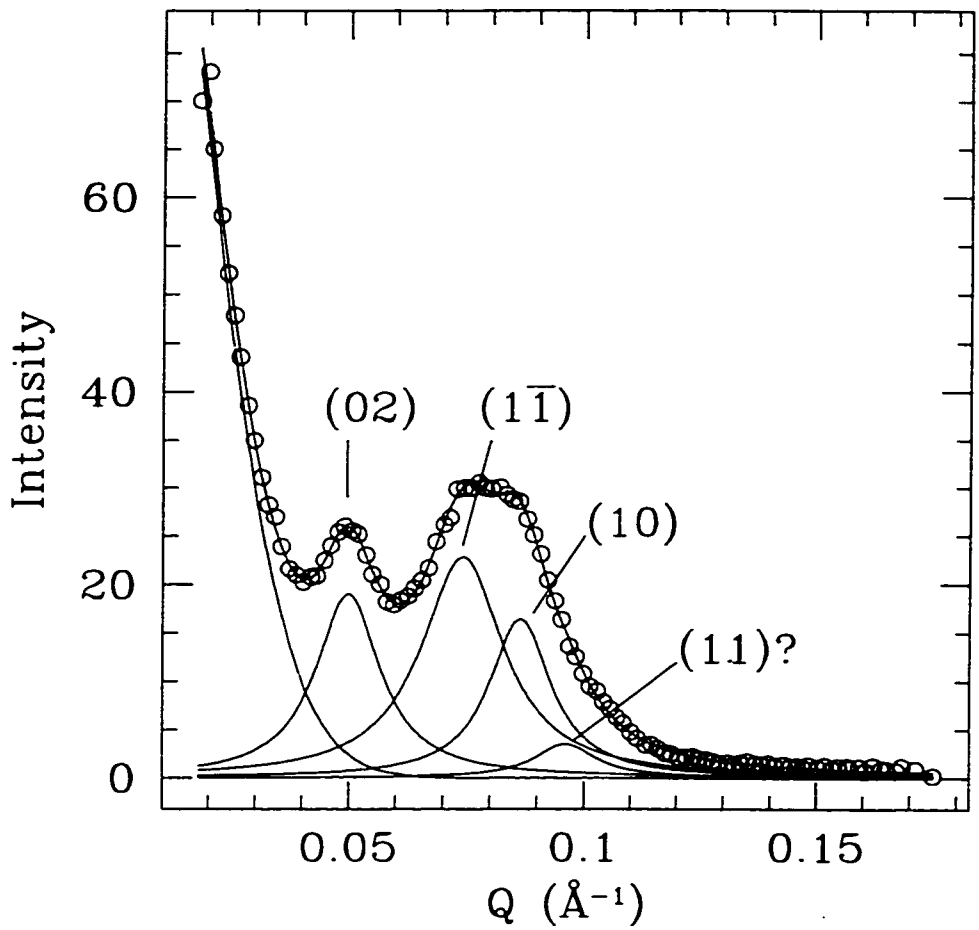

FIG. 9. Fit to the low resolution (3.5 m) neutron data of DPPC-d_9 . The fit consists of a background power law term and four separate Lorentzians. The Lorentzian associated with the (11) peak falls within the tails of the (1$\bar{1}$) and (10) peaks, making it difficult to extract any reliable information about its position.

C. Temperature Dependence of the Ripple Phase

Figure 9 shows a fit to the low resolution (3.5 m) neutron data in the $P_{\beta'}$ phase, cooled from the L_α phase. Consistent with the relevant x-ray data (Fig. 5) where three peaks are resolved, the broad peak in the neutron profile consists of two distinct reflections which we have labeled $(1\bar{1})$ and (10). A fourth peak was necessary in order to match the data in the tail ($Q > 0.95$ Å^{-1}) of the broad feature. This peak likely corresponds to peak 4 in the x-ray data (Fig. 5) although it appears to be centred below its x-ray value of $Q = 0.10$ Å^{-1}. The small amplitude of this peak in the neutron data and its proximity to the strong $(1\bar{1})$ and (10) peaks makes it difficult to extract any reliable information about this peak from the neutron profile. The behaviour of the remaining three peaks, however, can yield useful information as demonstrated in Fig. 10 which traces the (02) and (10) peak positions as a function of temperature through the ripple phase on cooling. The top two panels show the peak position and amplitude, respectively, of the (02) reflection as extracted from fits to the high resolution (8.0 m) neutron data. The bottom panel shows the peak position of the (10) taken from fits to the low resolution (3.5 m) data. It should be noted that the (10) data has been shifted by 1.0 °C along the temperature axis to ensure a match between the transition temperatures for the high resolution and low resolution experiments since it was found that the pre-transition temperature for these two separate experiments differed by this amount.

Equation 2 shows that the change in position of the (02) peak as a function of temperature could be the result of either a temperature dependent ripple wavelength, λ_r, or monoclinicity, γ, or both. Using the measured temperature dependence of the (02) and (10) peaks, we can predict the temperature dependence of the $(1\bar{1})$ peak

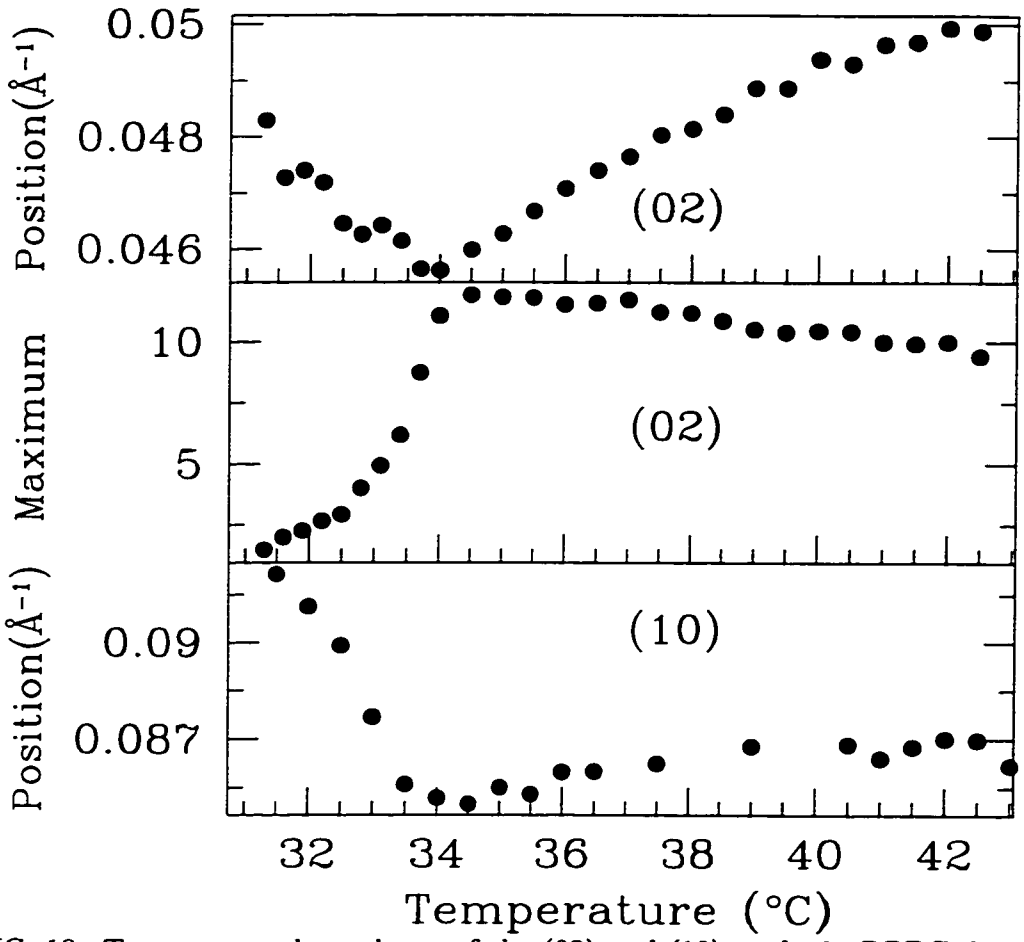

FIG. 10. Temperature dependence of the (02) and (10) peaks in DPPC-d_9 in the $P_{\beta'}$ phase on cooling. The top two panels show the (02) peak position extracted from the high resolution neutron experiment, while the bottom panel shows the peak position of the (10) peak taken from the low resolution neutron experiment. The temperature scale of the low resolution (3.5 m) data has been shifted by 1°C as the pre-transition temperature differed by this amount in the two separate experiments.

under the two possible limiting assumptions (λ varies, γ constant, or γ varies, λ constant) about our unit cell. As can be seen in Fig. 11, a model in which γ is held constant and λ_r varies with temperature is a good description of the observed data, while one in which λ_r is fixed and γ is allowed to vary is not.

As the origin of the temperature dependence of the (02) peak position within the $P_{\beta'}$ phase has been identified as being due to λ_r, it is interesting to compare the thermal expansivity observed in the middle of the ripple phase on cooling, with that typically observed in "hard" materials near room temperature. The thermal expansivity is defined as $\alpha = \frac{1}{a}\frac{da}{dT}$ where a is the appropriate lattice parameter. For the expansivity of the ripples, we obtain a value of $\alpha \sim 0.01$ K^{-1} in the middle of the ripple phase, which is huge compared to expansivities displayed by typical "hard" materials. Near room temperature metallic cesium exhibits the largest α displayed by an element, $\alpha \sim 0.0001$ K^{-1}. This behaviour is anomalously large compared with other elements, due to the fact that cesium melts just above room temperature. The ripple expansivity is sufficiently large that we feel it cannot be due to the anharmonic effects normally ascribed to thermal expansion, but rather to a temperature dependent penetration of the water into the head group region of the rippled bilayer, expanding the ripple structure out within the plane of the bilayer.

D. Stability of the Ripple Phase

Given that two $P_{\beta'}$ phases are clearly observed, one on warming and one on cooling, the question of which one is the equilibrium and which one is metastable remains. On the basis of calorimetric measurements of the enthalpies of the phases, Tenchov *et al.* [5] concluded that the ripple phase on cooling is metastable but long

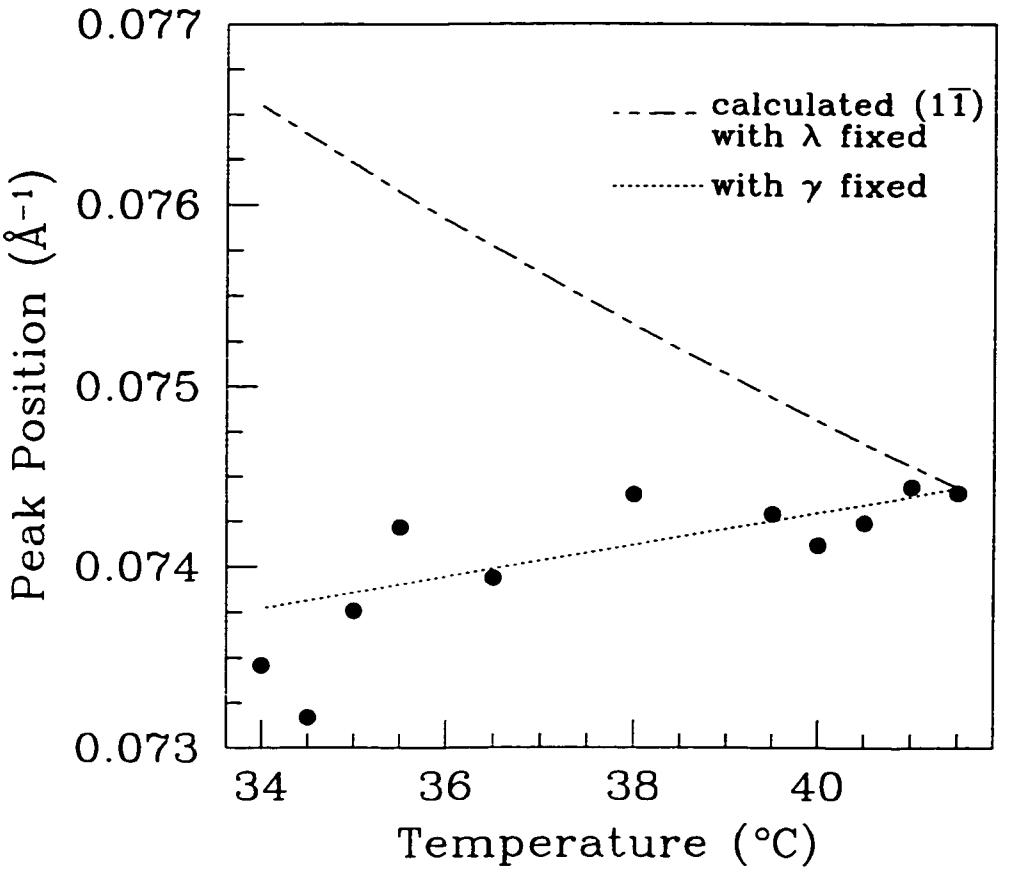

FIG. 11. Temperature dependence of the (1$\bar{1}$) peak in DPPC-d_9 in the $P_{\beta'}$ phase on cooling. The dashed lines indicate the expected temperature dependence of the (1$\bar{1}$) peak using two simple models and the observed temperature dependence of the (10) and (20) peaks. The results clearly show λ_r to be changing with temperature while the monoclinicity remains constant.

lived, and that the $P_{\beta'}$ phase achieved on warming is the true equilibrium phase. This conclusion is premature without entropic information of the two states. There are two features in the comparison between the scattering in the two ripple phases which lead us to believe that the $P_{\beta'}$ phase obtained on cooling is the more ordered phase. First, it displays much less diffuse small angle scattering than does the ripple phase obtained on warming from the $L_{\beta'}$ phase, as is clearly seen in the inset of Fig. 7. Second, the Bragg peaks are sharper in the $L_{\beta'}$ phase obtained on cooling. We therefore conclude that the entropy of $P_{\beta'}$ phase on cooling is less than the entropy of the $P_{\beta'}$ phase on warming. Since our experiments are conducted at constant pressure, it is the Gibbs potential, $G = H - TS$, which is relevant. Denoting the warming and cooling $P_{\beta'}$ phases with the subscripts w and c respectively, we can make now make the following simple thermodynamic argument:

$$S_c < S_w \iff S_w - S_c = \delta S; \quad \delta S > 0$$

$$H_c > H_w \iff H_c - H_w = \delta H; \quad \delta H > 0$$

$$G_c - G_w = (H_c - H_w) + T(S_w - S_c) = \delta H + T\delta S > 0$$

confirming the previous conclusion that the $P_{\beta'}$ phase on cooling is metastable.

We also observe, in agreement with previous measurements [14,15], that the bilayer periodicity exhibits a pronounced temperature dependence, known as anomalous swelling, just above the the $P_{\beta'}$ -L_α transition temperature, T_m (Figs. 2,3). Matuoka *et al.* [16] have shown that the appearance of the multipeak profile in the $P_{\beta'}$ phase requires slow cooling rates through the L_α phase in the vicinity of T_m. It is possible that passage through the anomalous swelling regime, with its strong temperature dependent lamellar repeat distance and concomitant reduction in bilayer

curvature modulus [14], constrains the system to assume the metastable $P_{\beta'}$ structure. The system must pass through this region on cooling into the $P_{\beta'}$ phase from the fluid L_α phase, but not when the $L_{\beta'}$ phase is the temperature precursor.

E. Metastable Gel Phase

The color contour plot of DPPC-d_9 on cooling (Fig. 3) indicates that remnants of the ripple phase persist into the $L_{\beta'}$ phase. One can trace the path of the (02) ripple periodicity peak as it decreases in Q with the approach to the $P_{\beta'}$ to $L_{\beta'}$ transition from above. At the pre-transition temperature, T_p (~34 °C), the (02) ripple periodicity peak merges with the very low Q scattering within the $L_{\beta'}$ phase, suggesting that this scattering originates from remnants of the ripples which are frozen into the $L_{\beta'}$ phase. Explicit evidence for this is seen in Fig. 10 which shows that fits to the scattering profile include a contribution from the ripple structure below T_p and well into the $L_{\beta'}$ phase. Figure 12 depicts the essentials of this argument more clearly. Here we see the marked difference in the warming and cooling scans within the $L_{\beta'}$ phase on both linear and semi-log scales. In addition to the increased scattering at all wavevectors below $Q \sim 0.09$ Å^{-1} in the cooling scan, the lamellar repeat peak is broader and less well-defined than that observed in the warming profile. This indicates the presence of disorder in the bilayer periodicity which is expected as the presence of short range ordered ripple regions in the $L_{\beta'}$ phase is likely to disrupt the bilayer stacking.

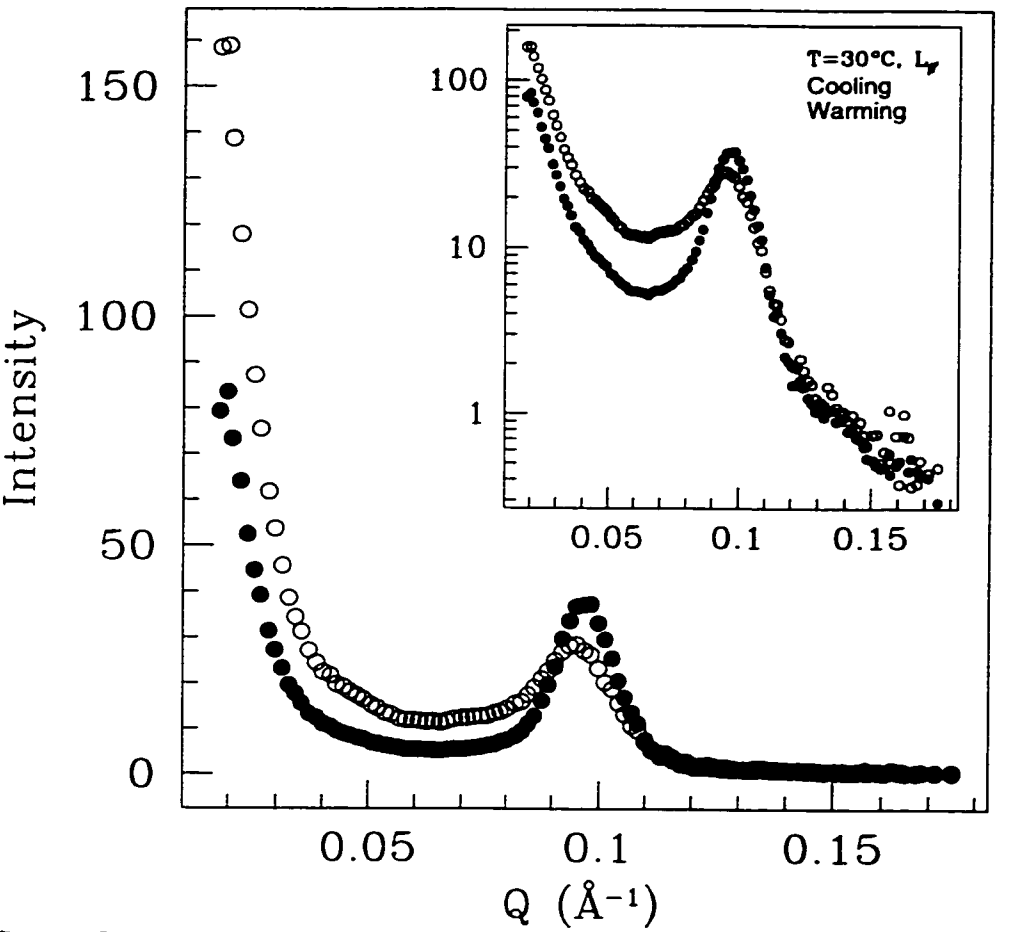

FIG. 12. Comparison of the neutron scattering profiles of DPPC-d_9 in the $L_{\beta'}$ (gel) phase on warming and cooling. The inset shows the same data on a semi-log scale. Both the width of the lamellar repeat peak and the intensity of the small angle ($Q < 0.09$ Å^{-1}) are enhanced in the cooling profile.

IV. CONCLUSION

In conclusion, we have performed complementary neutron and x-ray scattering experiments on MLV samples of DPPC in excess water. Our measurements focused on the ripple, $P_{\beta'}$, phases and we clearly see that different ripple phases form depending on whether the phase is entered from above or below in temperature. The $P_{\beta'}$ structure is much more highly ordered on cooling than on warming, and the diffraction patterns within the ordered $P_{\beta'}$ phase obtained on cooling are well-described using a simple model characterized by a single, long periodicity ripple and large monoclinicity. This model is fully consistent with previous high resolution x-ray data of DPPC in the $P_{\beta'}$ phase on cooling.

The ripple wavelength, λ_r, is found to change dramatically as a function of temperature within this phase, consistent with significant alterations in the degree of penetration or local structure of the water-head group region of the bilayer, as the phase is spanned in temperature. Our data also clearly shows that remnants of the ripple phase persist well past the pre-transition temperature into the $L_{\beta'}$ phase, so that both the $P_{\beta'}$ and $L_{\beta'}$ "solid" phases display pronounced history dependencies.

V. ACKNOWLEDGMENTS

It is a pleasure to acknowledge useful contributions to this work from J. Katsaras. This work was supported in part by the Natural Sciences and Engineering Research Council of Canada, and by the Medical Research Council of Canada under grant number MT-7654. The research at Oak Ridge supported by the Division of Materials Sciences, U.S. Department of Energy under contract No. DE-AC05-960R22464

with Lockheed Martin Energy Research Corporation.

REFERENCES

[1] W.-J. Sun, S. Tristram-Nagle, R.M. Suter, and J.F. Nagle, Proc. Natl. Acad. Sci. USA **93** 7008 (1996).

[2] H.W. Meyer, Biochim. Biophys. Acta **1302** 138 (1996).

[3] J. Katsaras, and V.A. Raghunathan, Phys. Rev. Lett. **74** 2022 (1995).

[4] J. Katsaras, R.F. Epand and R.M. Epand, Phys. Rev. E. **55** 3751 (1997).

[5] B.G. Tenchov, H. Yao, and I. Hatta, Biophys. J. **56** 757 (1989).

[6] H. Yao, S. Matuoka, B. Tenchov, and I. Hatta, Biophys. J. **59** 252 (1991).

[7] W.C. Koehler, Physica (Utrecht). **137B** 320 (1986).

[8] G.D. Wignall, and F.S. Bates, J. Appl. Cryst. **20** 28 (1986).

[9] W.S. Dubner, J.M. Schultz and G.D. Wignall, J. Appl. Cryst. **23**, 469 (1990).

[10] J.A.N. Zasadzinkski, J.Schneir, J. Gurley, V. Ehings, and P.K. Hansma, Science **239**, 953 (1988).

[11] S. Matuoka, S. Kato, and I. Hatta, Biophys. J. **67** 728 (1994).

[12] D.C. Wack, and W.W. Webb, Phys. Rev. A. **40** 2712 (1989).

[13] H.W. Meyer, B. Dobner, and K. Semmler, Chem. Phys. Lipids **82** 179 (1996).

[14] J. Lemmich, K. Mortensen, J.H. Ipsen, T. Honger, R. Bauer, and O.G. Mouritsen, Phys. Rev. E. **53** 5169 (1996).

[15] J.F. Nagle, H.I. Petrache, N. Gouliaev, S. Tristram-Nagle, Y. Liu, R.M. Suter, and K. Gawrisch, Phys. Rev. E. (accepted for publication).

[16] S. Matuoka, H. Yao, S. Kato, and I. Hatta, Biophys. J. **64** 1456 (1993).

Chapter 4

Phase Behaviour of DPPC LUVs

This chapter incorporates the article "Small angle neutron scattering and calorimetric studies of large unilamellar vesicles of the phospholipid DPPC" which, at the time of printing, has been peer-reviewed and accepted for publication in Physical Review E.

Small Angle Neutron Scattering and Calorimetric Studies of Large Unilamellar Vesicles of the Phospholipid DPPC

P.C. Mason and B.D. Gaulin

Department of Physics and Astronomy, McMaster University,

Hamilton, Ontario, L8S 4M1, Canada

R.M. Epand

Department of Biochemistry, McMaster University,

Hamilton, Ontario, L8N 3Z5, Canada

G.D. Wignall and J.S. Lin

Center for Small-Angle Scattering Research, Oak Ridge National Laboratory,

Oak Ridge, Tennessee 37831, USA

Abstract

High resolution differential scanning calorimetry (DSC) and small angle neutron scattering (SANS) experiments have been conducted on large unilamellar vesicles (LUVs) of the phospholipid dipalmitoylphosphatidylcholine (DPPC) in excess water. The DSC results indicate a phase transition at temperatures corresponding to the gel ($L_{\beta'}$) to ripple phase ($P_{\beta'}$) transition seen in multilamellar vesicles of DPPC while the SANS experiments provide direct evidence for the formation of $P_{\beta'}$ phase in these systems. In addition, it is shown that SANS is an effective technique for extracting structural parameters such as vesicle radius and thickness in LUV model membrane systems.

©1998 The American Phyical Society

I. INTRODUCTION

Phospholipids such as dipalmitoylphosphatidylcholine (DPPC) have been the object of intense study due to their unique physical properties, rich phase behavior, and their role as model membrane systems analogous to more complex biological membranes. Large unilamellar vesicles (LUVs) in particular mimic well their counterparts in nature, consisting of a single lipid bilayer forming a closed membrane encapsulating an aqueous core. Characterization of LUV properties such as vesicle radius and bilayer thickness have typically been done using dynamic light scattering [1–4]. While this technique has been and will continue to be an invaluable tool in the study of LUVs, it is important to develop complimentary approaches that may prove useful for elucidating the salient features of LUV systems under a variety of experimental conditions such as, for example, lipid systems with inserted membrane proteins and peptides. Small angle neutron scattering (SANS) is such a technique. In this paper we will show that SANS is sensitive to LUV morphology and present evidence for the existence of the ripple phase in unilamellar vesicles of DPPC.

The ripple, $P_{\beta'}$, phase of DPPC, first discovered by Tardieu *et al.* [5], is a well-studied phase in which the lipid bilayer develops a periodic spatial modulation. Despite this attention, many issues concerning the ripple phase remain unresolved. Several theoretical models of the $P_{\beta'}$ phase propose that the ripple structure is a result of lipid-lipid interactions within the bilayer [6–8]. However, while this phase forms readily in multilamellar vesicles (MLVs) of DPPC, compelling evidence for its formation in LUVs does not exist. Previous differential scanning calorimetry (DSC) studies [9–11] on DPPC LUVs have suggested the existence of the gel, $L_{\beta'}$, to $P_{\beta'}$

transition (known as the pretransition) with evidence of small enthalpy changes at temperatures corresponding to the pretransition temperature in MLVs.

Observations by Fang *et al.* [12] using atomic force microscopy (AFM) show a rippled structure in the upper layer of supported double bilayers of DPPC while regions of the same sample with only a single bilayer covering show no signs of a ripple, supporting theories that bilayer-bilayer interactions may also play an integral part in the formation of a rippled structure [13]. The absence of ripples in domains of single bilayers in the Fang *et al.* [12] study may be the result of suppression of undulations due to the substrate although rippled structures have been observed in single bilayers using AFM both with supported asymmetric unilamellar bilayers [14] (in which the opposing leaflets of the bilayer are composed of different lipids) and with supported unilamellar bilayers of DPPC in the presence of certain chemical compounds [15]. While these studies [12,14,15] should aid in the development of a complete microscopic theory of intra and interbilayer interactions, the relevance to the $P_{\beta'}$ phase in vesicular DPPC remains unclear. We present the results of DSC and SANS experiments on DPPC LUVs which point to the existence of the $P_{\beta'}$ phase in these systems.

II. MATERIALS AND EXPERIMENTAL METHODS

1,2-dipalmitoyl-sn-glycero-3-phosphocholine (DPPC) was purchased from Avanti Polar Lipids, Inc. (Birmingham, AL) and used without any further purification. For the small angle neutron scattering (SANS) experiments, 50 mg of DPPC was suspended in 0.5 mL D_20/PIPES buffer (20 mM PIPES, 1mM EDTA, 150 mM NaCl in D_2O adjusted to a pH meter reading of 7.4). This buffer simulates physio-

logical conditions and has the advantage of avoiding potential experimental artifacts caused by marked changes in pH due to the presence of small amounts of contaminants in an unbuffered solution.

The dispersion was freeze-thawed five times using alternating liquid nitrogen and warm water cycles to promote equilibrium transmembrane distributions of solutes [16]. It is important to avoid transmembrane osmolality variations as such conditions can lead to dramatic differences in vesicle size [3] and morphology [17]. LUV samples were then made by extruding the suspension ten times under nitrogen pressure using a stainless steel extrusion device (Lipex Biomembranes, Inc., Vancouver,B.C.). Each extrusion cycle was performed through two stacked 100 nm pore size polycarbonate filters (Nucleopore Corp., Pleasanton, CA), following the procedure outlined by Hope *et al.* [18]. LUVs prepared in this way are known to be essentially monodisperse [3], almost exclusively unilamellar [18], and extremely stable over periods up to six months [19]. The solution was transfered to a 1 mm pathlength Helma quartz cell designed for SANS experiments on solutions.

The SANS experiments were conducted at the W.C. Koehler 30 m SANS facility at the Oak Ridge National Laboratory [20] using neutrons of wavelength 4.75 Å ($\delta\lambda/\lambda \sim 5\%$). Three configurations of the instrument were employed with sample to detector distances of 1.5 m ($Q = \frac{4\pi}{\lambda}\ sin\ \theta \in [0.035, 0.39\ \text{Å}^{-1}]$ where 2θ is the scattering angle), 3.2 m ($Q \in [0.017, 0.19\ \text{Å}^{-1}]$), and 18.0 m ($Q \in$[0.003, 0.03 Å^{-1}]), for relatively low, medium, and high resolution measurements, respectively. The SANS data were corrected for instrumental backgrounds and detector efficiency and converted into absolute differential cross sections per unit sample volume using established protocols [21,22].

Samples for the DSC were prepared by suspending 10.0 mg of DPPC in 10.0

mL of PIPES buffer and following the LUV preparation procedure outlined above. Measurements were made using a Nano Differential Scanning Calorimeter (Calorimetry Sciences Corporation, Provo, UT). The features of the design of this instrument have been previously described [23]. Solutions were degassed under vacuum prior to loading in the calorimeter cells.

III. RESULTS AND DISCUSSION

A. Differential Scanning Calorimetry

Reported enthalpy changes at the pretransition vary greatly depending on the LUV preparation method, vesicle size, and buffer solution [9–11]. We have conducted DSC experiments on LUVs of DPPC at various scan rates. The results of two different scan rates are displayed in Fig. 1 with the top panel showing data collected at 0.75 °C/min and the bottom data collected at 2.00 °C/min. The solid lines represent fits to the data consisting of a linear background term, a Lorentzian centered at the pretransition temperature, and an inverse power law which describes the low temperature side of the main transition peak. The fits are cut off just below the main transition temperature as the asymmetry in the main transition peak complicated the analysis without adding to the interpretation. The insets show the data with the background and the contribution of the main transition (the inverse power law) subtracted, along with the Lorentzian contribution to the fit. In both cases there is clear evidence for the pretransition with enthalpy changes far in excess of what would be expected even if there was an improbably high amount of multilamellar contamination in the samples. The results of these experiments are summarized in Table I, along with the results of an experiment performed for comparative purposes on a

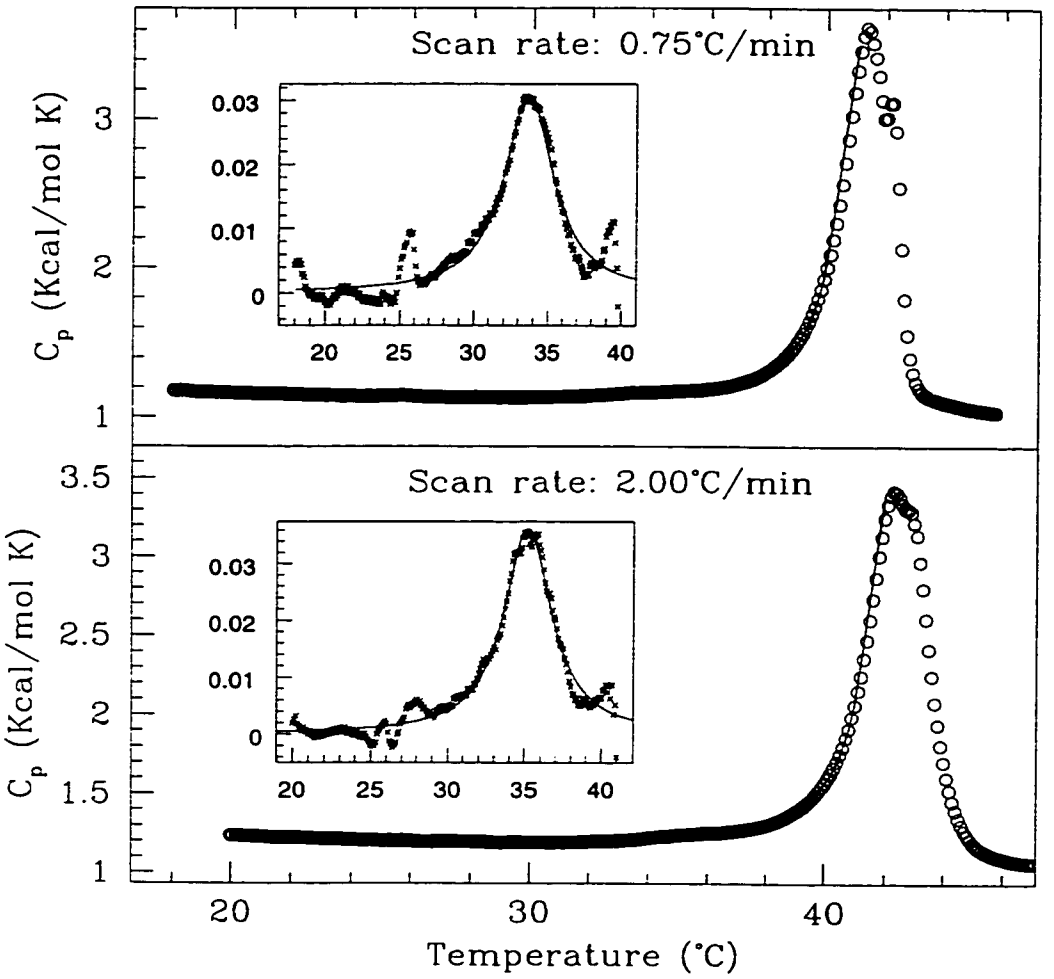

FIG. 1. DSC results at two different scan rates on DPPC LUVs. The solid line is a fit to the data. As described in the text, the insets show the difference between the data and the sum of the background and contribution of the main transition peak at $T \sim 42°C$. The solid line in the insets is the Lorentian component of the fit to the data sets. Both scan rates give clear indication of the pretransition. The results of quantitative analysis of the measurements are listed in Table I.

TABLE I. DSC results for DPPC LUVs at two different scan rates and MLVs at a scan rate of 0.75 °C/min. The results presented are from scans as the sample was warmed. The subscripts p and m refer to the pretransition and main transition respectively.

Sample type	Scan Rate (°C/min)	T_p (°C)	ΔH_p (Kcal/mol)	T_m (°C)	ΔH_m (Kcal/mol)	$\frac{\Delta H_p}{\Delta H_m}$ (x100%)
LUV	0.75	33.7	0.16	41.3	7.0	2.3
	2.00	35.2	0.18	42.3	7.2	2.5
MLV	0.75	36.0	1.1	42.0	7.4	15

DPPC MLV sample in the same environment. The enthalpy changes and transition temperatures for the MLV sample agree well with known values [24] while the LUV enthalpies are on the low end of the range of those reported in the literature.

B. Small Angle Neutron Scattering

Based on previous results on egg PC [18,25,26], prepared using similar techniques as our own, we expect our LUV samples to be monodisperse, unilamellar, spherical vesicles. From a scattering standpoint, such samples in low concentration should be easily modeled as hollow, non-interacting spheres for which the scattering function is simply the difference between the Fourier transforms of concentric spheres. This can be written analytically as:

$$S(Q) = A\left[(R+d)^3 \frac{sin(Q(R+d)) - Q(R+d)cos(Q(R+d))}{(Q(R+d))^3} - R^3 \frac{sin(QR) - QRcos(QR)}{(QR)^3}\right]^2 \quad (1)$$

where A is an overall amplitude of the scattering, R is the radius of the LUV, and d is the thickness of the bilayer. The radius is a measure of the membrane curvature which

is an important parameter in membrane elasticity theories (see, for example, [27–33]) and is thought to influence such properties as transbilayer lipid transport processes [34], while the bilayer thickness plays an integral role in modulating the function of transmembrane proteins among other properties [35]. The scattering function given in Eq. 1 can be expanded in terms of products of periodic functions and shown to consist of a rapidly oscillating term with a period of $2\pi/R$ within an envelope of much more slowly varying oscillations of period $2\pi/d$. Thus, we expect that we should be able to extract these membrane parameters from scattering data taken over a sufficiently broad range in Q-space.

In our SANS experiments, the scattering events actually measured are a convolution of the true scattering function of the system with the appropriate resolution function of the instrumentation:

$$I(Q) = \int_{Q'} S(Q') \cdot R(Q - Q')\, dQ' \tag{2}$$

where $S(Q')$ is the scattering function given in Eq. 1 and $R(Q-Q')$ is the instrumental resolution function centered at Q. A short discussion of resolution function appears in the appendix. Since the SANS intensities are converted to absolute differential cross sections per unit sample volume and the Q-ranges from the three different resolution configurations overlap, we are able to assemble the data into a single scattering curve, as shown in Fig. 2 which extends over four and a half decades in measured intensity and almost two decades in Q. The data shown in Fig. 2 were collected at 20 °C which corresponds to the gel, $L_{\beta'}$, phase of DPPC. The best fit to the data, using Eq. 2 and a Gaussian resolution function, was obtained using a non-linear least squares fitting routine and is shown as the solid line in the figure. The unconvoluted fit appears as the dotted line.

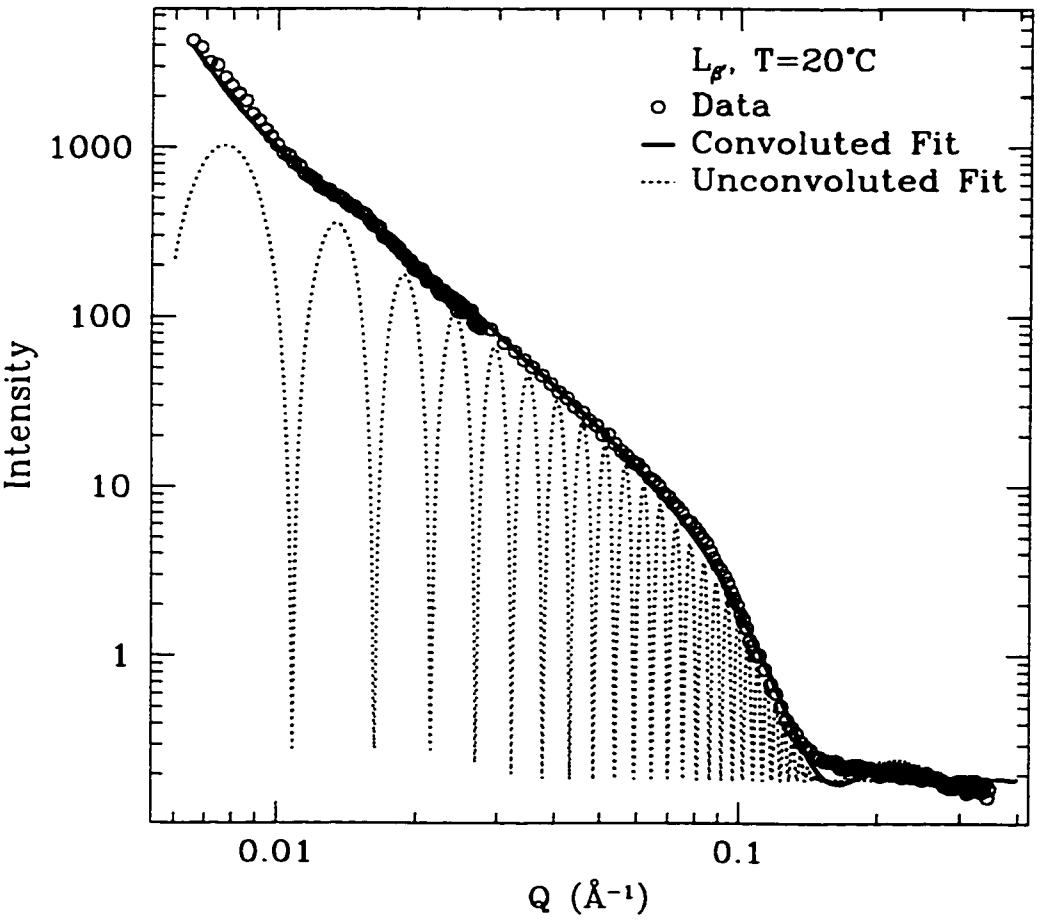

FIG. 2. Fit to the scattering profiles of DPPC LUVs at 20°C, as described in the text.

Inspection of Fig. 2 shows that the fit using Eq. 2 under the assumption of a sample of monodisperse, noninteracting, hollow spheres is a good description of the data. The fit describes the data over four decades in intensity and over one and a half decades in Q, yielding a membrane radius of $R = 570$ Å and thickness $d = 38.4$ Å. Deviations from the fit are seen at small values (< 0.01 Å^{-1}) of Q, where the fit falls below the actual scattering. We speculate that this is due to intervesicular contributions to the scattering.

The fit also fails to describe the data well at the major distinguishing feature seen in the data in Fig. 2– the shoulder at ~ 0.1 Å^{-1}. The instrumental resolution function smears the data in much the same way as would a polydisperse sample centered about a mean radius and it was found that increasing the width of the instrumental resolution function, $R(Q - Q')$, did not improve the fit in this region. Therefore, it is unlikely that polydispersity would affect the goodness of the fit. The discrepancy cannot be explained by assuming a scattering contribution from a bilayer periodicity which would occur if there was a small multilamellar component to our samples as such scattering would be apparent in the subtractions of the data sets shown later in this paper. There have been reports of non-spherical LUVs in an isoosmotic environment similar to ours [17]. Deviations from a spherical form could affect our scattering pattern in such a way that it cannot be fully described by the simple form given in Eq. 1. However, given the good overall description of the data over such a wide range of Q and intensity, it is unlikely we are seeing dramatic shape fluctuations such as those described, for example, by Mui *et al.* [17].

While the membrane radius, R, taken from our fit falls within accepted values for LUVs produced by extrusion [1], the the membrane thickness, d, falls below established values [35,36]. This is not surprising since the location of the shoulder in

the SANS profile ($Q \sim 0.1$ Å^{-1}) gives a measure of d and this is the precisely where our fit fails to adequately describe the data in detail. The top panel of Fig. 3 shows medium resolution data at temperatures corresponding to the gel ($L_{\beta'}$,T=20 °C) ripple ($P_{\beta'}$,T=37 °C), and liquid crystalline (L_α,T=50 °C) phases, highlighting the region in which the shoulder seen in Fig. 2 occurs. In this region of Q space, there is no discernible difference between the data sets collected at 20 °C and 37 °C which is expected even if the sample is in the $P_{\beta'}$ phase at 37 °C since both the $L_{\beta'}$ and $P_{\beta'}$ phases are gel phases with the acyl chains largely as trans rotomers. Thus, a change in membrane thickness and subsequent shift in the shoulder feature would be surprising. In the L_α phase at T=50 °C, the rotational isomerism associated with the melting of the acyl chains leads to a decrease in membrane thickness, pushing the shoulder out to a higher value of Q as is clearly seen in the figure.

The shoulder in the data is a region of local maximum curvature of the plot and will therefore correspond to a local minimum in the second derivative. The bottom panel of Fig. 3 shows the 2nd derivative of the three data sets, along with lines marking the location of the local minimum. The shift in the minimum for the L_α phase data clearly corresponds to the shift in the location of the shoulder in the data. We can do the same derivative analysis with the convoluted theoretical scattering function by varying the two membrane parameters systematically, generating the scattering curve numerically, convoluting with the resolution function, and finding the location of the second derivative minimum for each set of input parameters. Repeating this procedure for a wide range of parameters allows us to generate a series of "calibration curves" which relate the position of maximum curvature, the shoulder, to the membrane thickness, d, for a given value of the vesicle radius, R.

Using values for the vesicle radii extracted from fits to the joined data over

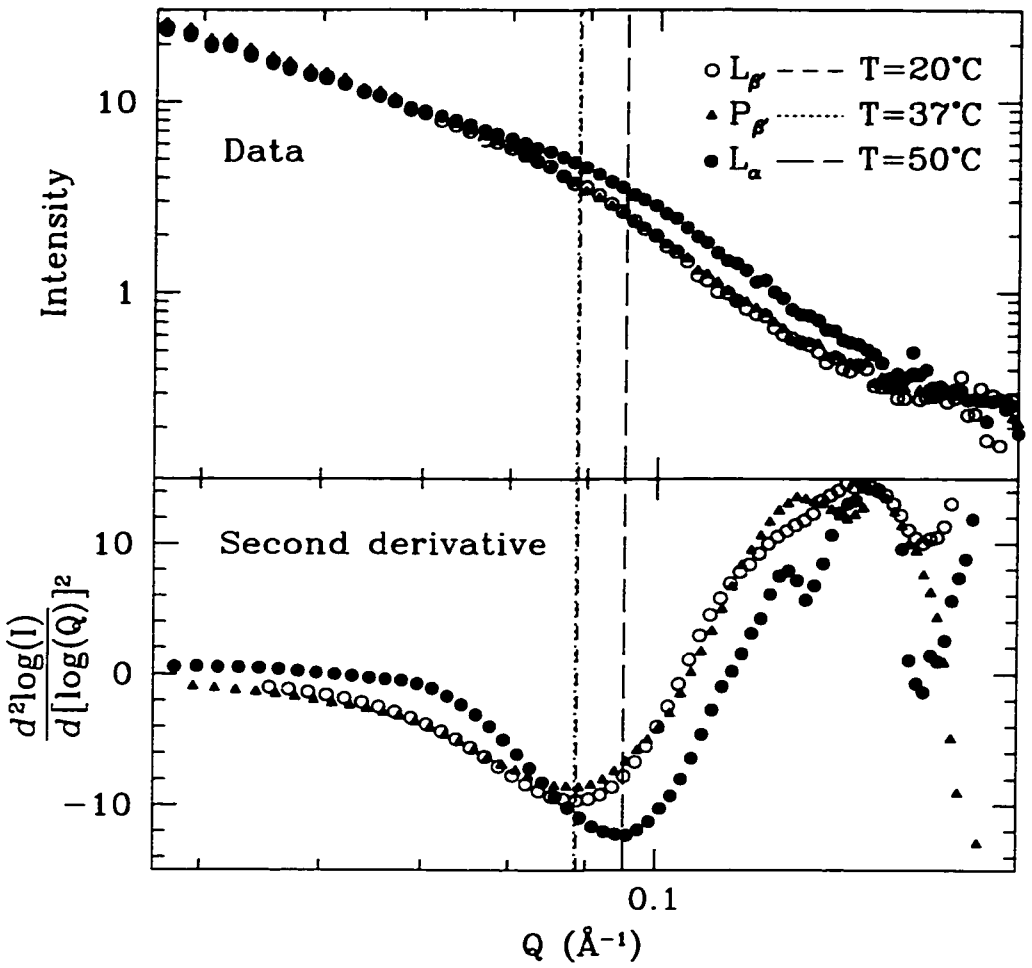

FIG. 3. Results of medium resolution SANS LUV experiments: the top panel shows data collected at temperatures corresponding to the $L_{\beta'}$,$P_{\beta'}$, and L_α phases while the bottom panel shows the curvature in the data. The vertical lines indicated positions of maximum curvature.

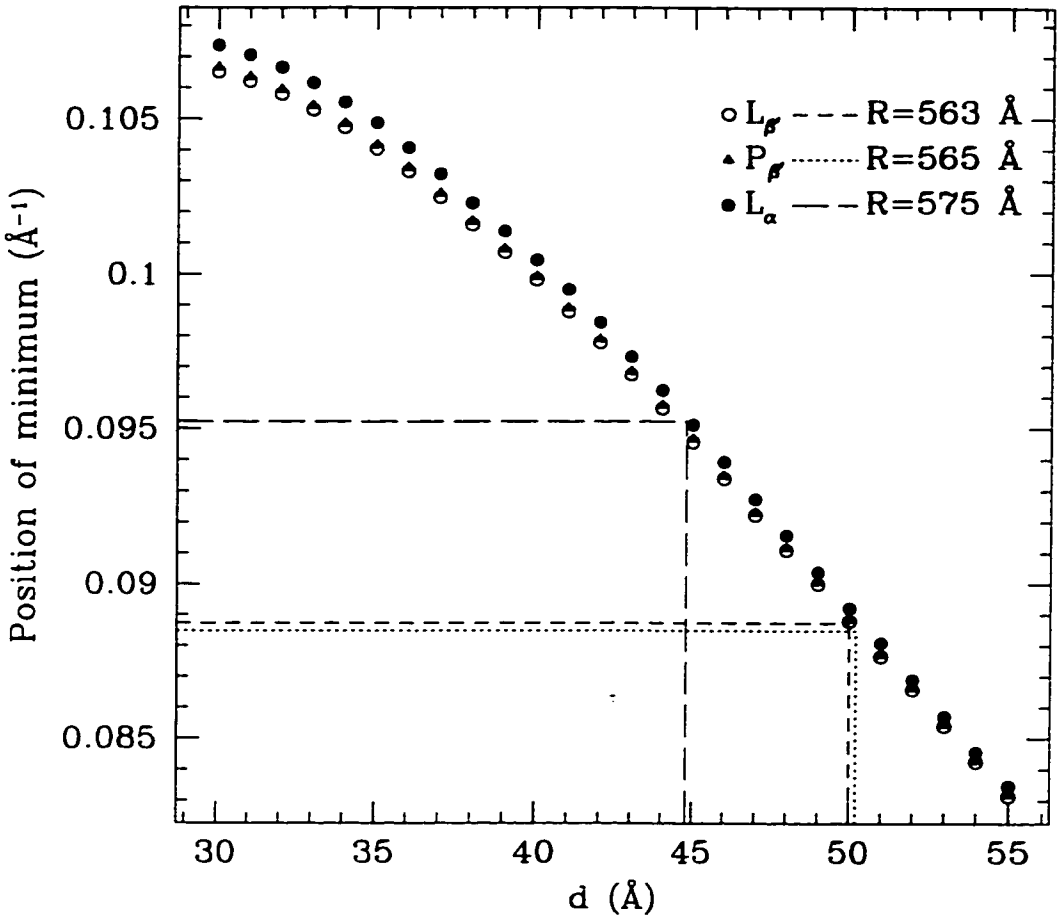

FIG. 4. Calibration curves relating the position of the minimum in the second derivative of the convoluted theoretical scattering function (Eq. 2) to the membrane thickness, d, as it appears in Eq. 1. The dashed lines correspond to minimums in the second derivative of the SANS data, taken from Fig. 4, which are used to extract an accurate estimate of d in each phase.

TABLE II. Vesicle parameters as determined by SANS analysis. The first column of vesicle thickness, d, values were extracted from fits to the data, while the second were determined by derivative analysis and are the accurate absolute measure of d. R is the vesicle radius.

Temp.(°C), phase	R (Å)	$d_{fit} \pm 0.4$ (Å)	$d_{deriv} \pm 2$ (Å)
20, $L_{\beta'}$	563 ± 12	39.6	50
37, $P_{\beta'}$	565 ± 12	39.3	50
50, L_{α}	575 ± 12	35.5	45

the three different resolutions such as that shown in Fig. 2, a calibration curve of shoulder position versus membrane thickness was generated, as shown in Fig. 4, for each of the three temperatures measured. Horizontal lines from the three Q values corresponding to maximum curvature taken from the data in Fig. 3 are shown in Fig. 4. These lines intercept their corresponding calibration curves at which point a line can be dropped to the abscissa, yielding a value for the membrane thickness, d, for each temperature. The results of this analysis yield $d_{L_\alpha} = 45 \pm 2$Å, $d_{P_{\beta'}} = 50 \pm 2$Å, and $d_{L_{\beta'}} = 50 \pm 2$Å. It is these values of the membrane thickness, well within the range of accepted values [36], that we believe accurately represent the information provided by our SANS data. Uncertainties on these values are estimated by varying R in the theoretical fits to the point that they no longer describe the data well. A membrane thickness based on these limiting values of R is considered to be a fair indication of the uncertainty in d. The results of the fitting and derivative analysis are summarized in Table II. While the results of the two analyses differ significantly in their absolute values for the membrane thickness, it is interesting to note that both are consistent in showing that d does not change (within uncertainty) in going from

20 °C to 37 °C , while it decreases by $\sim$ 12% in the L_α phase, in agreement with measurements using other techniques.

As evidenced by Fig. 2, resolution limited measurements of the scattering function given by Eq. 2 show relatively few features. The shoulder in the data at $Q \sim 0.1$ Å^{-1}, discussed above, corresponds to the slowly varying oscillations of period $2\pi/d$. At small Q, the more rapid $2\pi/R$ oscillations can be probed. The upturn in the data at $Q \sim 0.012$ Å^{-1} will give a measure of these high-frequency oscillations. From the results given in Table II, using fitting routines to determine the vesicle radius gives nearly identical values for R at 20 °C and 37 °C. While the fits are not particularly sensitive to small changes in R, subtractions of the data should highlight any differences present in the sample due to the change in temperature. A shift in R should result in an observable difference between the data sets at small Q, on the order of $\frac{2\pi}{R} \sim \frac{2\pi}{500} = 0.0125$ Å^{-1}. The top panel of Fig. 5 shows high resolution data taken at temperatures corresponding to the $L_{\beta'}$ and $P_{\beta'}$ phases. The middle panel shows a subtraction of the data sets in the top panel, which peaks at $Q \sim 0.013$ Å^{-1}. The bottom panel of Fig. 5 shows subtractions of the remaining two data sets. The $P_{\beta'}$ set minus the L_α set peaks at $Q \sim 0.012$ Å^{-1}while the $L_{\beta'}$ minus the L_α peaks weakly at $Q \sim 0.011$ Å^{-1}. Thus, while the fitted values of the vesicle radius given in Table II are indistinguishable within error, the data subtractions clearly show sensitivity to relative shifts in R in each of the three phases.

Similar subtractions of the medium resolution data are shown in Fig. 6. It is very interesting to note that the subtraction of the $L_{\beta'}$ phase data from the data collected at T=37 °C shows a 5% difference in the scattering peaking at $Q \sim$ 0.055 Å^{-1}. The subtraction of the L_α data from the T=37 °C (bottom panel) also peaks at this same wavevector, whereas the subtraction of the L_α phase from the $L_{\beta'}$

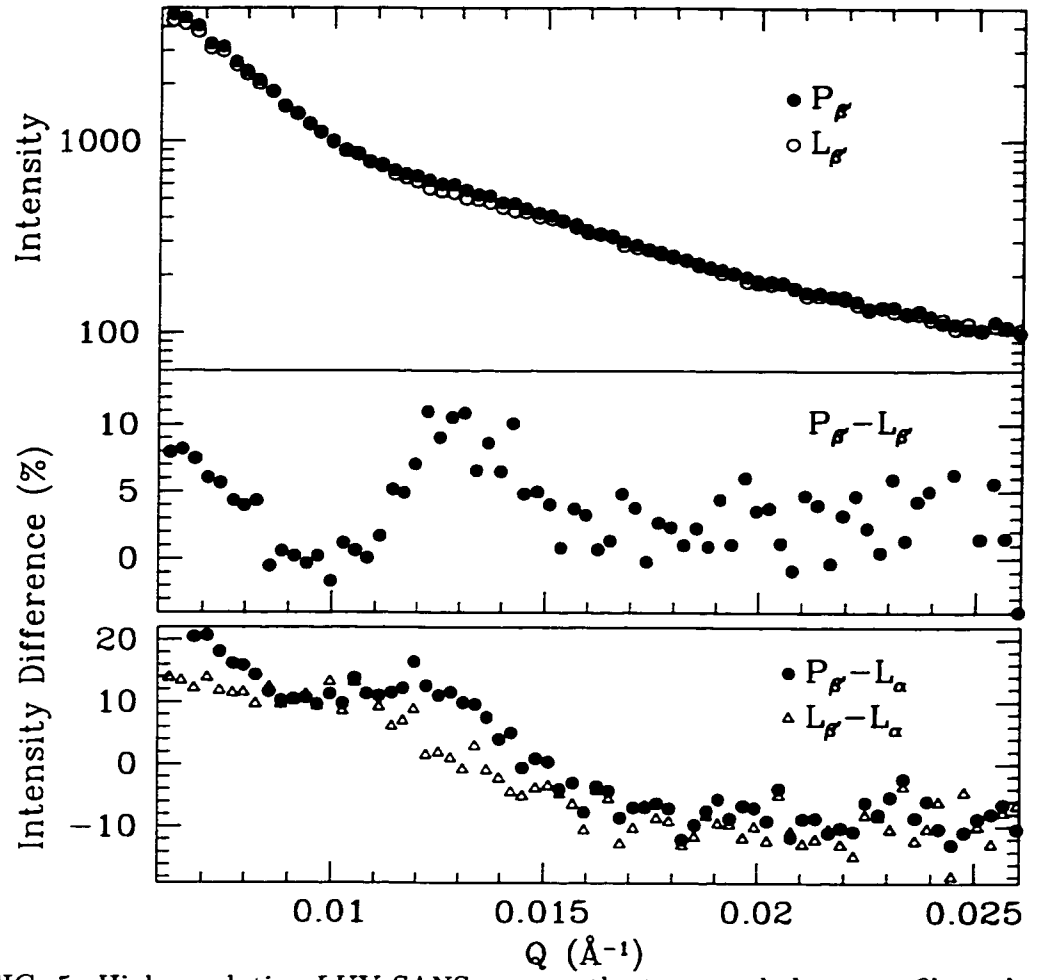

FIG. 5. High resolution LUV SANS curves: the top panel shows profiles taken in the $P_{\beta'}$ and $L_{\beta'}$ phases with the difference in the curves appearing below; the bottom panel shows the difference between scattering in the L_{α} phase and in the $P_{\beta'}$ and $L_{\beta'}$ phases respectively.

phase shows a negligible difference in scattering at this value of Q. The peak in the intensity differences at $Q \sim 0.055$ Å^{-1} cannot be explained by differences in either vesicle radius or thickness. It can be explained, however, by assuming the development of a ripple structure of wavelength $\lambda_r \sim 115$ Å in the membrane, direct evidence that the $P_{\beta'}$ phase does indeed form in LUVs of DPPC. If the difference in the data sets is done as a straight subtraction (not shown) as opposed to a percentage difference, one finds that the expected ripple wavelength shifts up slightly giving $\lambda_r \sim 125$ Å. Both of these values for λ_r fall within accepted values for the ripple wavelength for the $P_{\beta'}$ phase seen in DPPC MLVs [38–40]. The large dip in the intensity difference at $Q \sim 0.11$ Å^{-1} seen in the bottom panel of Fig. 6 is due to the shift in the shoulder position L_α phase (*cf.* Fig. 3) and gives a measure of the order of d. Note that none of the subtractions give evidence for a multilamellar component to our LUVs, as such contamination would yield peaks in the range 0.08 Å$^{-1} < Q < 0.10$ Å^{-1}.

It is not surprising that the ripple feature of the LUV $P_{\beta'}$ phase should be difficult to see with diffraction. In MLVs , the rippling of the membrane surface occurs in each bilayer of the stacked bilayer construct, forming coherently between bilayers creating a three dimensional, monoclinic lattice readily apparent in scattering experiments [40]. In LUVs, ripples in the solitary bilayer of each vesicle will contribute incoherently to the scattering in contrast to the coherent contribution to the scattering from multiple rippled bilayers in each MLV. Therefore, the 5% increase in scattering at the ripple wavevector in LUVs in the $P_{\beta'}$ phase, while small compared to increase seen in MLVs, should not be interpreted as the result of incomplete formation of this phase in LUVs, but rather as a natural suppression of similar scattering seen in MLV systems.

It is interesting to note that we see very little change in vesicle size in going

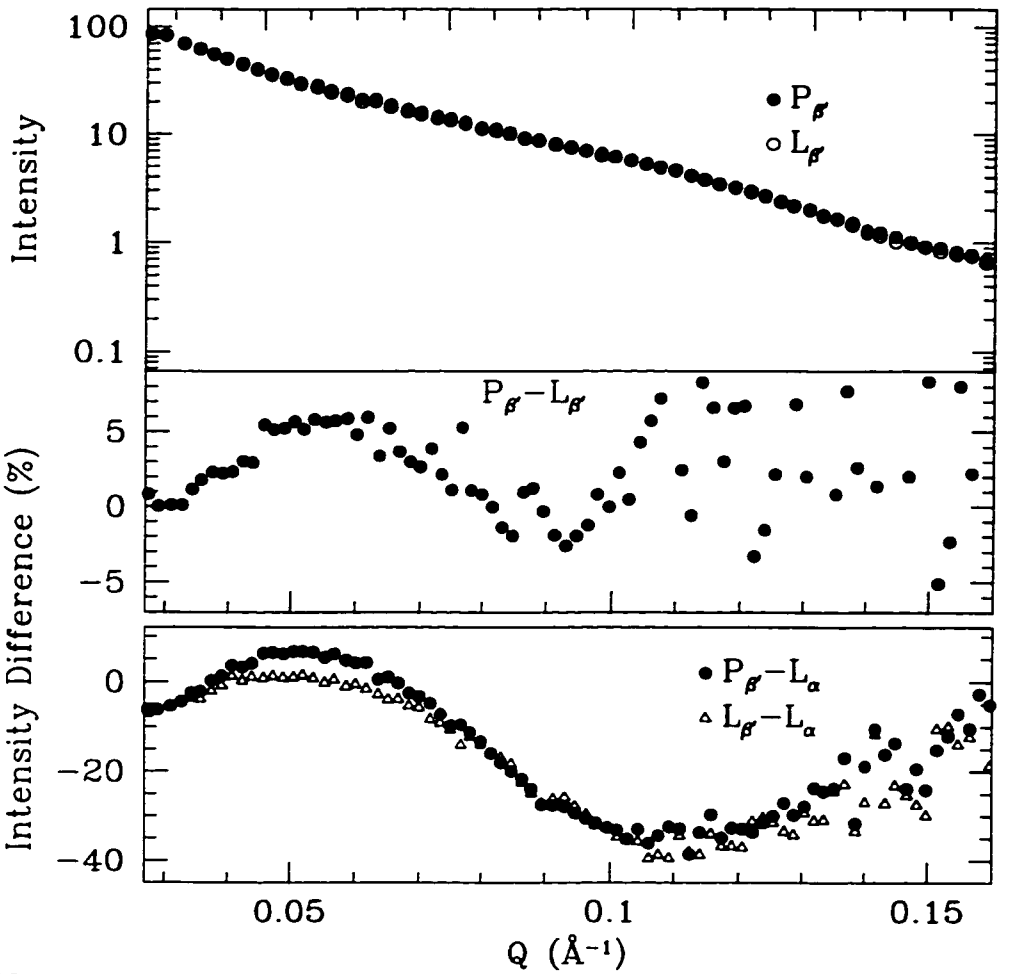

FIG. 6. Medium resolution LUV SANS curves: the top panel shows profiles taken in the $P_{\beta'}$ and $L_{\beta'}$ phases with the difference in the curves appearing below; the bottom panel shows the difference between scattering in the L_{α} phase and in the $P_{\beta'}$ and $L_{\beta'}$ phases respectively.

from the $L_{\beta'}$ to the $P_{\beta'}$ phase, contrary to what is seen in MLV systems [37]. There have been reports [41] of marked decreases (as high as 28%) in MLV radius upon entry into the $P_{\beta'}$ phase. We would be sensitive to such changes if they were occurring in our LUV system, suggesting that bilayer-bilayer interactions may play a role in these changes in MLVs.

IV. CONCLUSION

In summary, we show high resolution differential scanning calorimetry results indicating a small excess heat capacity in DPPC large unilamellar systems at a temperature where the gel to ripple phase transition is expected in MLV systems. Complimentary small angle neutron scattering experiments were performed on identically prepared large unilamellar vesicles of DPPC at three different temperatures, corresponding to the $L_{\beta'}$, $P_{\beta'}$, and L_{α} phases, at three different instrumental resolutions. We have shown that our samples are well modeled by monodisperse, unilamellar, non-interacting, hollow spheres and extract reasonable values for both the vesicle radius and membrane thickness from our analysis. We present, for the first time, diffraction evidence for the existence of the $P_{\beta'}$ phase in DPPC LUVs with a ripple wavelength of the same order as seen in MLV systems.

V. ACKNOWLEDGMENTS

The authors would like to thank R.F. Epand for helpful discussions about the DSC work. This work was supported in part by the Natural Sciences and Engineering Research Council of Canada, and by the Medical Research Council of Canada under grant number MT-7654. The research at Oak Ridge supported by the Division of Ma-

terials Sciences, U.S. Department of Energy under contract No. DE-AC05-960R22464 with Lockheed Martin Energy Research Corporation.

APPENDIX A: DISCUSSION OF THE RESOLUTION/CONVOLUTION

The choice of resolution function was not critical as the rapid oscillations in S(Q) (see Eq. 1 and Fig. 2) will smear out quickly for any reasonable (finite) choice of instrumental resolution, especially in the medium and low resolution configurations. A Gaussian function was chosen since it is simple to model and it has been shown to be a good descriptor of the resolution function for SANS instruments such as those at ORNL [42]. The widths of the resolution function at sample-to-detector distances of 1.5 m, 3.2 m, and 18.0 m were 0.024 $Å^{-1}$, 0.015 $Å^{-1}$, and 0.0065 $Å^{-1}$ respectively based on measurements of widths from resolution-limited Bragg peaks seen in an experiment on multilamellar vesicles of DPPC in the solid $L_{\beta'}$ and $P_{\beta'}$ phases under identical experimental conditions [40,43]. At the boundaries between the data sets care was taken to ensure that the convoluted fit function remained continuous. The parameters extracted from the fits were robust with respect to small variations of the resolution function in all three instrumental configurations.

REFERENCES

[1] D.G. Hunter, and B.J. Frisken, Biophys. J. **74** 2996 (1998).

[2] F.R. Hallett, J. Watton, and P.H. Krygsman, Biophys. J. **59** 357 (1991).

[3] G. White, J. Pencer, B.G. Nickel, J.M. Wood, and F.R. Hallett, Biophys. J. **71** 2701 (1996).

[4] A. Ertel, A.G. Marangoni, J. Marsh, F.R. Hallett, and J.M. Wood, Biophys. J. **64** 426 (1993).

[5] A. Tardieu, V. Luzzati, and F.C. Reman, J. Mol. Biol. **75** 711 (1973).

[6] S. Doniach, J. Chem. Phys **70** 4587 (1979).

[7] T.C. Lubensky, and F.C. MacKintosh, Phys. Rev. Lett **71** 1565 (1993).

[8] J.M. Carlson, and J.P. Sethna, Phys. Rev. A **36** 3359 (1987).

[9] R. Parente, and B. Lentz, Biochemistry **23** 2353 (1984).

[10] R. Parente, M. Hochli, and B. Lentz, Biochim. Biophy. Acta. **812** 493 (1985).

[11] D. Lichtenberg, M. Menashe, S. Donaldson, and R. Biltonen, Lipids **19** 395 (1984).

[12] Y. Fang, and J. Yang, J. Phys. Chem. **100** 15614 (1996).

[13] G. Cevc, B. Zeks, and R. Podgornik, Chem. Phys. Lett **84** 209 (1981).

[14] D.M. Czajkowsky, C. Huang, and Z. Shao, Biochemistry **34** 12501 (1995).

[15] J. Mou, J. Yang, and Z. Shao, Biochemistry **33** 4439 (1994).

[16] L.D. Mayer, M.J. Hope, P.R. Cullis, and A.S. Janoff, Biochim. Biophys. Acta.

817 193 (1985).

[17] B.L.-S. Mui, P.R. Cullis, E.A. Evans, and T.D. Madden, Biophys. J. **64** 443 (1993).

[18] M.J. Hope, M.B. Bally, G. Webb, and P.R. Cullis, Biochim. Biophys. Acta. **812** 55 (1985).

[19] H. Nagano, H. Yao, and K. Ema, Phys. Rev. E. **51** 3363 (1995).

[20] W.C. Koehler, Physica (Utrecht) **137B** 320 (1986).

[21] G.D. Wignall, and F.S. Bates, J. Appl. Cryst. **20** 28 (1986).

[22] W.S. Dubner, J.M. Schultz and G.D. Wignall, J. Appl. Cryst. **23**, 469 (1990).

[23] G. Privalov, V. Kavina, E. Freire, and P.L. Privalov, Analytical Biochem. **232** 79 (1995).

[24] S.C. Chen, J.M. Sturtevant, and B.J. Gaffney, Proc. Natl. Acad. Sci. U.S.A. **77** 5060 (1980).

[25] R. Nayer, M.J. Hope, and P.R. Cullis, Biochim. Biophys. Acta. **986** 200 (1989).

[26] L.D. Mayer, M.J. Hope, and P.R. Cullis, Biochim. Biophys. Acta. **858** 161 (1986).

[27] W. Helfrich, Z. Naturforsch **28c** 693 (1973).

[28] E.A. Evans, Biophys. J. **30** 265 (1980).

[29] U. Seifert, K. Berndl, and R. Lipowsky, Phys. Rev. A. **44** 1182 (1991).

[30] U. Seifert, Phys. Rev. Lett. **70** 1335 (1993).

[31] L. Miao, B. Fourcade, M. Rao, M. Wortis, and R.K.P. Zia, Phys. Rev. A. **43**

6843 (1991).

[32] L. Miao, U. Seifert, M. Wortis, H.-G. Döbereiner, Phys. Rev. E. **49** 5389 (1991).

[33] S. Svetina, and B. Žekš, Eur. Biophys. J. **17** 101 (1989).

[34] B.L.-S Mui, H.-G. Döbereiner, T.D. Madden, and P.R. Cullis, Biophys. J. **69** 930 (1995).

[35] B.A. Lewis, and D.M. Engelman, J. Mol. Biol. **166** 211 (1983).

[36] Y. Inoko, and T. Mitsui, J. Phys. Soc. Japan, **44** 1918 (1978).

[37] E. Evans, and R. Kwok, Biochemistry **21** 4874 (1982).

[38] H. Yao, S. Matuoka, B. Tenchov, and I. Hatta, Biophys. J. **59** 252 (1991).

[39] J.A.N. Zasadzinkski, J.Schneir, J. Gurley, V. Ehings, and P.K. Hansma, Science **239**, 953 (1988).

[40] P.C. Mason, B.D. Gaulin, R.M. Epand, G.D. Wignall, and J.S. Lin Phys. Rev. E (accepted for publication).

[41] R.P. Perkins, X. Li, J.L. Slater, P.A. Harmon, P.L. Ahl, S.R. Minchey, S.M. Gruner, and A.S. Janoff, Biochim. Biophys. Acta. **1327** 41 (1997).

[42] J.S. Pedersen, D. Posselt, and K. Mortensen, J. Appl. Cryst. **23** 321 (1990).

[43] P.C. Mason, B.D. Gaulin, R.M. Epand, G.D. Wignall, and J.S. Lin (unpublished).

Chapter 5

Interfacial Morphologies of DPPC and POPE

This chapter incorporates the article "Interfacial morphologies of the phospholipids DPPC and POPE in excess water using small angle neutron scattering" which was submitted for publication in Physical Review E on November 17, 1998.

Interfacial Morphologies of the Phospholipids DPPC and POPE in Excess Water Using Small Angle Neutron Scattering

P.C. Mason and B.D. Gaulin

Department of Physics and Astronomy, McMaster University,

Hamilton, Ontario, L8S 4M1, Canada

R.M. Epand

Department of Biochemistry, McMaster University,

Hamilton, Ontario, L8N 3Z5, Canada

G.D. Wignall and J.S. Lin

Center for Small-Angle Scattering Research, Oak Ridge National Laboratory,

Oak Ridge, Tennessee 37831, USA

Abstract

Small angle neutron scattering (SANS) experiments have been performed on samples of the phospholipids dipalmitoylphosphatidylcholine (DPPC), DPPC in which the quaternary ammonium methyl hydrogens have been replaced with deuterium (DPPC-d_9), and 1-palmitoyl-2-oleoylphosphatidylethanolomine (POPE) at four different temperatures and in excess water. In the low angle region, below the lamellar repeat Bragg peak, the scattering profiles exhibit power law behavior over a decade in scattering angle. Fits to these profiles indicate that POPE at all temperatures and the DPPC samples in the liquid crystalline (L_α) phase are well described

by the Porod law for smooth interfaces. Scattering from the DPPC samples in their solid gel ($L_{\beta'}$) and ripple ($P_{\beta'}$) phases is consistent with a fractal surface indicating a rough interface between the DPPC headgroups and the water at these temperatures.

©1998 The American Phyical Society

I. INTRODUCTION

Model membranes systems, such as those composed of homogeneous suspensions of phospholipids dipalmitoylphosphatidylcholine (DPPC) and 1-palmitoyl-2-cleoylphosphatidylethanolomine (POPE), have been studied extensively to give insight into the properties of biological membranes. DPPC, the most widely studied of the phospholipids, consists of a hydrophilic choline headgroup attached through a phosphate to a glycerol backbone to which are esterified two identical acyl chains, sixteen carbons in length. POPE, another common membrane phospholipid, has an ethanolamine headgroup and two different acyl chains– one saturated, 16 carbons in length (palmitic acid), and the other unsaturated, 18 carbons long (oleic acid), with a cis double bond between carbons 9 and 10. In excess water, these phospholipids will self-assemble into multilamellar vesicles (MLVs) consisting of concentric, stacked bilayers each separated by a layer of water. Such a construct will be replete with interfacial boundaries between the lipids and the aqueous environment.

Much has been learned about model membrane conformational and morphological properties through such techniques as diffraction (both neutron and x-ray), nuclear magnetic resonance, and atomic force microscopy to name a few. The properties of the membrane surface are of particular biological importance as it plays an integral role in the binding of cations, peptides, and both amphitropic and periferal membrane proteins. The membrane surface defines an interface between the membrane and its aqueous environment, the nature of which will naturally depend strongly on the chemical and electrostatic properties of the headgroups of the phospholipids, but will also be affected by the behavior of the acyl chains. That a complete micro-

scopic understanding of phospholipids mesophases in solution has yet to be developed is evidenced by the continuing efforts to explain such well studied phenomena as the ripple ($P_{\beta'}$) phase in DPPC [1–6].

The study of surfaces and interfaces with diffraction methods is a well developed technique with applications to a wide variety of materials such as colloidal suspensions [7], metal fractures [8], solid on solid systems [9], and porous materials [10]. Surface properties in such systems, which can vary from ordered and smooth to disordered and rough, can be studied effectively using small angle x-ray scattering (SAXS) and small angle neutron scattering (SANS) as these techniques have proven to be an effective measure of the properties of the surfaces averaged over all the interfaces present in the system. The intensity of the small angle scattering from such interfaces is often of the form

$$I(Q) = I_0 Q^{-\gamma} \tag{1}$$

where $Q = \frac{4\pi}{\lambda} sin\,\theta$ (2θ is the scattering angle), I_0 is a constant, and γ is a constant with physical relevance to the interface in question. The theory of such power law behavior was first developed by Porod [11] to describe the small angle scattering from smooth interfaces and has been extended to describe the scattering from rough and fractal surfaces [12,13].

II. MATERIALS AND EXPERIMENTAL METHODS

Samples of dipalmitoylphosphocholine (DPPC), DPPC in which the quaternary ammonium methyl hydrogens have been replaced with deuterium (DPPC-d_9), and 1-palmitoyl-2-oleoylphosphatidylethanolomine (POPE) were purchased from Avanti Polar Lipids, Inc. (Birmingham, AL) and used without any further purifica-

tion. For each lipid sample used in the small angle neutron scattering (SANS) experiments, 50 mg of lipid was suspended in 0.5 mL D_2O/PIPES buffer (20 mM PIPES, 1mM EDTA, 150 mM NaCl in D_2O adjusted to a pH meter reading of 7.4). This buffer simulates physiological conditions and has the advantage of avoiding potential experimental artifacts caused by marked changes in pH due to the presence of small amounts of contaminants in an unbuffered solution. The solution was centrifuged and transfered to a 1 mm pathlength Helma quartz cell and incubated at 45 °C for at least 24 hours. Excess water was drawn off and more suspension was transfered into the cell. After incubating a second time, a small amount of water was visibly separated from the remainder of the solution, confirming that the sample was in a state of excess water.

The SANS experiments were conducted at the W.C. Koehler 30 m SANS facility at Oak Ridge National Laboratory [14] using neutrons of wavelength 4.75 Å ($\delta\lambda/\lambda \sim 5\%$). Two configurations of the instrument were employed with sample to detector distances of 3.2 m ($Q = \frac{4\pi}{\lambda} sin\,\theta \in [0.017, 0.19\ \text{Å}^{-1}]$), and 18.0 m ($Q \in [0.003, 0.03\ \text{Å}^{-1}]$), for relatively low and high resolution measurements, respectively. The SANS data were corrected for instrumental backgrounds and detector efficiency and converted into absolute differential cross sections per unit sample volume using established protocols [15,16].

III. RESULTS AND DISCUSSION

A. Power Law Behavior

At twenty degrees Celsius, both DPPC and POPE form gel phases in which their acyl chains are largely trans rotomers defining a regular lattice [17–19]. The

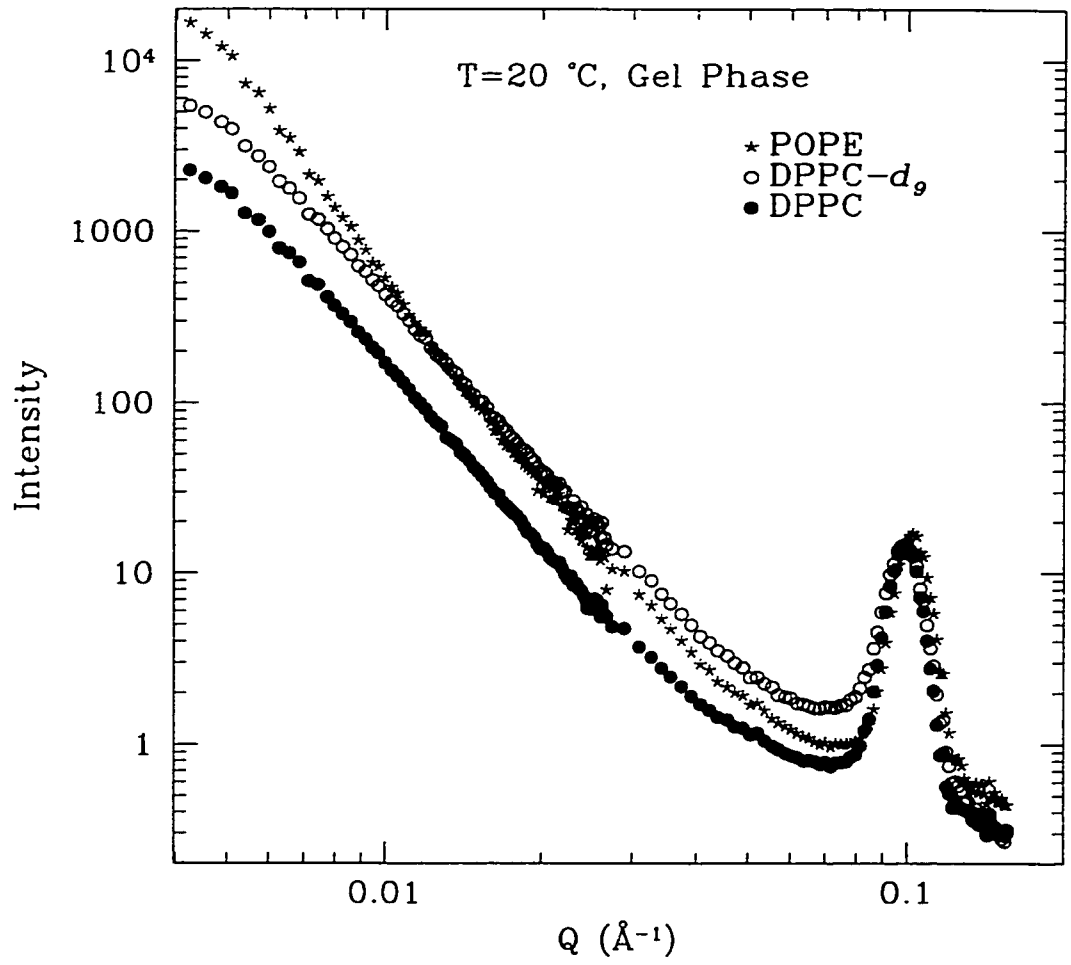

FIG. 1. Comparison of combined high and low resolution scattering profiles POPE, DPPC, and DPPC-d_9 $T = 20°C$. The scattering shows linear behavior in the small Q ($Q < 0.05\text{Å}^{-1}$) region, indicating a power law form to the scattering function, and a bilayer repeat Bragg peak at $Q \sim 0.1\text{Å}^{-1}$.

DPPC gel phase is denoted the $L_{\beta'}$ phase with the prime indicating that the acyl chains are tilted with respect to the bilayer normal. In POPE, the acyl chains are parallel to the bilayer normal so the gel phase is simply denoted L_{β}. Figure 1 shows the SANS profiles of POPE, DPPC, and DPPC-d_9 at $T = 20$ °C (gel phase). Since the SANS intensities are converted to absolute differential cross sections per unit sample volume and the Q-ranges from the two different resolution configurations overlap, we are able to assemble the data into a continuous scattering curve for each sample showing both the small angle scattering ($Q < 0.05$ Å^{-1}) and the Bragg feature due to the lamellar repeat ($Q \sim 0.1$ Å^{-1}). The linear behavior of the small Q scattering on such a log-log plot implies a scattering function of the form given by Eq. 1. The slopes of the small Q data for the DPPC and DPPC-d_9 (the PCs) are nearly identical. For the DPPC, the scattering length density contrast between the quaternary ammonium methyl groups and the solvent will be high while for DPPC-d_9 it will be very low, effectively shifting the location of the interfacial boundary between the solvent and headgroup towards the phosphate group in the deuterated sample. The slope invariance in the small angle scattering for the PCs despite the different scattering length density profiles in the vicinity of the headgroups indicates that the extracted interfacial characteristics are robust. It is clear from Fig. 1 that the small Q behavior of the POPE sample differs from the PCs as the slope in this region is much steeper.

Figure 2 shows a fit to the DPPC-d_9 data in the $L_{\beta'}$ phase. The fit consists of a power law form given by Eq. 1 and a Lorentzian centered at the lamellar repeat Bragg peak. The fit describes the data well over a decade of Q between the dashed lines at $Q = 0.005$ Å^{-1} and $Q = 0.05$ Å^{-1}. The fit for $Q > 0.05$ Å^{-1} is qualitative at best, but as we are concentrating on the small Q data we did not attempt a

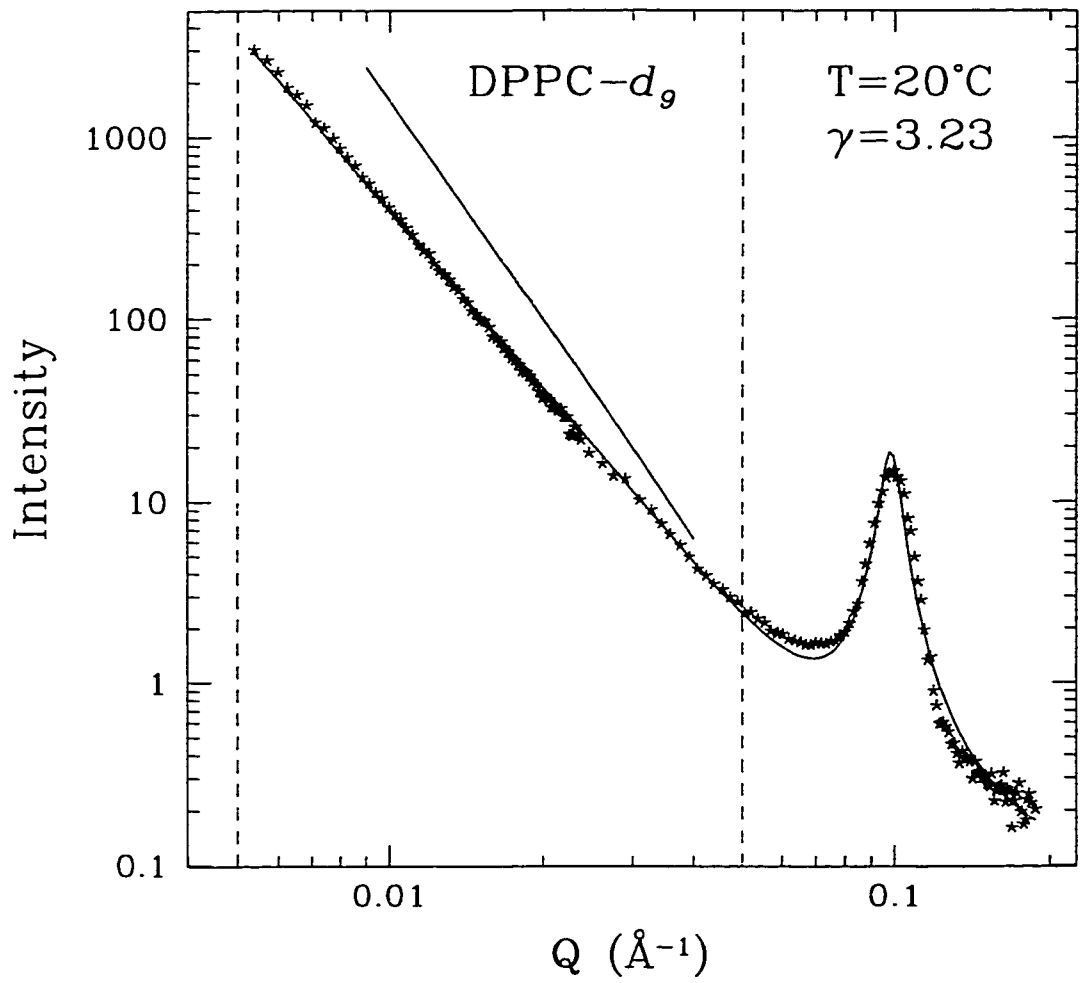

FIG. 2. Fit to the combined scattering profile of DPPC-d_9 in the $L_{\beta'}$ phase (T=20 °C). The fit consists of an inverse power law to describe the low Q data ($Q < 0.05$ Å^{-1}) and a Lorentzian centred at $Q \sim 0.1$ Å^{-1} to describe the lamellar repeat peak. The dotted lines at Q=0.005 Å^{-1} and Q=0.05 Å^{-1} delimit a decade in Q. The solid line above the low Q data shows a Q^{-4} fall off in intensity, representative of that expected from smooth, Porod, interfaces.

more complete description in this range. The exponent, $\gamma = 3.23$, of the power law describing the $Q^{-\gamma}$ form of the scattering gives a measure of the interfacial roughness. The solid line above the small Q data in the figure shows a power law with $\gamma = 4$, which would be expected for a smooth surface, falling much more quickly than the measured intensity. This difference will be discussed in more detail in section III B.

As mentioned above, the data shown in Figs. 1 and 2 are collected at two different instrumental resolutions. It was found that fitting a power law to the high resolution (low Q) data alone gave the same value of γ within uncertainty (± 0.1), so fits to the remaining samples in each phase were done to the high resolution data only. Figure 3 shows a number of these fits. The fits to the POPE data in both the L_β and L_α phases are shown in the upper panel while fits to the DPPC-d_9 data in the $L_{\beta'}$ and L_α phases are presented below. The POPE sample shows no change in γ between the two phases while the DPPC-d_9 sample exhibits a much faster fall off of intensity in the L_α phase compared to the $L_{\beta'}$ phase, with γ approaching the value seen in the POPE data. The results of power law fits for each sample as a function of temperature (phase) are summarized in Fig. 4. The PC samples consistently show a power law exponent in agreement with $\gamma = 3.4$ while in the $L_{\beta'}$ ($T = 20$ °C) and $P_{\beta'}$ ($T = 35, 37$ °C) phases. The exponent for the POPE sample remains invariant in agreement with $\gamma = 4.0$ at all temperatures and phases. All three samples display an exponent consistent with $\gamma = 4.0$ in the L_α phase.

B. Interpretation

It has long been known [11,20] that small angle scattering from a smooth surface will approach the form given in Eq. 1 with $\gamma = 4$ provided that $Q\xi \gg 1$

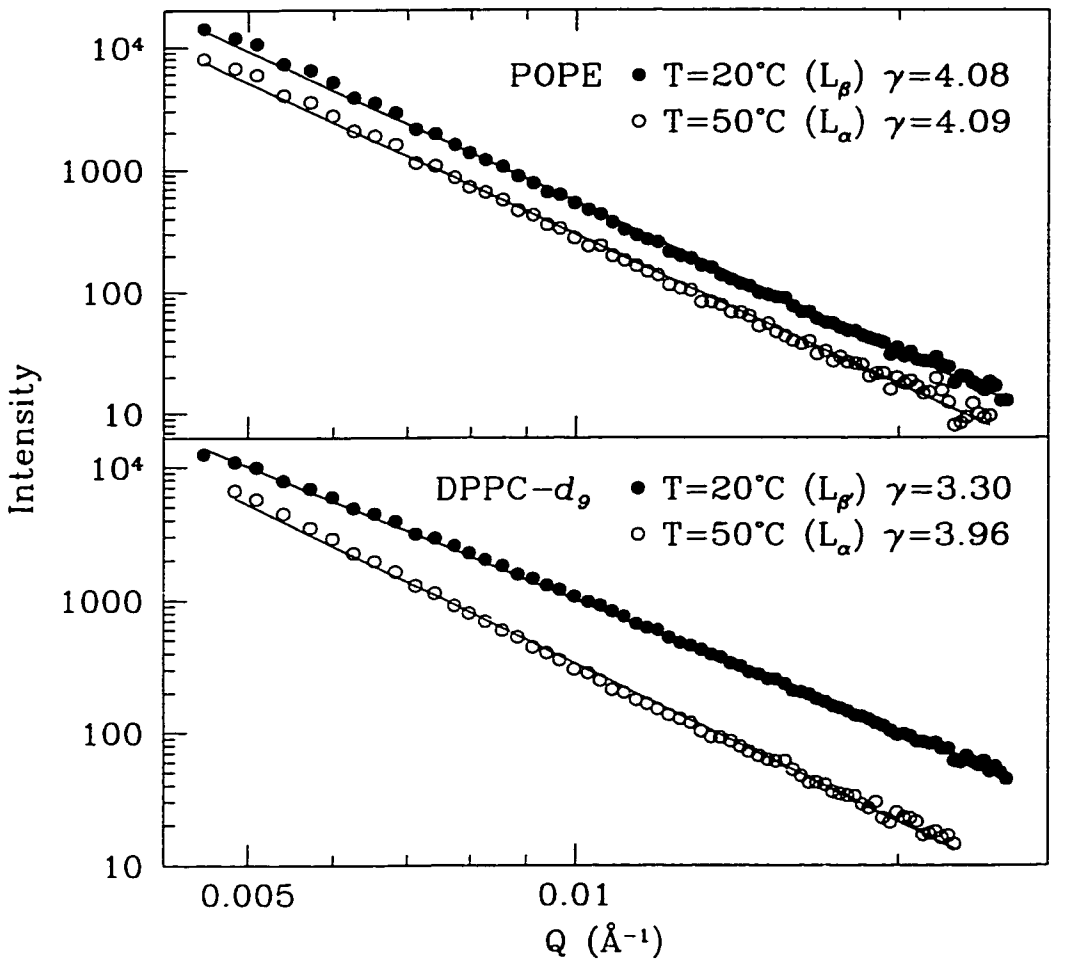

FIG. 3. Comparison of the power law fits to the small Q data in the gel (L_β,$L_{\beta'}$) and liquid crystalline (L_α) phases. The top panel presents fits to the POPE data showing no change in the slope of the data going from the L_β to the L_α phase, while the bottom panel shows fits to the DPPC-d_9 data indicating a clear change of slope between the $L_{\beta'}$ and L_α phases.

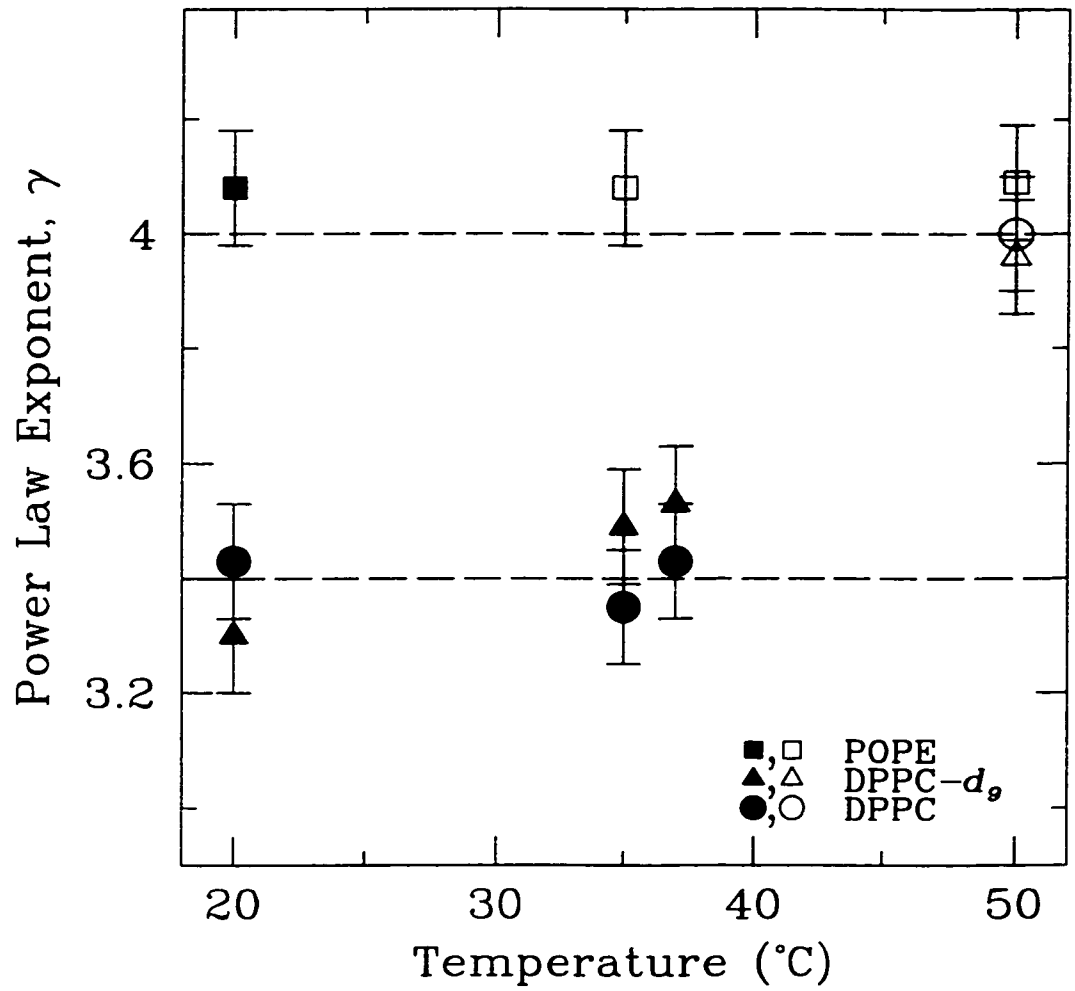

FIG. 4. Plot of the power law exponent, γ, versus temperature for samples of POPE, DPPC, and DPPC-d_9. The filled symbols represent analysis from the solid phases for each sample (L_β, $L_{\beta'}$, or $P_{\beta'}$) while the open symbols correspond to the L_α phase. The dashed line at 3.4 is consistent with all six PC solid phase exponents while the line at 4.0 agrees with all four exponents in the L_α phase and all three POPE exponents independent of phase.

where ξ is a measure of the size of the scattering systems. This is the well known Porod law. This condition is certainly satisfied as the MLVs used here will generally be no smaller than 5 μm [21]. Scattering from rough or fractal surfaces will also obey a power law of the form

$$I(q) = I_0 Q^{-(2d-d_s)} \tag{2}$$

where d is the dimension of the particle and d_s is the fractal dimension of the surface [9,10,22,23]. For a smooth interface ($d_s = d - 1$) in three dimensions, the Porod law is recovered with $\gamma = 2d - d_s = d + 1 = 4$. It is apparent from Eq. 2 that deviations from a smooth surface will serve to decrease γ from its Porod law value. A value of γ less than four does not necessarily imply that the surface being probed is a fractal in the strict sense of the word as it has been shown [13,24] that a system with randomly oriented rough surfaces will also scatter with a form given by Eq. 2.

The fact that γ for POPE does not change from the L_β phase to the L_α phase suggests that the interfacial properties of this MLV system are phase invariant. In the L_β phase the cis double bond in POPE inhibits a close packing of the acyl changes, allowing enough area for the relatively small ethanolamine headgroups to orient approximately parallel to the bilayer surface [25]. In the L_α phase the rotational isomerism of the acyl chains spreads the headgroups even further, preserving the smooth interface. At all three temperatures probed, the POPE small angle scattering is consistent, within error, with the Porod law. Interestingly, the increased hydration associated with the L_α phase [17] does not appear to affect the value of γ, although it is possible that there are competing effects which compensate.

In contrast to the POPE sample, the value for γ in the PCs varies with temperature. For the PCs in the $L_{\beta'}$ and $P_{\beta'}$ phases, $\gamma = 3.4$ implies a rough surface

with fractal dimension $d_s = 2.6$. There are a number of factors that could lead to a reduction in γ. The PC headgroup is large compared to the PE headgroup and the saturated acyl chains of DPPC have no cis bonds to impede close packing in the $L_{\beta'}$ phase. The net result is a restricted area in which to pack the PC headgroups. To relieve these constraints, the headgroups extend out from the surface to take advantage of the space available to them beyond the dimension of the interface. Such protuberances have been proposed to explain the increased steric effects seen in PC headgroup lipids compared to PEs [26]. This increases the effective dimensionality and roughness of the surface.

Another surface roughening effect that may reduce γ is the tilt of the acyl chains with respect to the bilayer normal in the $L_{\beta'}$ and $P_{\beta'}$ phases of the PCs. This tilt breaks the planar symmetry of the membrane surface by introducing a preferred orientation, ϕ, to the projection of the acyl chains onto the plane defined by the bilayer normal. Given that the chains pack on a hexagonal lattice in the solid ($L_{\beta'}$, $P_{\beta'}$) phases, for each lipid ϕ will have sixfold symmetry as it can be oriented in the direction of any of its six near neighbors. Domains of various length scales corresponding to a preferred acyl chain tilt direction, ϕ, will give rise to domain boundaries at their intersection with competing domains of tilt direction $\phi' \neq \phi$. The higher symmetry of the L_β phase in POPE generates a surface without such regions of competing orientation. The chain tilt angle is different between the $L_{\beta'}$ and $P_{\beta'}$ phases [18] so the γ invariance between these phases for the PCs suggests that it is not the magnitude of the tilt angle that matters, only the fact that it is non-zero leading to domain formation. A systematic study of the broad transition region between the $L_{\beta'}$ and $P_{\beta'}$ phases, where the number of domain boundaries would be expected to increase, could help quantify the contribution of these boundaries to the value of γ.

As is the case with POPE, the rotational isomerism of the acyl chains in the L_α phase of the PCs increases the average interchain distance. In addition the chain tilt angle goes to zero restoring planar symmetry to the interface by eliminating differences between domains. The increased area available for the headgroups allows them to recede into a two dimensional surface and the disappearance of domain boundaries ensures that this surface is smooth and discrete, analogous to POPE, with a concomitant increase in γ to a value in agreement with Porod's law. This result seems to be in conflict with computer simulations [27] and mean-field lattice theory work [28] showing a molecularly rough, diffuse interface in the DPPC L_α phase.

There are a number of interesting ideas to be extracted from this analysis. One might have anticipated that γ would fall below the Porod law value in the L_α phase as the softening of the membrane in this phase leads to increased surface undulations. That this is not the case in any of the samples, particularly the POPE which has constant γ throughout, is an indication that the scattering from the membrane interface is unaffected by fluctuations in the surface. This type Porod and fractal surface analysis is common, including the remarkable example of Beulah lignite coal [10] which exhibits power law behavior with the same fractal dimension as our solid phase PCs over more than seven decades in intensity. However, we know of no other studies where the fractal dimension of the interface is a tunable parameter as a function of temperature. In this vein, the main transition (T_m) from the L_α to the $P_{\beta'}$ phase in DPPC is shown to also correspond to an interfacial roughening transition, in addition to the standard view of it being a melting transition.

IV. CONCLUSIONS

In summary, the small angle neutron scattering profiles of DPPC, DPPC-d_9, and POPE exhibit power law behavior over a decade in Q for values of Q below the lamellar repeat Bragg peak at all temperatures probed. Fits to the data yield Porod law exponents ($\gamma = 4$) for the POPE data in both the L_β and L_α phases, and for the DPPC and DPPC-d_9 samples in the L_α phase only. The PCs exhibit consistent $\gamma = 3.4$ behavior in both of their solid phases, corresponding to scattering from a fractal surface of dimension $d_s = 2.6$. The surface roughness is due to limited packing area for the headgroups in the $L_{\beta'}$ and $P_{\beta'}$ phases which forces the headgroups to extend out of the plane defined by the bilayer normal. Acyl chain tilt in these phases which breaks the planar symmetry and leads to domain boundaries may also roughen the surface and contribute to the increase in the fractal dimension of the surface.

V. ACKNOWLEDGMENTS

This work was supported in part by the Natural Sciences and Engineering Research Council of Canada, and by the Medical Research Council of Canada under grant number MT-7654. The research at Oak Ridge supported by the Division of Materials Sciences, U.S. Department of Energy under contract No. DE-AC05-960R22464 with Lockheed Martin Energy Research Corporation.

REFERENCES

[1] W.-J. Sun, S. Tristram-Nagle, R.M. Suter, and J.F. Nagle, Proc. Natl. Acad. Sci. USA **93** 7008 (1996).

[2] H.W. Meyer, Biochim. Biophys. Acta **1302** 138 (1996).

[3] J. Katsaras, and V.A. Raghunathan, Phys. Rev. Lett. **74** 2022 (1995).

[4] T.C. Lubensky, and F.C. MacKintosh, Phys. Rev. Lett **71** 1565 (1993).

[5] J. Katsaras, R.F. Epand and R.M. Epand, Phys. Rev. E. **55** 3751 (1997).

[6] P.C. Mason, B.D. Gaulin, R.M. Epand, G.D. Wignall, and J.S. Lin, Phys. Rev. E (accepted for publication)

[7] S.H. Chen, Ann. Rev. Phys. Chem. **37** 351 (1986).

[8] B.B. Mandelbrot, D.E. Passoja, and A.J. Paullay, Nature **308** 721 (1984).

[9] P.-z. Wong, J. Howard, and J.-S. Lin, Phys. Rev. Lett. **57** 637 (1986).

[10] H.D. Bale, and P.W. Schmidt, Phys. Rev. Lett. **53** 596 (1984).

[11] G. Porod, Kolloid-Z. **124** 83 (1951).

[12] P.W. Schmidt, J. Appl. Cryst. **24**, 414 (1991).

[13] P.-z. Wong, and A.J. Bray J. Appl. Cryst. **21** 786 (1988).

[14] W.C. Koehler, Physica (Utrecht) **137B** 320 (1986).

[15] G.D. Wignall, and F.S. Bates, J. Appl. Cryst. **20** 28 (1986).

[16] W.S. Dubner, J.M. Schultz and G.D. Wignall, J. Appl. Cryst. **23**, 469 (1990).

[17] J. Katsaras, K.R. Jeffrey, D.S.-C Yang, and R.M. Epand, Biochemistry **32** 10700 (1993).

[18] A. Tardieu, V. Luzzati, and F.C. Reman, J. Mol. Biol. **75** 711 (1973).

[19] D.C. Wack, and W.W. Webb, Phys. Rev. A. **40** 2712 (1989).

[20] P. Debye, H.R. Anderson, and H. Brumberger J. Appl. Phys. **28** 679 (1957)

[21] M.K. Jain, and R.C. Wagner *Introduction to Biological Membranes* (Wiley, New York, 1980).

[22] J.K. Kjems, and P. Schofield. In *Scaling Phenomena in Disordered Media* edited by R. Pynn and A. Skjeltorp, pp 141-149 (Plenum, New York, 1985).

[23] J.E. Martin, and A.J. Hurd, J. Appl. Cryst. **20**, 61 (1987).

[24] P.-z. Wong, Phys. Rev. B. **32** 7417 (1985).

[25] G. Cevc, and D. Marsh, *Phospholipid bilayers* (Wiley, Toronto, 1987).

[26] T.J. McIntosh, Chem. Phys. Lipids **81** 117 (1996).

[27] E. Egberts, and Berendsen, H.J.C., J. Chem. Phys. **89** 3718 (1988).

[28] F.A.M. Leermakers, and Scheutjens J.M.H.M., J. Chem. Phys. **89** 3264, 6912 (1988)

Chapter 6

Summary

Model membrane systems have been of considerable interest to scientists both as an analogue of biological membranes and for their material and thermodynamic properties. Scattering techniques play a key role in the determination of the structure and phase behaviour of these systems. In this thesis we have demonstrated the applicability of small angle neutron and X-ray scattering to extracting information on phospholipid systems in excess water. Three main results are presented and summarized here, along with some comments on outstanding issues and future work.

A combination of small angle neutron and X-ray scattering on multilamellar samples of DPPC have shown that the DPPC ripple phase obtained after cooling from the high temperature L_α phase is metastable and long-lived. The diffraction pattern of the metastable $P_{\beta'}$ phase is markedly different than the equilibrium $P_{\beta'}$ phase it has been shown that, due to the different sensitivities of the two probes, the use of both neutrons and X-rays in tandem is necessary to extract all the salient features of the metastable $P_{\beta'}$ diffraction pattern for DPPC. In doing so, a simple, single wavelength model of the bilayer surface modulation in the metastable $P_{\beta'}$ phase emerges which fully describes the diffraction patterns seen using both X-rays and neutrons. This new

model also consistently describes previously published X-ray work on the metastable phase. Should the issue of fully hydrated aligned samples be satisfactorily settled, experiments on the metastable $P_{\beta'}$ phase could be done which could conclusively determine the viability of our model.

Some surprises in the ripple phase DPPC MLV work are that the metastable ripple wavelength has an anomalously strong temperature dependence and that the metastable nature is carried into the the lower temperature gel $L_{\beta'}$ phase. Unlike the ripple phase, however, the metastable gel phase is not long lived.

The SANS work on large unilamellar vesicles of DPPC proved equally fascinating. An accurate value of the vesicle parameters were extracted through some relatively simple analysis. Most importantly, diffraction evidence for the formation of the $P_{\beta'}$ phase in DPPC LUVs is presented for the first time, a result which is supported by the accompanying calorimetric data. This result should aid in the development of a theoretical treatment of the ripple phase as it suggests that bilayer-bilayer interactions are not necessary to drive the system into this phase.

Finally, high resolution, small angle neutron scattering profiles of three different multilamellar lipid samples have been studied to determine their bulk interfacial properties. Results indicate that POPE, with its relatively small headgroup and inhibited acyl chain packing, exhibits a smooth interface in both the gel (L_β) and liquid crystalline L_α phases. On the other hand, DPPC and DPPC-d_9 are consistent in showing that the gel-like phases ($L_{\beta'}$ and $P_{\beta'}$) have a rough lipid-solvent interface, while the L_α phase interface is well-defined, with results indicating a surface dimensionality of d_s=2 consistent with the POPE interface in both phases and with Porod's law.

From the currently available data it is not possible to conclusively pinpoint the source of the interfacial roughening in the PCs. It may be due to the limited area

available for the PC headgroups in the gel-like phases, causing the ammonium methyl groups to protrude from the bilayer surface. Another possibility is the proclivity to form competing domains which will result in interfacial roughening domain boundaries. It is interesting to note that the interfacial roughness does not change from the $L_{\beta'}$ phase to the $P_{\beta'}$ phase despite the change in acyl chain tilt angle between the phases and the increased rotational motion of the headgroup in $P_{\beta'}$ phase. It might be informative to perform the same type of scattering experiments and analysis of DPPC MLVs as they pass through the pretransition to see if the interfacial roughness remains constant throughout. As well, experiments could be done with PC headgroup lipids that form a L_{β} phase instead of an $L_{\beta'}$ phase to see what influence the tilt angle has on the interface defined by the headgroup-solvent boundary.

Bibliography

Avnir, D., Farin, D. & Pfeifer, P. (1984), *Nature (London)* **308**, 261.

Bale, H. D. & Schmidt, P. W. (1984), *Phys. Rev. Lett.* **53**, 596.

Cameron, D. G. & Mantsch, H. H. (1982), *Biophys. J.* **38**, 175.

Casal, H. L. & Mantsch, H. H. (1984), *Biochim. Biophys. Acta.* **779**, 381.

Cevc, G. & Marsh, D. (1987), *Phospholipid Bilayers*, John Wiley & Sons, Toronto.

Cevc, G., Zeks, B. & Podgornik, R. (1981), *Chem. Phys. Lett.* **84**, 209.

Czajkowsky, D. M., Huang, C. & Shao, Z. (1995), *Biochemistry* **34**, 12501.

Debye, P. (1915), *Ann. Physik* **46**, 809.

Debye, P., Anderson, H. R. & Brumberger, H. (1957), *J. Appl. Phys.* **28**, 679.

Doniach, S. (1979), *J. Chem. Phys.* **70**, 4587.

Epand, R. M. (1996), *Chem. Phys. Lipids* **81**, 101.

Falkovitz, M. S., Seul, M., Frisch, H. L. & McConnell, H. M. (1982), *Proc. Natl. Acad. Sci. USA* **29**, 3918.

Franks, N. P. & Lieb, W. R. (1981), X-ray and Neutron Diffraction of Lipids, *in* C. G. Knight, ed., 'Liposomes: from Physical Structure to Therapeutic Applications', Elsevier/North-Holland Biomedical Press, Amsterdam, p. 242.

Friedrich, W., Knipping, P. & Laue, M. (1912), *Proceedings of the Royal Bavarian Academy of Science* p. 303.

Gamble, R. C. & Schimmel, P. R. (1978), *Proc. Natl. Acad. Sci. USA* **75**, 3011.

Grünewald, B., Frisch, W. & Holzwarth, J. F. (1981), *Biochim. Biophys. Acta.* **641**, 311.

Guinier, A. & Fournet, G. (1955), *Small Angle Scattering of X-rays*, Wiley, New York.

Harrison, R. & Lunt, G. (1975), *Biological Membranes: Their Structure and Function*, John Wiley & Sons, Toronto.

Hatta, I., Kato, S. & Takahashi, H. (1993), *Phase Transitions* **45**, 157.

Hope, M. J., Bally, M. B., Webb, G. & Cullis, P. R. (1985), *Biophys. Acta.* **812**, 55.

Israelachvili, J. & Wennerström, H. (1992), *J. Phys. Chem.* **96**, 520.

Israelachvili, S., Marčelja, S. & Horn, R. (1980), *Quart. Rev. Biophys.* **13**, 121.

Katsaras, J. (1997), *Biophys. J.* **73**, 2924.

Kjems, J. K. & Freltoft, T. (1985), *in* R. Pynn & A. Skjeltrop, eds, 'Scaling Phenomena in Disordered Systems', Plenum, New York, p. 141.

Koehler, W. C. (1986), *Physica (Utrecht)* **137B**, 320.

Larsson, K. (1977), *Chem. Phys. Lipids* **20**, 225.

Lemmich, J., Mortensen, K., Ipsen, J. H., Honger, T., Bauer, R. & Mouritsen, O. G. (1996), *Phys. Rev. E* **53**, 5169.

Lumsden, M. A. (1998), X-ray diffraction study of dppc aligned on mica, Master's thesis, McMaster Unversity.

Mandelbrot, B. B. (1983), *The Fractal Geometry of Nature*, Freeman, New York.

Martin, J. E. & Hurd, A. J. (1987), *J. Appl. Cryst.* **20**, 61.

Mitsui, T. (1978), X-ray diffraction studies of membranes, *in* M. Kotani, ed., 'Advances in Biophysics', Vol. 10, Japan Scientific Societies Press, Toronto.

Mou, J., Yang, J. & Shao, Z. (1994), *Biochemistry* **33**, 4439.

Mouritsen, O. G. (1991), *Chem. Phys. Lipids* **57**, 179.

Nagle, J. F. (1980), *Annu. Rev. Phys. Chem.* **31**, 157.

Nagle, J. F., Petrache, H. I., Gouliaev, N., Tristram-Nagle, S., Liu, Y., Suter, R. M. & Gawrisch, K. (1998), *Phys. Rev. E, accepted for publication* .

Pearce, P. A. & Scott, H. L. (1982), *J. Chem. Phys.* **77**, 951.

Pearson, R. H. & Pascher, I. (1979), *Nature* **281**, 499.

Placzek, G. (1952), *Phys. Rev.* **86**, 377.

Porod, G. (1951), *Kolloid-Z.* **124**, 83.

Porod, G. (1982), General theory, *in* O. Glatter & O. Kratky, eds, 'Small Angle X-ray Scattering', Academic Press, Toronto.

Ruland, W. (1971), *J. Appl. Cryst.* **4**, 70.

Schmidt, P. W. (1991), *J. Appl. Cryst.* **24**, 414.

Shepherd, J. C. W. & Büldt, G. (1978), *Biochim. Biophys. Acta.* **514**, 83.

Shepherd, J. C. W. & Büldt, G. (1979), *Biochim. Biophys. Acta.* **558**, 41.

Singer, S. J. & Nicolson, G. L. (1972), *Science* **175**, 720.

Singh, M. A. & Barberato, C. (1997), *Physics in Canada* **53**(5), 261.

Sobry, R., Ledent, J. & Fontaine, F. (1991), *J. Appl. Cryst.* **24**, 516.

Squires, G. L. (1978), *Introduction to the Theory of Thermal Neutron Scattering*, Cambridge University Press, New York.

Suwalsky, M. & Tapia, J. (1981), *Z. Naturforsch. Teil C Biochem. Biophys. Biol. Virol.* **36**, 875.

Tanford, C. (1980), *The Hydrophobic Effect*, John Wiley & Sons, New York.

Tardieu, A., Luzzati, V. & Reman, F. C. (1973), *J. Mol. Biol.* **75**, 711.

Trahms, L. W., Klabe, D. & Boroske, E. (1983), *Biophys. J.* **42**, 285.

Wack, D. C. & Webb, W. W. (1989), *Phys. Rev. A.* **40**, 2712.

Warren, B. E. (1990), *X-Ray Diffraction*, Dover Publications, Inc., New York.

Windsor, C. G. (1988), *J. Appl. Cryst.* **21**, 582.

Wong, P. z. & Bray, A. J. (1988), *J. Appl. Cryst.* **21**, 786.

Yao, H., Matuoka, S., Tenchov, B. & Hatta, I. (1991), *Biophys. J.* **59**, 252.

Yeagle, P. (1987), *The Membranes of Cells*, Academic Press, Toronto.

Zhang, S., Tristram-Nagle, S., Headrick, R. L., Suter, R. M. & Nagle, J. F. (1995), *Phys. Rev. Lett.* **74**, 2832.